COHERENT RAMAN STANDOFF DETECTION

By

Marshall T. Bremer

A DISSERTATION

Submitted to
Michigan State University
in partial fulfillment of the requirements
for the degree of

Physics - Doctor of Philosophy

2013

ABSTRACT

COHERENT RAMAN STANDOFF DETECTION

By

Marshall T. Bremer

This dissertation outlines the development of several laser-based methods of detecting chemicals at a distance. They are based on two forms of coherent Raman scattering: coherent anti-Stokes Raman scattering and stimulated Raman scattering. The specific motivation is to detect trace quantities of explosives, but the techniques can be adapted to other applications where chemical analysis of macroscopic samples is of interest. Each method is developed toward an imaging modality as the ultimate demonstration of sensitivity and specificity.

Spontaneous Raman scattering is a linear process sensitive to molecular vibrations and well known for its chemical specificity. Unfortunately, this weak signal is only suitable for standoff detection of chemicals in bulk form. Coherent Raman processes are non-linear phenomenon in which the phase of the scattered light can be predicted or controlled. This can lead to dramatic enhancements in the signal strength through coherent addition of the fields from different scatterers and allows amplification through externally applied fields. These phenomena are utilized in the development of the most powerful Raman-based standoff detection systems to date, capable of detecting nanogram quantities of explosives with a few laser shots at 10 meters. The technique is non-destructive, using laser wavelengths in the near IR with an average power of less than 10 mW.

The enabling tools are an ultra-short (<10 fs) pulsed laser and a pulse shaper. This laser pulse is capable of impulsive excitation of virtually all Raman active vibrations. The pulse shaper enables resolution of the different modes or selective excitation of individual vibrations through non-linear interference within the broadband pulse. The result is a simple experimental setup capable of detecting trace quantities of hazardous materials.

DEDICATION

The dissertation is dedicated to my wife, Abigail, and son, Maxwell,
by far the most important discoveries of my graduate career.

ACKNOWLEDGEMENTS

Looking back on the standoff detection project, I am very proud of our work and I appreciate the opportunity to pursue this important goal. Many people contributed to its success and my understanding of non-linear optics.

First, I thank previous and current members of the Dantus group for their contributions in building and improving the lab and experimental setup. I am especially grateful to Dr. Paul Wrzesinski, Dr. Vadim Lozovoy, and Dr. Dmitry Pestov for insightful discussions on coherent Raman processes. I am indebted to all current members of the Dantus group for creating a stimulating and fun environment in which to explore non-linear optics.

I thank my advisor, Marcos Dantus, for providing a great research project and the funds to complete it. I appreciate the freedom I was afforded in pursuing the goals, and encouragement to try "out of the box" approaches. I am grateful for the opportunity to do research in a world class laboratory and the expert advice on how to best put femtosecond lasers to use.

I thank the members of my committee, Professors Chong-Yu Ruan, John McGuire, Carlo Piermarocchi, and Scott Pratt, for support and guidance in completing my dissertation. I have enjoyed my time at Michigan State University, and I am also grateful for all the support I have received from the faculty and my peers in the Department of Physics and Astronomy.

Initial funding for the CARS standoff detection project was from a grant awarded to BioPhotonic Solutions Inc. and to Michigan State University by the United States Army Research Office (USARO). The author's contributions were funded by a subsequent grant from the Department of Homeland Security, Science and Technology Directorate, under Contract No. HSHQDC-09-C-00135 (Dr. Michael Shepard, Program manager), administered by The John Hopkins University, Applied Physics Laboratory (Dr. Robert Osiander and Dr. Jane M. Spicer Program Managers). Additional funds supported the author and the general development of non-linear spectroscopies and imaging techniques. These were provided by the Air Force Research Laboratory under Contract No. FA8650-10-C-2008 and by the Air Force Office of Scientific Research (Dr. Enrique Parra, Program Manager). The Dissertation Completion Fellowship from the Graduate School also provided support in the summer of 2009.

PREFACE

Significant research effort has focused on using lasers to quickly detect dangerous compounds, such as explosives, from a safe distance. Recently, these efforts have been directed toward detecting trace residues deposited on surfaces since the bulk material may be concealed. This is a significant challenge as most laser based methods capable of detecting trace quantities, such as those based on fluorescence or laser induced breakdown spectroscopy, encounter major difficulties making positive chemical determination of surface-adsorbed molecules in the presence of other hydrocarbons. In contrast, Raman spectroscopy is exceptional at discriminating between compounds. Unfortunately, the small scattering cross-section makes trace detection prohibitively time consuming.

The approach used in this dissertation is to use the latest ideas in the field of non-linear optics to dramatically increase the speed with which Raman-specific information can be obtained from a surface. In the past decade, coherent Raman techniques have been used to great effect in microscopy, providing video rate chemical imaging of cells. The setup is somewhat cumbersome, generally involving the synchronization and overlap of several lasers, and much of the research focuses on simplifying the setup and eliminating interfering non-linear signals. We have created a number of concise versions of this spectroscopy, employing a single femtosecond laser and a pulse shaper, and applied it to standoff detection. Standoff detection presents unique challenges due to the low numerical aperture and the focus on detection rather than contrast. These challenges are addressed. The result is more than a proof of principle or an interesting

experimental realization of ideas in non-linear optics. The result is arguably the best solution to the problem of standoff detection of trace quantities of hazardous materials.

Chapter 1 provides the motivation for coherent Raman standoff detection. Despite the wealth of analytical chemistry techniques developed in human history, no clear solution has been found. A few currently pursued linear techniques are described to illustrate the difficulties. Ultrafast lasers become an attractive and realistic approach despite the complexity and expense. The fundamentals of the most popular non-linear Raman spectroscopic technique, coherent anti-Stokes Raman scattering (CARS), are presented in Chapter 2. The process was discovered 50 years ago but remains a very active area of research. This is due to both the rapid improvement of pulsed laser technology and subtle complexities in the measurement, such as the non-resonant background, that prevent the associated measurement techniques from reaching their full potential. The single-beam and multi-beam approaches are described to highlight the advantages of the former despite the uncommon nature of the measurement. A classical model of the process is developed here to illustrate the most important properties. This model is easily extended to the SRS measurement of Chapter 5.

CARS-based standoff detection has been pursued for a number of years. The author's first contribution to the field is in quantifying the potential sensitivity of the measurement within a complex chemical environment meant to mimic surfaces found in the real world. This is described in Chapter 3. This chapter also describes the experimental setup used throughout most of the dissertation. While the measurement principle had been demonstrated previously,

experimental advances were made to provide the most compelling evidence of the viability of single-beam CARS standoff detection.

The broad bandwidth of femtosecond lasers combined with spectral phase shaping enable interesting opportunities in coherent control of molecular vibrations. This is fundamentally interesting, but can also provide practical benefits toward increasing the sensitivity of CARS. The background and potential of this selective excitation are addressed in Chapter 4. One experimental implementation is presented in detail.

Chapter 5 describes the development of the first stimulated Raman scattering (SRS) based standoff detection system. Generally, SRS was considered inapplicable to sensitive standoff detection. We have recently devised a robust, sensitive method to detect explosives deposited on realistic surfaces. The technique uses the selective excitation ideas of Chapter 4 to detect chemicals through the transfer of photons within the laser bandwidth. This is the author's most important and distinct contribution to the field and is presently the most powerful Raman-based standoff detection method. A brief discussion of the prospects of this research is presented in the final chapter.

The appendices contain useful information for the interested reader. Appendix A can be treated as a brief aside into another application of single-beam CARS: combustion diagnostics. The measurement uses a very similar experimental setup as the standoff work and provides some additional insight into the CARS process. CARS thermometry is described and chemical and thermal images of a flame are presented. Appendices B and C provide some mathematical

descriptions of femtosecond pulses and pulse shaping, intended as a primer for graduate students new to the field and to provide some definitions used throughout the dissertation. Appendix D contains experimental details which are not crucial to understanding the concepts, but will help in reproducing the results.

TABLE OF CONTENTS

LIST OF FIGURES

KEY TO ABBREVIATIONS

CARS	Coherent Anti-Stokes Raman Scattering
DNT	Dinitrotoluene
GDD	Group Delay Dispersion
IR	Infrared
SLM	Spatial Light Modulator
SRS	Stimulated Raman Scattering
TL	Transform Limited
TNT	Trinitrotoluene

1. Motivation for Coherent Raman Standoff Detection

Standoff detection can refer to a broad range of situations, but the essential feature is that a chemical or object is detected some distance from the measuring device. The canonical example is the detection of a bomb from a safe distance. Metal detection or observation of visual cues can be useful for detecting such hazards, but our focus is standoff detection of *chemicals*.

Atmospheric monitoring on earth, or even extra-solar planets, uses stars as light sources and could be considered standoff detection of chemicals. This class of detection is more appropriately termed remote sensing. The types of problems recently explored with standoff detection are directed toward human safety and include: monitoring of industrial emissions, detecting poison gas attacks (battlefield or elsewhere), detecting illegal drugs, monitoring mail for bioterrorism, informing first responders to disasters, detecting roadside bombs, and monitoring public spaces for weapons of mass destruction. These goals vary in target distance and quantity to be detected. The work explored in this dissertation can be applied to many of the above situations, but the specific target is detection of trace quantities of chemicals at modest standoff (2-50 m), with an emphasis on explosives detection.

1.1 The Problem

Many technologies have been developed to address this challenge, but the most successful approaches are based on air sampling, mimicking the oldest standoff detector: the nose. Bomb-

sniffing dogs are arguably the best technology available. However, people desire a more robust, scalable, and user friendly system. Mass spectrometry can detect a single molecule, with virtually perfect specificity (for small molecules). These are used to analyze hand swabs at the airport and monitor the air in sensitive locations. Absorption spectroscopy is also very sensitive and chemically specific in the gas phase.[1] Researchers are developing additional air sampling techniques based on SERS or functionalized materials.[2,3]

Unfortunately, most explosives have extremely low vapor pressures.[4] Room temperature equilibrium concentration of vapor phase trinitrotoluene (TNT) is 10 ppbv. Ammonium nitrate, a component of the bomb used in the Oklahoma City bombing, has a similar vapor pressure. PETN, used in the shoe and Christmas Day bombing attempts, is present at one part per billion levels. Other common high-explosives, such as HMX and RDX, have part per trillion concentrations or lower. Plastic bonding of high explosives generally reduces this vapor pressure. These figures represent the saturated vapor levels and real world situations will present significantly lower quantities of vapor-phase molecules, severely limiting the effectiveness of air sampling methods.

This suggests the need for an optical technique capable of detecting explosives in the more abundant condensed phase. Often the explosive is deliberately concealed, and the technique should be directed toward detecting trace amounts of these compounds on surfaces, as indicators of concealed danger. There are several reviews on the subject of standoff detection of explosives which outline the many approaches used so far.[4–7] The research is highly competitive with no

technique clearly identified as the most advantageous. The next section outlines some of the most obvious approaches and some of the most competitive.

1.2 Optical Techniques

1.2.1 Fluorescence Spectroscopy

Fluorescence spectroscopy can be a powerful technique to detect atoms of molecules in the gas phase. By shining the appropriate laser wavelength on the target, the atom or molecule of interest may transition to the excited electronic state. The excited species may then radiatively decay to the ground state or a lower excited state and the emitted photons can be collected at a distance. These two processes are wavelength specific and provide two pieces of spectroscopic information. Furthermore, the cross section for this process is quite strong, producing ample signal.

Unfortunately, these narrow, highly-specific transitions become very broad in the condensed phase at room temperature. This makes fluorescence a valuable technique for gas phase detection, but not for standoff detection of explosives.

1.2.2 IR absorption Spectroscopy

Infrared (IR) absorption spectroscopy is based on optically active vibrational transitions in molecules. The vibrational spectrum of a molecule is unique (excluding enantiomers) providing a valuable method of chemical identification. As with fluorescence measurements, a light source

of appropriate wavelength is shined on the sample to induce vibrational excitation. The excited molecules may re-emit at a characteristic frequency, but this is generally not collected due to the high background radiation and expensive detectors for this wavelength range. Instead, the absorption is measured by comparing the incident light to the transmitted light. This is a powerful technique for gas-phase detection, achieving ppb levels with explosives using cavity ring down spectroscopy.[1]

The transitions broaden significantly in the condensed phase, similar to electronic excitations. With the proper experimental setup, however, the method is a powerful tool for chemical analysis, common in analytical chemistry labs. In these instruments, a sample is placed in a carefully calibrated optical setup and the transmission changes are recorded. Similarly, UV/Vis absorption spectrometers are available for electronic transitions. This is virtually inapplicable to standoff detection, where the environment cannot be well calibrated. Still, there have been several attempts to develop this instrument for standoff detection.[8–10]

A few groups have pursued improved techniques based on IR absorption. Instead of measuring the change in laser spectrum after reflecting from the sample, they try to identify temperature changes in the sample. This can manifest as an acoustic pulse (if pulsed lasers are used) as the matter expands slightly, or as thermal radiation which can be detected with a thermal camera.[8,11] These are among the most competitive methods for standoff detection of explosives.

1.2.3 Raman Spectroscopy

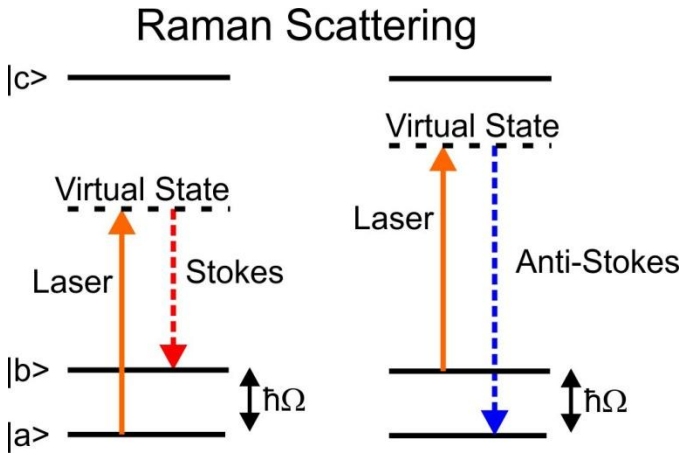

Figure 1.1. Energy level diagram of Raman scattering. The laser excites a virtual state, which immediately transitions to a new vibrational state and emits a photon. For interpretation of the references to color in this and all other figures, the reader is referred to the electronic version of this dissertation.

Raman scattering is an inelastic photon scattering process where the frequency of the scattered field differs from that of the incident. This difference corresponds to a vibrational transition within the scattering molecule and conservation of energy is maintained by this transition. The process is diagramed in Figure 1.1. At room temperature, the excited vibrational states have a low probability of being populated, and the red-shifted Stokes scattering is much stronger than anti-Stokes scattering. Unlike IR absorption spectroscopy, light is emitted from the sample at new frequencies and the signature is unambiguous. Lasers of any wavelength can be used. Furthermore, the Raman spectrum generally consists of well separated narrow features even in the condensed phase (see example in Figure 1.2), improving the ability to detect trace quantities of compounds in chemical mixtures.

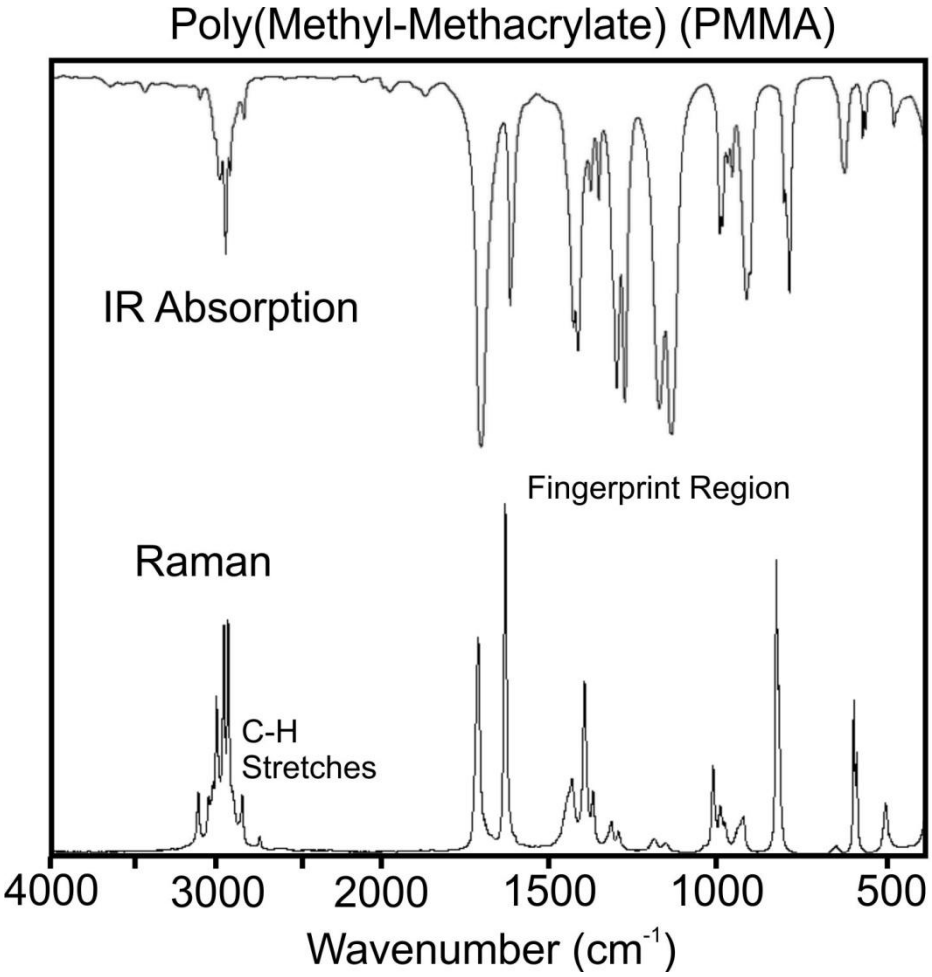

Figure 1.2 The Raman and IR absorption spectrum of PMMA. They contain similar information, but the Raman resonances are generally much narrower. The non-linear scale highlights the spectroscopically rich fingerprint region. Source: AIST Japan, Spectral Database for Organic Compounds.

Several groups have developed standoff detection systems based on Raman scattering[10,12–15] and have achieved detection of bulk quantities of explosives at 50-500 m.[14,16] The most successful approaches use high-energy/ low-rep-rate lasers and time-gated spectrometers to reduce fluorescence interference and noise from ambient light. Unfortunately, the spontaneous Raman cross section is quite small and large quantities of material are required to scatter enough photons to detect. As an example, the Raman scattering cross section of the strongest

resonance of TNT is ~10^{-29} cm^2/sr/molecule for 515 nm light.[17] Therefore, the probability that a photon will be scattered by a 1mm thick film of TNT, approximately 100 mg/cm^2, is ~10^{-7}. Assuming uniform angular distribution of the scattering, a two inch optic will collect a fraction of only ~10^{-6} scattered photons at 10 meters. A one mJ pulse (very energetic) in the visible contains roughly 10^{16} photons, leaving only 1000 photons available for detection. Trace detection (<100µg/cm^2) using visible or infrared wavelengths is virtually impossible.

1.2.3.1 UV Raman

A recently explored avenue to increase the Raman cross section is to use UV lasers. Several groups have successfully increased the cross section through resonant enhancement using UV laser sources.[12,16,18–21] Up to one-hundred fold increase in the cross section is measured.[22] At first, the use of UV lasers would seem to exacerbate the fluorescence interference, but by using deep UV light (e.g. 247nm) the Raman scattered light is shifted to the UV, below the wavelength range of fluorescence of most compounds. Detection of trace quantities (1µg/cm^2) of neat explosives has been demonstrated using a UV laser at 30cm standoff, but the extrapolated performance estimate was 300 signal photons collected in 20 seconds using 25mW of laser power (degradation limit).[21] Demonstrations on fabric or other real world surfaces have yet to achieve trace level (<100µg/cm^2) detection.[20]

1.3 Coherent Raman

Instead of increasing the Raman cross section, the Raman signal can be enhanced through coherent methods. If the phase of the scattered field from each molecule can be controlled, it opens up several avenues with which one can collect more scattered photons.

If there is a direct phase relationship between an incident laser field and the scattered field, the scattered light gains some interesting properties. The fields will add *coherently*.

1. The field will propagate directionally, as laser light does. The propagation mode will be related to that of the incident field, sample volume, and material dispersion.

2. Since the fields will add, the intensity of the scattered light is proportional to the square of the number of scatterers, thus it will grow quadratically with interaction length (assuming perfect phase matching).

3. It is possible to amplify this light with another light field. This is called heterodyne amplification, the same phenomenon used to amplify radio frequency signals in your car.

The first property will make it easy to collect the signal with a small optic. This is not generally useful for standoff detection unless we can adjust the phase matching conditions so that the

signal field travels backwards. However, this advantage is useful for the measurements on flames explored in Appendix A.

The second property can give coherent Raman a profound advantage over spontaneous Raman for standoff detection. Let us consider a collection of one million Raman scatterers from the field perspective. If they emit in phase, the fields will add and the intensity will grow with the square of the number of scatterers. There will be one million times more photons to detect than if they emit with random phase. Considering that a one micron cubed grain of sugar contains more than a billion molecules, coherent methods can provide huge improvements in the speed and sensitivity of Raman based standoff detection.

The 3rd property can lead to arbitrary amplification of the signal. This property is not explored until the final chapter, but the idea is very simple. Consider two fields of the same frequency, E_s and E_{lo}. E_s is the weak signal to be amplified by the constant and strong local oscillator field, E_{lo} (local oscillator is a term carried over from RADAR applications). The intensity, measured by a photodetector, is proportional to the square of the total field.

.

$$I \propto |E_{total}|^2 = |E_s + E_{lo}|^2 = |E_s|^2 + |E_{lo}|^2 + 2Re(E_s E_{lo}^*).$$

The second term is constant. The third term shows the signal amplification by the local oscillator. Depending on the relative phase, this term can range from positive to negative. For

small signals, the first term is comparatively very small and can be ignored. Note that this is the complex field representation as described in Appendix A.1.

In the next chapter, the most common form of coherent Raman, coherent anti-Stokes Raman scattering is described.

2. Coherent Anti-Stokes Raman Scattering

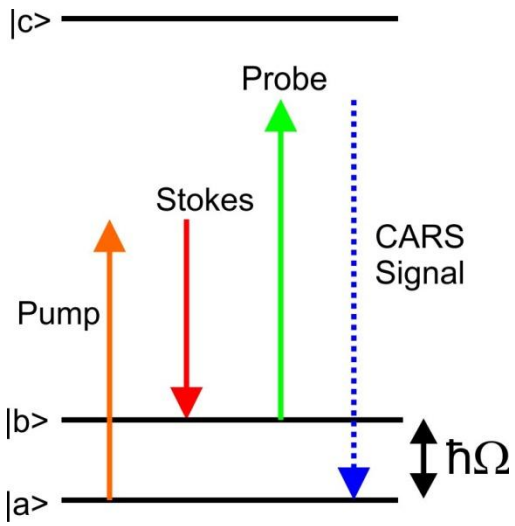

Figure 2.1. Energy level diagram of the CARS process. There are three interactions between the material and the field producing the CARS signal. The pump and Stokes fields couple the ground and excited vibrational states. The probe interaction, which can occur at a later time, produces the CARS signal at a new frequency.

Coherent anti-Stokes Raman scattering (CARS) is a four-wave mixing process sensitive to Raman transitions. This is one of many four-wave mixing phenomena. All are commonly described in terms of the third order non-linear susceptibility. The energy diagram for this process is shown in figure 2.1. The first two fields (pump and Stokes) couple the ground state to the excited vibrational state and create a coherent superposition of states. This is mediated by a virtual state, and the process can be performed with off-resonance fields. A third field, called the probe, scatters from this coherence and returns the molecular ensemble to the ground state, creating a fourth blue-shifted field.

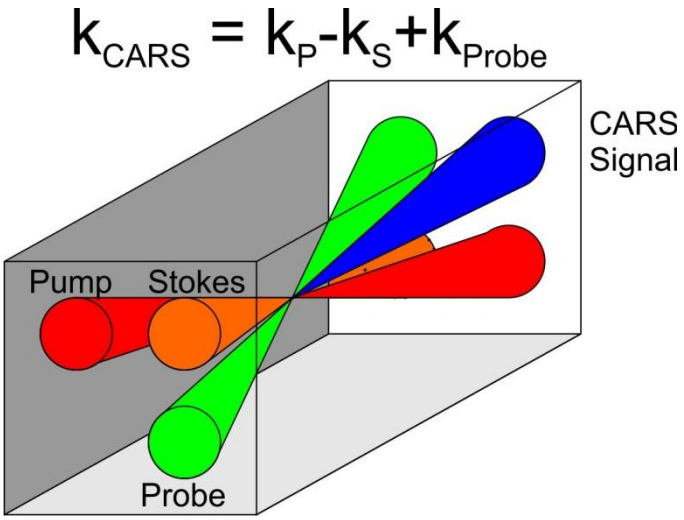

Figure 2.2. Schematic of CARS in the BOXCARS geometry. The direction of the signal is determined by conservation of momentum. Properly chosen angles can improve phase matching in dispersive material.

The new field, or CARS signal, is shifted by the frequency of the vibrational transition from the probe frequency. The CARS signal forms a coherent beam and there is a specific phase relation to the probe field. In contrast to Raman, the signal scales quadratically in molecule number, cubic in total laser intensity, and there is no fluorescence (single photon) interference since the signal is blue shifted from the incident fields. An interesting geometry for this experiment is shown in Figure 2.2. Conservation of momentum determines the direction of the resultant CARS signal, and in the geometry shown, there is no background from the incident lasers.

CARS was discovered in 1963 by Terhune[23] who was working at the Ford Motor Company Laboratory. One of the original uses for this non-linear spectroscopy was the study of combustion where the directional signal and 3D sectioning ability of the method provided an advantage over spontaneous Raman. It has also been used for spectroscopy.[24] In the last decade, most of the CARS research has been toward microscopy applications.[25]

Spontaneous Raman scattering has been used for several decades in microscopy. The specificity allows identification of chemicals within biological tissue. This can be very sensitive, identifying a collection of fewer than 1000 molecules within a cell. This level of sensitivity is very time consuming (~1 second for the example) because of the low efficiency of Raman scattering. Creating a chemical image requires raster scanning of the Raman laser, meaning a one megapixel image will take 12 days in the above scenario. CARS microscopy has been used for chemical imaging at video rate.[26] Chapter 3 will discuss the relatively new application to standoff detection of chemicals.

2.1 The Non-Linear Susceptibility

Most non-linear optical phenomena involve the creation of a new field or the modification of a field by other fields. Thus, the phenomena can be described by finding expressions for the polarization and susceptibility. In linear optics, the polarization is proportional to the field strength. For example,

$$P = \chi E ,$$

where χ, the susceptibility, is the constant of proportionality. For simplicity, the vector nature of the polarization and the electric field are ignored throughout this discussion, but in general χ is a second rank tensor relating the two vectors:

$$\mathbf{P} = \chi \mathbf{E}.$$

This definition is easily extended to include non-linear effects. The components are separated by order in field strength

$$P(t) = \chi^{(1)}E(t) + \chi^{(2)}E(t)^2 + \chi^{(3)}E(t)^3 + \ldots \tag{2.1}$$

In general, $\chi^{(2)}$ is a third rank tensor and is responsible for sum frequency generation and optical rectification. This susceptibility is only non-zero at interfaces and in non-centrosymetric materials. The 3rd order susceptibility is the primary non-linear susceptibility in most materials due to the prevalence of centrosymmetry. The time dependence is shown explicitly in eq. (2.1). This form assumes an instantaneous response of the medium and no dissipation. Dispersion and dissipation can be incorporated by using a functional form of eq. (2.1), where previous events affect the current polarization. Through most of this document, we will deal with modifications of the field at particular frequencies, and a frequency domain expression is more appropriate.

$$P(\omega) = P^{(1)}(\omega) + P^{(2)}(\omega) + P^{(3)}(\omega) + \ldots$$

Where, for example,

$$P^{(3)}(\omega) = \chi^{(3)}(\omega;\omega_2,\omega_3,\omega_4)\tilde{E}(\omega_2)\tilde{E}(\omega_3)\tilde{E}(\omega_4)\,.$$

$\chi^{(3)}$ is a 4th rank tensor with 81 components. Each component can have multiple terms associated with the wealth of third order phenomena including self focusing, two-photon absorption, and linear and non-linear Raman scattering. The vectoral nature of the polarizability will be ignored for simplicity.

This expression for $P^{(3)}$ shows explicitly that the fields of several frequencies can change the polarization at frequency ω. In the next section, a classical model is used to show how Raman contributions to the third order susceptibility can lead to the creation of new optical fields.

2.2 Classical Calculation of the Third Order Raman Susceptibility

In this section we will use a classical model of a vibrating molecule to calculate the component of $\chi^{(3)}$ due to Raman transitions. This is based on a well known treatment of the subject.[27] This calculation can be done quantum mechanically through perturbation theory,[28] but the classical model provides an intuitive framework to understand all the relevant properties of CARS as well as the SRS measurements discussed in the final chapter.

We model a single molecular vibration as a damped harmonic oscillator with resonant frequency, Ω, damping constant, γ, and deviation of the inter-nuclear coordinate from the equilibrium position, q. The equation of motion is

$$\frac{d^2}{dt^2}q(t) + 2\gamma\frac{d}{dt}q(t) + \Omega^2 q(t) = \frac{F(t)}{m}. \tag{2.2}$$

We will deal with Raman active vibrational modes and thus assume the polarizability changes with q,

$$\alpha(t) \approx \alpha_0 + q(t)\frac{d\alpha}{dq}|_0 = \alpha_0 + q(t)\alpha_0'. \tag{2.3}$$

With many such molecules, coherent vibrations will lead to a modulation in the refractive index of the bulk medium.

$$n(t) = \sqrt{\epsilon_0(t)} = [1 + N\alpha(t)]^{1/2}.$$

This can create new frequencies of light by scattering incident light, as will be shown. First, we show that incident laser light can also be the driving force for these coherent vibrations. The microscopic polarization of a molecule is proportional to the field. Energy is required to establish this polarization, and the work done by the field is

$$W = \frac{1}{2}\langle \mathbf{p}\cdot\mathbf{E}\rangle = \frac{1}{2}\epsilon_0 \alpha \langle E^2 \rangle ,$$

where the brackets denote time averaging over the optical period. Hence, an optical field exerts a compressive or expansive force on the molecule due to the change in polarizability with q,

$$F = \frac{dW}{dq} = \frac{1}{2}\epsilon_0 \alpha_0' \langle E^2 \rangle .$$

The time averaged square of the *E* field is proportional to the intensity, *I*. With two optical fields, $E_p(t)$ and $E_S(t)$, a driving force will be applied at the beat frequency.

$$\begin{aligned} I(t) &\propto |\, E_p(t) + E_S(t)\,|^2 \\ &= |\, E_p\,|^2 + |\, E_S\,|^2 + E_p E_S^* e^{i(\omega_p - \omega_S)t} + E_p^* E_S e^{-i(\omega_p - \omega_S)t} \\ &= |\, E_p\,|^2 + |\, E_S\,|^2 + 2\,\mathrm{Re}(E_p E_S^*)\cos((\omega_p - \omega_S)t). \end{aligned}$$

This leads to an oscillating refractive index. In an extended medium, the collective oscillations will be created in the region of overlap between the two fields. This will create a traveling phase grating with phase velocity at or near (in the presence of dispersion) the speed of light.

If a third laser field is introduced, the phase modulation due to this grating will produce sidebands. This is observed by taking the Fourier transform of the time domain phase modulation, which can be evaluated through the convolution property of Fourier transforms.

$$\tilde{E}_{modulated}(\omega) = FT[e^{-i\phi(t)}E_0(t)] = FT[e^{-i\phi(t)}] * FT[E_0(t)].$$

The phase modulation on resonance will be 90 degrees out of phase with the cosinusoidal driving force and, to illustrate the effect, is approximated as

$$e^{-i\phi(t)} \approx 1 - i\phi(t) \approx 1 - c_1(i\ sin(\Omega t)),$$

and

$$FT[1 - c_1(i\ sin(\Omega t))] \propto c_1(\delta(\omega+\Omega) - \delta(\omega-\Omega)) + \delta(\omega).$$

Thus, the two sidebands are shifted by Ω from the incident field. The spectral intensity is proportional to $|E(\omega)|^2$, which will produce a positive valued spectrum. Depending on the experimental geometry, these new fields may propagate in a new direction (see for example Figure 2.2). This is the general principle of all four-wave mixing. If the beat frequency of the driving fields matches the vibrational frequency of the molecules, this phase grating is greatly enhanced and can survive for some time after the driving fields are turned off. Of the two

sidebands, the red-shifted one represents coherent Stokes Raman scattering (CSRS) and the blue shifted one represents anti-Stokes scattering (CARS). Figure 2.3 shows a schematic of CARS in the spectral domain.

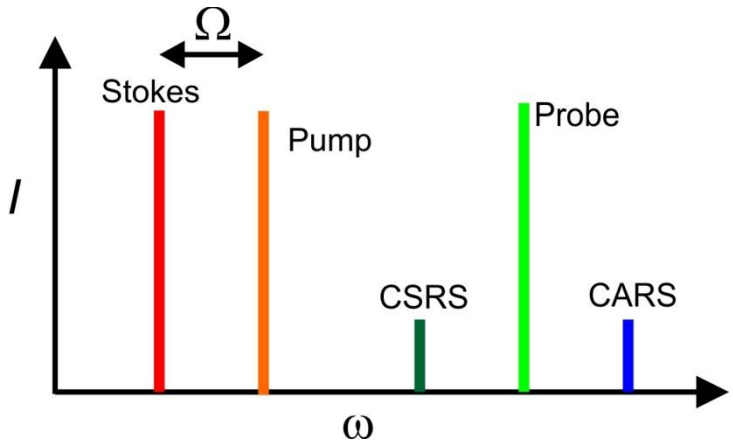

Figure 2.3. Schematic of the CARS and CSRS experiments in the spectral domain. The signals are enhanced if the frequency spacing, Ω, matches the vibrational frequency. Note that the strength of the signals is greatly exaggerated in this schematic.

In order to develop a quantitative framework for coherent Raman processes, let us look at the equation of motion of the nuclear coordinate. The steady state solution to eq. (2.2) using the force due to intensity beating of the two lasers is

$$q(t) \propto \frac{\alpha_0'^2 E_p E_S^* exp(i(\omega_p - \omega_S)t)}{\Omega^2 - (\omega_p - \omega_S)^2 - 2i(\omega_p - \omega_S)\gamma} + c.c.$$

Thus, the macroscopic polarization in the presence of an additional probe using eq. (2.3) is

$$P(t) = \epsilon_0 N \alpha(t) E_{probe}(t) = \epsilon_0 N[\alpha_0 + q(t)\tilde{\alpha}] E_{probe}(t) .$$

The second term contains the non-linear contributions and introduces new frequencies at [ω_{probe} + (ω_p - ω_s)] and [ω_{probe} - (ω_p - ω_s)]. From this term one can find the Raman susceptibility, one term in the multi-component third order susceptibility. Considering the polarization at frequency $\omega_{CARS} = \omega_{probe} + (\omega_p - \omega_s)$, we can write

$$P^{(3)}(\omega_{CARS}) = \chi^{(3)}(\omega_{CARS}; \omega_{probe}, -\omega_S, \omega_p) E_{probe} E_S^* E_p ,$$

where

$$\chi^{(3)}(\omega_{CARS}; \omega_{probe}, -\omega_s, \omega_p) = \frac{\epsilon_0 (N/6m)\tilde{\alpha}^2}{\Omega^2 - (\omega_p - \omega_s)^2 - 2i(\omega_p - \omega_s)\gamma} .$$

The CARS signal is proportional to the modulus square of the induced polarization,

$$I_{CARS} \propto |\chi|^2 \, | E_{probe} |^2 | E_s |^2 | E_p |^2 .$$

From the expression, we see the CARS signal scales cubically with laser intensity and quadratically with molecule number. A similar expression is obtained by considering the

polarization established at frequency $\omega_{CSRS} = \omega_{probe} - (\omega_p - \omega_s)$. This is coherent Stokes Raman scattering (CSRS). This signal will be approximately the same strength as the CARS signal. CSRS may overlap with the single-photon fluorescence signal, therefore CARS is preferred for nearly all applications.

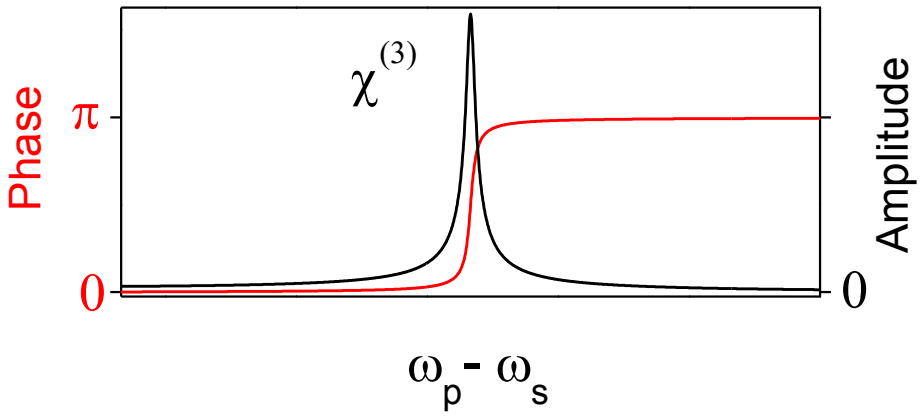

Figure 2.4. Plot of the χ term responsible for CARS as a function of excitation frequency near the resonance. At high driving frequencies, the susceptibility responds 180 degrees out of phase.

The susceptibility is plotted as a function of driving frequency in Figure 2.4. The phase of the susceptibility changes as the beat frequency is tuned through the resonance. On resonance, the driving force will be 90 degrees out of phase with the molecular motion. Below resonance, the polarization will oscillate in phase. This change in phase through the resonance can lead to distortion of the recorded line-shape if the signal is mixed with another field.

2.3 The Non-Resonant Background

As shown in Figure 2.1, CARS is a parametric process in which photons are exchanged between frequencies but the material is returned to the initial state. This process can also occur off-resonance, and the corresponding signal is referred to as the non-resonant background. In microscopy, this background is undesirable because it reduces contrast and can distort line-shapes. The effect can be devastating for standoff detection because the signal is always present to varying degrees, making absolute detection impossible. Since the first experiments, most of the research in CARS microscopy is directed toward eliminating this background.

The non-resonant background is a coherent signal and can therefore interfere with the resonant CARS signal.

$$I_{CARS} \propto |\chi_R + \chi_{NR}|^2 = |\chi_R|^2 + |\chi_{NR}|^2 + 2Re(\chi_R \chi_{NR}^*),$$

where χ_{NR} is the non-resonant susceptibility, and χ_R is the resonant.

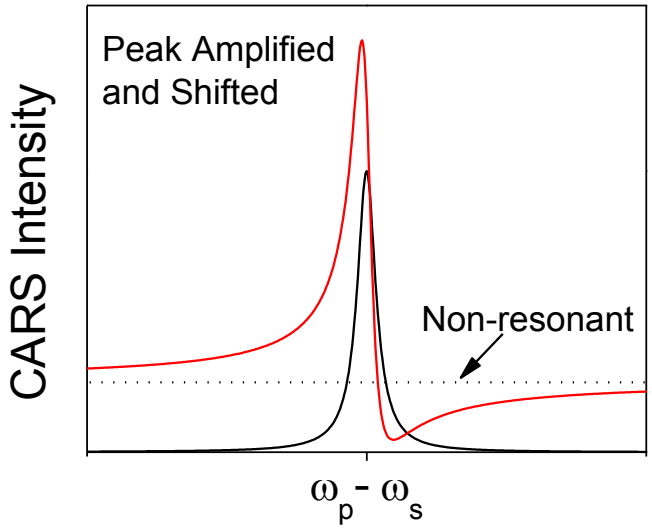

Figure 2.5. Simulated CARS spectrum near a resonance with and without a non-resonant background. Note the signal is amplified slightly and shifted. Larger non-resonant backgrounds will have a more severe effect.

The non-resonant background is smoothly varying with the driving frequency and has a constant phase. This can lead to a dispersive line-shape in the presence of a resonance, and peak shifts in the frequency resolved spectra. This is observed in the simulation plotted in Figure 2.5.

2.4 Common Implementation (Two-Color CARS)

Two laser beams are enough to do spectroscopy or chemically image with CARS. These lasers are almost always pulsed, providing the peak intensity required for non-linear processes without depositing too much energy. The pump and Stokes lasers will create the coherence if their frequency difference matches the transition. The pump laser is used as the probe beam, ensuring a blue shifted CARS signal with no laser interference. This requires the synchronization of two

laser pulse trains and delay stages to make the two pulses arrive at the sample at the same time. Often, an optical parametric oscillator, or another method of frequency conversion, is used to create one of the beams and ensure synchronization. A short-pass optical filter and photo-detector enables detection free from laser interference. Tuning the wavelength of one of the lasers can produce a spectrum.

This "simplest" implementation suffers due to the non-resonant background, which limits image contrast and distorts spectra. For standoff detection, the non-resonant background is very detrimental; since there will always be signal, absolute detection is impossible. Many complicated variations have been developed in order to reduce or eliminate this background. We will focus on the four key approaches: time delayed probe, polarization methods, phase cycling, and spectral analysis. All of these methods decrease signal intensity or increase acquisition time.

1. A resonant excitation field (pump and Stokes) will produce a transient phase grating that persists after the excitation field is turned off, while non-resonant excitation will not. Thus, introducing a third beam to serve as a time delayed probe can produce non-resonant free CARS signal. However, the CARS signal quickly dephases and, in most instances, the magnitude of the signal is significantly reduced. If very short pulses are used, the dephasing can be avoided but short pulses have a broad bandwidth and energy resolution will suffer. It is noted that a delayed probe will not resolve the signal from broadband, rapidly dephasing vibrational modes.

2. By carefully choosing the polarization of the three fields, there will be a slight difference in the polarization angle of the non-resonant signal and the resonant signal. Using a polarizer before detection can eliminate the non-resonant background while allowing some of the resonant signal to transmit.[29] This reduces the signal since much of it is blocked by the polarizer.

3. Adding a field at the frequency of the signal allows measurement of the relative phase. The two fields will interfere in a manner depending on their relative phase and by cycling the phase of this added field (local oscillator), one can measure the phase of the CARS signal and isolate the resonant component.[30]

4. The non-resonant background is smoothly varying with respect to frequency compared to most Raman features. Thus, a spectrum provides a way to distinguish the two contributions. This will require wavelength tuning in the two beam CARS setup which can be time consuming and complicated. There are reasonably good computational methods available to remove the distorting effects of the mixing term (see Figure 2.5).[31]

With the single beam method described in the next section and subsequent chapter, the spectrum is produced without wavelength scanning, and the time delayed probe approach to non-resonant reduction is easily implemented.

2.5. Single Beam CARS

In the last section, we concluded by describing the traditional multi-beam approach to CARS. These techniques are quite complicated and require overlapping multiple pulses in time and space within the sample. Further, laser tuning is required to measure multiple Raman transitions. This section describes the principle of single-beam CARS and a few experimental implementations.

2.5.1 Principle

A pulsed laser cannot operate at a single wavelength due to the relationship between time and frequency (see Appendix B). The shorter the pulse is in time, the broader the required laser bandwidth. As an example, a 1 fs visible laser pulse requires a bandwidth spanning the entire visible spectrum. Such a laser can be made in the laboratory with great expense, but 10 fs laser systems in the near IR are sold commercially. The carbon/hydrogen bond stretching vibrations correspond to a Raman frequency near 3000 cm^{-1}. These are the highest frequency modes of interest in most molecules and have a period of ~10 fs. It can be shown that, a 10 fs laser contains the appropriately spaced frequencies required for two beam CARS at <3000 cm^{-1}. By filtering out the unwanted laser light, CARS measurements can be performed with a single laser (see Figure 2.6). This dramatically simplifies the laser setup.

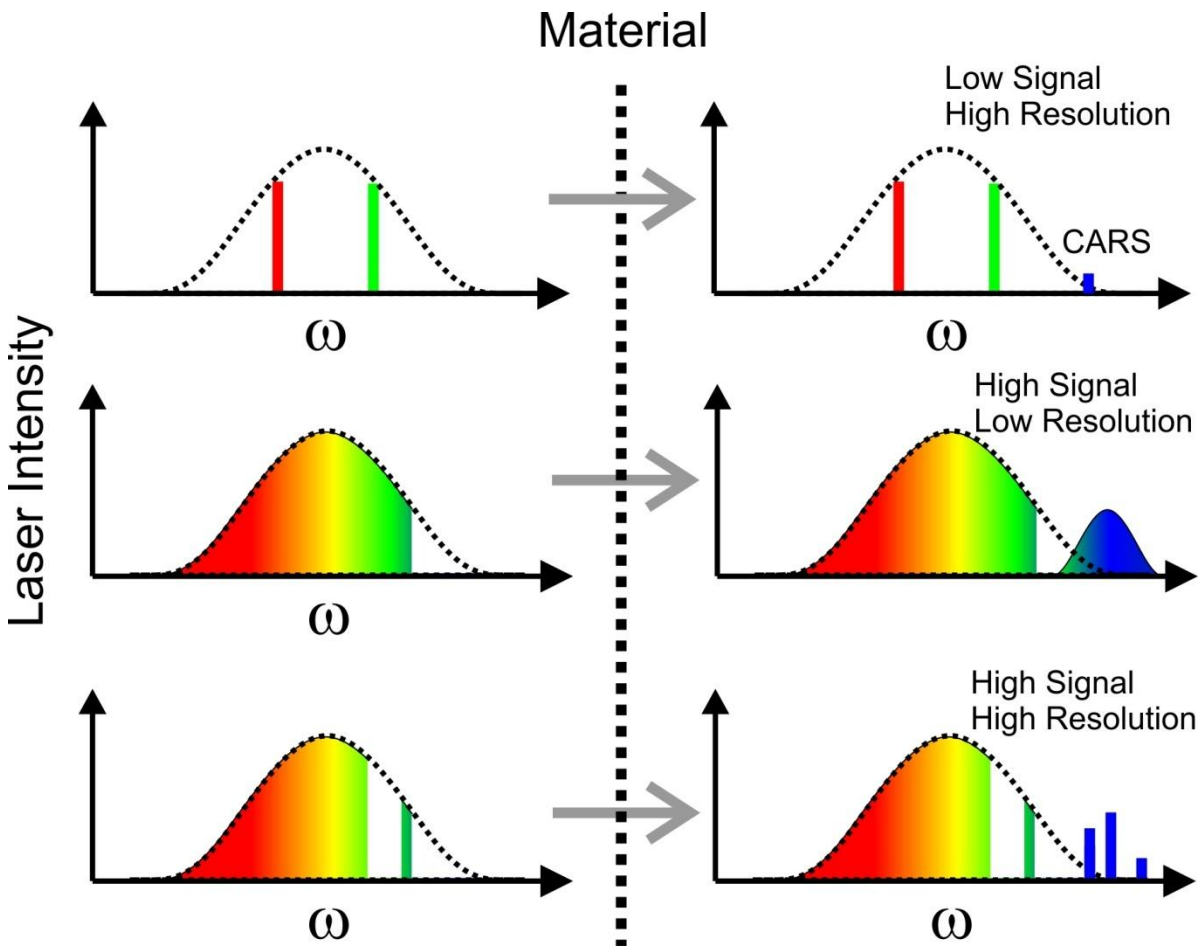

Figure 2.6. Schematic of possible implementations of single-beam CARS. The first is identical to two color CARS, but most of the laser power is eliminated, which produces a weak CARS signal. The second provide large CARS signal, but little energy resolution in the convoluted signal. The final implementation has high resolution and strong signal.

This approach is unattractive since the vast majority of the laser light is discarded and the CARS signal is cubic in laser intensity. However, if the laser is left unfiltered, the intense laser pulse will excite many Raman modes with great efficiency. These modes can be resolved by introducing a narrowband probe, which can be carved out of the broadband spectrum (see Figure 2.6). In terms of the classical model developed in the previous chapter, the intense pulse compresses the molecules, which then begin to oscillate at their respective frequencies. The phase grating then has a several frequency components from which the probe can scatter. In

addition to providing automatic overlap of all frequency components, there is the added benefit that a spectrum can be acquired in a single shot with no tuning of the laser wavelengths.

It was already stated that filtering the broadband laser down to two wavelengths will result in poor signal. In fact, the single-beam CARS approach will produce much stronger signal at a given anti-Stokes shift. This may be puzzling at first, but is because there are not just two laser wavelengths contributing to the signal for a particular anti-Stokes shift. All wavelengths with an appropriately spaced partner will contribute to the signal.

2.5.2 Experimental Application

Single-beam CARS was first demonstrated in microscopy by the Silberberg group.[32] Since this time, several groups have improved the results or implemented alternate setups.[33–36] However, several difficulties have prevented widespread adoption of this technique for microscopy and multi-beam approaches remain much more common.

The most successful CARS microscopy setups look exclusively at the C-H stretches. In biological tissue, these modes are plentiful but distinct enough in the different tissue to allow meaningful chemical contrast. As previously stated, the carbon-hydrogen stretches are the highest frequency modes of most molecules (~3000 cm^{-1}) and require a sub ~10 fs pulse to excite in a single beam setup. This poses several experimental challenges. These lasers are available commercially, but the power can be quite low. In addition, dispersion has severe consequences on such short pulses, and the microscope objectives required for tight focusing

with broadband light sources utilize many glass elements introducing significant dispersion, which lengthens the pulse in time (see Appendix C). Last, only the edge of the bandwidth contributes to the signal, making the efficiency significantly less than that of two-color CARS.

Observing the Raman modes in the fingerprint region (~200-1500 cm^{-1}) is extremely important for molecular identification, as the name suggests. However, microscopy in this region is rare due to the low concentration of any particular molecule in biological tissue.

3. CARS Standoff Detection

As stated, CARS microscopy is most successfully applied to the C-H stretches where the sample number is large enough to generate substantial signal. In macroscopic applications, the larger sample volumes enable scientists to look at the lower wavenumber modes, referred to as the "fingerprint" region (~200-1500cm^{-1}), which is very useful in molecular identification. The applications include gas phase measurement (e.g. combustion studies) and standoff detection. For these applications, the bandwidth requirements are not as extreme and the advantages of single-beam CARS are realized. Limited results from gas phase measurements are presented in Appendix A.

This chapter describes the application of single-beam CARS to standoff detection. The largest section is devoted to the initial work of the author in demonstrating the sensitivity and specificity of single beam CARS for standoff detection.[37] Some figures and descriptions are reproduced with permission from these references.[37,38] First, the CARS based standoff detection work is reviewed to make the authors contribution clear.

3.1 Prior Standoff Detection Efforts

In 2005, Marlan Scully outlined the possibility of using CARS to detect anthrax endospores at large standoff.[39] Three years later, his group demonstrated detection of trace quantities of bacterial endospores.[40] This was achieved with a microscope objective and cannot be considered standoff detection, although the signal was collected in the backscattered direction. Since then, most of the effort from this group has been focused on detection of anthrax within envelopes, not standoff detection. Their recent demonstration of backward lasing in air, however, could have significant impact on remote sensing in the long term.[41]

The first CARS based standoff detection measurements were performed by the Dantus group with a single beam setup.[42] The CARS spectrum of various chemicals were detected at 12m standoff, including solids, gasses, and liquids. In most instances, a mirror was placed behind the transparent sample to retro-reflect the generated CARS signal. For two samples, xylene and toluene, the liquid was applied to a collection of silica micro-beads, which form a diffusely reflecting surface, and the mirror was removed. The utility of selective excitation of particular Raman modes was also demonstrated, but will be discussed further in Chapter 4. The paper provides a proof of principle for detecting small amounts of materials at modest standoff. A subsequent paper explicitly demonstrates the standoff detection of a compound present at 2% within a binary mixture.[43]

Shortly after this initial work, two Israeli groups published useful research toward standoff detection of explosive traces. Silberberg's group used single-beam CARS to detect sub-milligram quantities of explosives at >10 meters without a retro-reflecting mirror,[44] and they extended this to 50 m in 2012.[45] Portnov *et al.* quantified the increase in signal of CARS over Raman for standoff detection from scattering surfaces, reporting an enhancement of ~10^4.[46] This work was implemented with a multi-beam setup, and it must be noted that this enhancement depends on several parameters, including sample volume and laser power.

When I joined the Dantus group in 2009, we were tasked with exploring the limits of standoff detection with single-beam CARS through a grant from the Department of Homeland Security. Specifically, what is the sensitivity and selectivity of single-beam CARS when applied to trace quantities of explosive simulants deposited within a complex chemical background at modest standoff? The previous proof-of-principle studies indicate significant promise for the CARS approach to standoff detection, but no clear metrics of performance. An honest assessment involves pushing the technique to the limit of performance. This requires understanding the limiting contributions to spectral resolution and signal generation and advances in the experimental setup.

3.2 Experimental Setup

In the following, the experimental setup is described in detail. This includes the laser and spectral broadening technique used in previous publications. The author's contribution begins with the design of the modified pulse shaper. The setup is altered for the SRS measurements in Chapter 5 and will be detailed there.

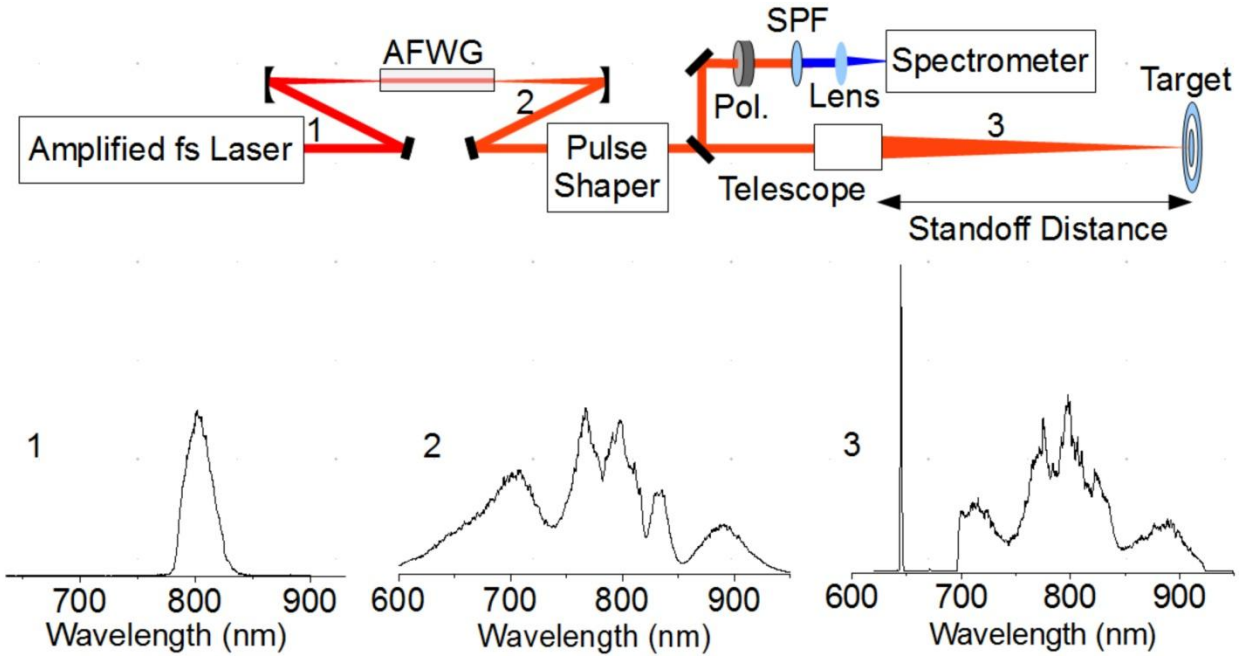

Figure 3.1. Experimental setup (a). An amplified laser is spectrally broadened within the AFWG, shaped and temporally compressed by the pulse shaper, and focused on the sample. The signal is collected and resolved by a spectrometer after passing through a polarizer (Pol.) and short-pass filter (SPF). The spectrum of the laser at several locations in the experimental setup is shown in the lower half. AFWG: argon filled wave guide, SPF: short-pass filter.

A schematic of the setup is shown in Figure 3.1. The femtosecond oscillators used for single beam CARS microscopy do not provide enough pulse energy for standoff detection because of the much smaller numerical aperture. CARS signal is proportional to intensity cubed, so peak

power, rather than average power is of primary concern. Thus, an amplified femtosecond laser is required. The details of the laser system are available in the appendix, but it can deliver 35fs, 1mJ pulses centered at 800 nm at a 1 kHz repetition rate. This output is spectrally broadened through a non-linear process within an argon filled waveguide. This pulse is compressed and shaped by the pulse shaper (see next section) and focused on the sample, one meter away. The shaped spectrum consists of a broadband pump/Stokes portion and a narrowband probe on the blue side of the spectrum with orthogonal polarization. The average power of the laser never exceeds 8 mW (8 µJ pulse energy) and is focused to a spot roughly 100 µm in diameter. The signal is collected with a small lens adjacent to the focusing mirror. It is then directed through a polarizer and short pass filter (650 nm) before being coupled into a spectrograph. The orthogonal polarization of the probe helps eliminate the background due to the excitation pulse acting as a probe.

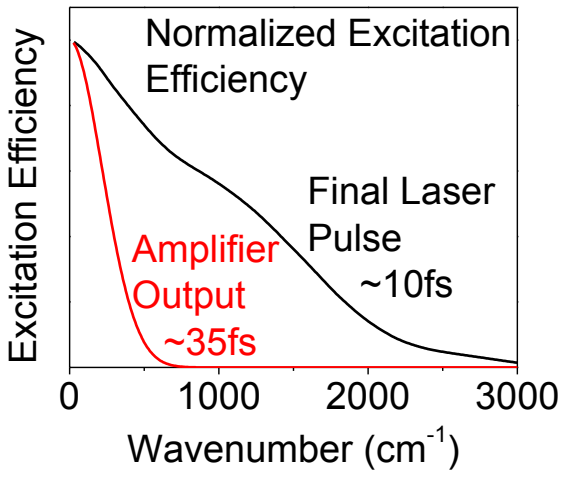

Figure 3.2. The computed excitation efficiency for the initial and final spectra in Figure 3.1.

In general, amplifiers limit the bandwidth to the laser and prevent access to high frequency vibrational modes. The 35fs pulse in the setup places this limit at less than 1000 cm^{-1} (see Figure 3.2). Thus, the bandwidth must be increased. This is achieved through self phase modulation in an argon filled capillary as first utilized by Nisoli *et al.*[47] Self phase modulation is a third (or higher) order non-linear process related to the intensity dependent index of refraction. The index of refraction experienced by the most intense section of the pulse is different from that of the weaker portions. They travel at different speeds and new frequencies are created in analogy to the Doppler Effect. The resulting spectrum is the second spectrum presented in Figure 3.1. This spectrum can be compressed to a <5 fs pulse.[48]

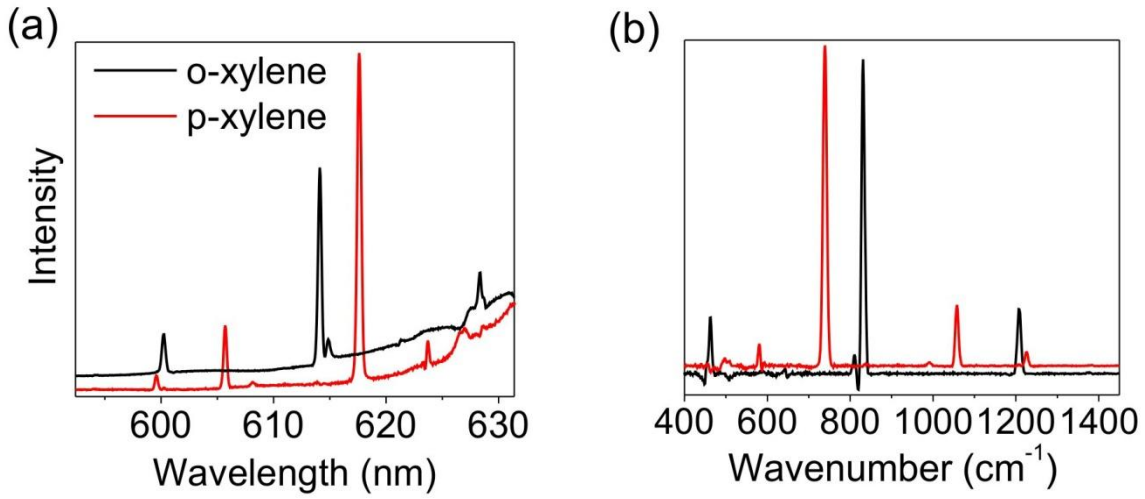

Figure 3.3. Example single-beam CARS spectra from two isomers of xylene. (a) Blue shifted CARS signal as observed with spectrometer. (b) CARS spectrum plotted in wavenumber units with respect to the probe frequency. In both figures, the spectra are vertically offset for clarity. The resolution is two orders of magnitude better than the excitation range.

High resolution CARS spectra acquired with the setup are shown in Figure 3.3. Raw data is shown in 3.3 (a) and the processed spectrum shown in 3.3(b). The sharp resonant features ride

on top of a broad, smoothly varying non-resonant background in the raw data. This background is quite low in comparison to that typically observed with two-color CARS due to the time delay of the probe. Further delaying the probe can eliminate the background, but results in significantly reduced signal. Only the quickly varying spectral features are retained in the processed spectrum.

3.2.1 Pulse Shaping

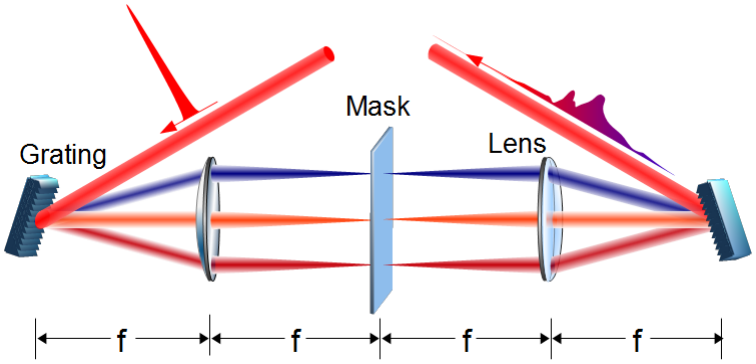

Figure 3.4. Schematic of a 4-f pulse shaper. The grating angularly distributes the different frequency components. A lens maps this angle to a position at the Fourier plane. This is where the mask or SLM is located. The mask controls the spectrum by attenuating different components or changes the spectral phase by increasing the optical path (e.g. introducing glass).

Pulse shaping is achieved through an interesting optical device called a 4-f pulse shaper. The principle of this device is to manipulate the pulse in the frequency domain, thereby producing the desired pulse in the time domain through Fourier synthesis. A diagram of the design principle is shown in Figure 3.4. A collimated broadband laser is chromatically dispersed with a grating or prism located one focal length from a lens. The lens maps the angle of incidence to the Fourier plane, one focal length away. A *spatial light modulator* (SLM) at the Fourier plane can block certain wavelengths, performing amplitude shaping, or introduce a change in the optical path

length, performing phase shaping. In our lab, the SLM is a computer controlled liquid crystal device which can provide phase and amplitude shaping. An identical setup recombines the frequency components to synthesize the pulse. Often, a mirror is placed at the Fourier plane to retro-reflect the laser and fold the setup in half. Appendix C describes some basic phase-shapes and the resulting time domain pulse profiles.

In this chapter, the pulse shaper is used to compensate for dispersion, delivering the shortest pulse possible to the target, and for amplitude shaping, to define the probe. In later chapters, the pulse shaper will be used in more interesting ways (e.g. coherently control the population of vibrational states). Dispersion, in which different wavelengths experience different optical paths, can be detrimental to short laser pulses and is present in all materials. Short pulses will lengthen in time, reducing the peak intensity and the strength of non-linear effects. The broader the bandwidth, the more important dispersion becomes. As an example, a 5 fs, transform-limited (TL) pulse centered at 800 nm (necessitating a broad bandwidth) will be stretched to 60 fs after propagating 10 meters in air, while a 30 fs transform-limited pulse will stretch only to 35 fs. A technique called multiphoton intrapulse interference phase scan (MIIPS), developed in the Dantus lab, is used to measure the phase distortions and compress the pulse using the pulse shaper.[48]

3.2.2 Modified Pulse Shaper

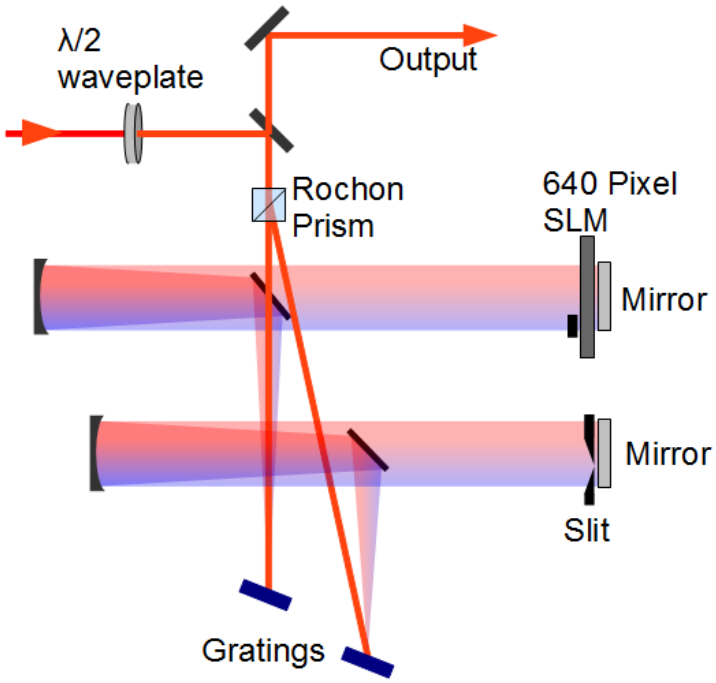

Figure 3.5. Schematic of the modified pulse shaper used in the experiment. The Rochon prism sends each polarization component to a different pulse shaper. The waveplate controls the relative intensity of each shaped component. A delay stage in the probe arm (not shown) controls the relative timing of the two components.

In order to improve performance, several modifications were made to the general pulse shaper design and shown schematically in Figure 3.5. These changes are simple but result in significant improvements in signal intensity, background suppression, and energy resolution. The author is responsible for this design, so a detailed description is provided. The goals of the changes are to provide the high power probe with ideal resolution and orthogonal polarization. While a traditional dual mask SLM is capable of polarization or amplitude shaping in addition to phase shaping, here we have effectively created two shaping apparatuses, one for each polarization component. An achromatic waveplate rotates the polarization of the laser and the Rochon prism passes the horizontal component to the traditional SLM based shaper. The vertical component is

directed to a simple folded 4-f shaper which selects a narrowband feature with a slit at the Fourier plane. The two components are recombined within the Rochon prism. This is fundamentally similar to other so called “full control” pulse shapers (amplitude, phase and polarization) that spatially separate polarization components before spectral shaping in a 4-f shaper.[49,50]

There are three benefits of this setup. First, the Rochon prism offers a high contrast ratio ($>10^4$) and accordingly good polarization based background suppression. Second, a tradeoff between excitation bandwidth and probe resolution occurs with the 640 pixel SLM, which is avoided by the use of a slit at the Fourier plane in the probe arm. Finally, amplitude shaping is possible in this scheme, allowing reduction of the ultra-short (~7fs) excitation pulse energy below the damage threshold while retaining the maximum intensity in the harmless probe pulse (picoseconds).

Similar advantages could be realized through alternative methods, with a narrowband filter (this would be quite expensive) and polarization optics, for example. However, the additional pulse shaper offers versatility. The wavelength can be varied by rotating the grating, and the bandwidth is controlled by the width of the slit at the Fourier plane. Interesting multiple-probe configurations can be arranged, for example, to measure dephasing rates as shown in the next Appendix A. Finally, the setup, while "multi-beam" in nature since not all optics are common, is essentially alignment-free. As long as the back mirror of both shapers is located at the Fourier plane, the two beams will always focus to the same spot. In addition, the probe beam is easily

offset by tilting the back mirror, which will reduce the region of overlap at the focus in the axial direction and increase the 3D sectioning ability of the technique.

3.2.3 Target Preparation

The technique was tested on the explosive simulant dinitrotoluene (DNT) deposited within a polymer/solvent matrix, either poly-methylmethacrylate (PMMA) or poly-styrene (PS) dissolved in toluene. The polymer represents a complex chemical background in which the analyte is to be detected. The mixture was applied as a thin film to a gold-coated silicon wafer substrate. The mirror like surface ensures that all of the signal can be collected and provides a flat surface on which a thin film can be deposited uniformly. By measuring the film thickness, the surface concentration of the analyte can be determined. Film thicknesses range from 200 nm to 5 μm, measured by ellipsometry or thin film interference, and DNT concentrations are between 2-10% by mass excluding the mass of the solvent which mostly evaporates after deposition.

3.3 Results: Spectra

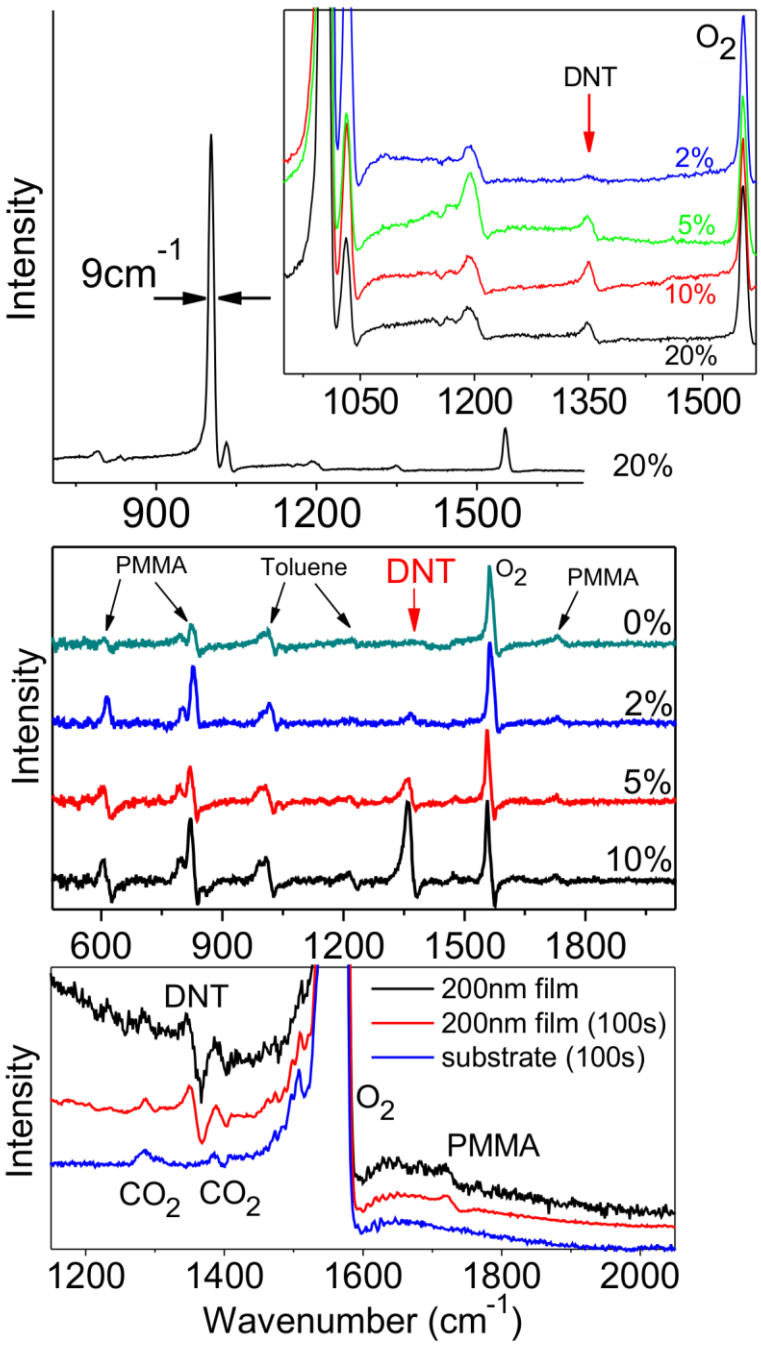

Figure 3.6. CARS spectra acquired at 1 meter standoff on <5 µm PS (a), <2.5 µm PMMA films (b), and 200 nm film containing 10% DNT (c). Percentages refer to the concentration of DNT in the film relative to polymer mass. Unprocessed (a) and processed data (b) both show detection of the 1350 cm^{-1} DNT feature at 2% concentration. Unprocessed data in (c) shows signal from a blank substrate (blue) and 200 nm film (red) integrated for 100 s to clarify features in the low

signal to noise 1s exposure (black). CO_2 and the ro-vibrational features of O_2 are also visible in (c).

CARS spectra obtained from PS and PMMA films containing various concentrations of DNT at one meter stand-off and with 1 second of collection are shown in Figure 3.6. The CARS lines from PS, PMMA, residual toluene, and air form a complex background in which the 1350 cm^{-1} DNT feature is still visible at 2% concentration. The surface DNT concentration in the 2% PS film is <10 $\mu g/cm^2$ (Fig. 2a) and <5 $\mu g/cm^2$ in the 2.1 μm thick 2% PMMA film (Figure. 3.6b). Additional features of air and signal from 2 $\mu g/cm^2$ of DNT are observed in Figure 3.6c. The dispersive line-shapes are due to mixing with the non-resonant background.

3.4 Results: Images

To demonstrate the power of the technique in regards to offering high sensitivity and excellent specificity simultaneously, an imaging modality is introduced. The standoff CARS images are created by raster scanning the sample and monitoring the peaks in the generated spectrum. To make data collection easier, the sample, as opposed to the laser, is moved to create the raster images. By monitoring the spectra and measuring intensity at a particular wavenumber and subtracting the intensity at an adjacent value, chemical images were created. In this way, each scan creates a three dimensional data set, two spatial and the third energy. Each image is a slice of this data set; examples of such images are shown in Figures 3.7 and 3.8.

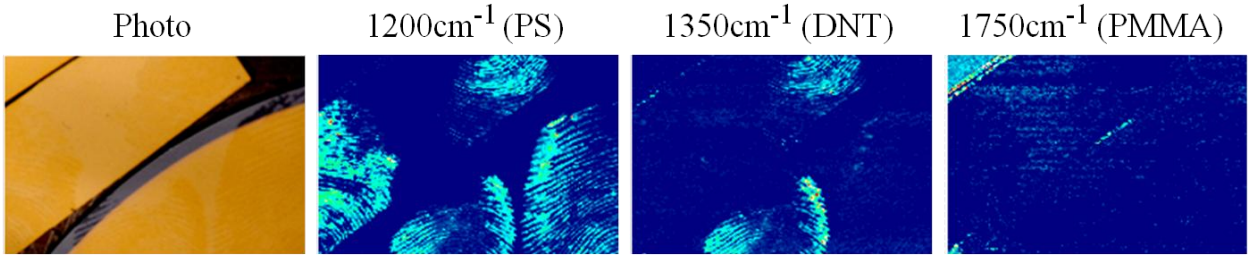

Figure 3.7. CARS images of polystyrene fingerprints on three gold-coated wafer pieces. The title on each image refers to the resonance monitored. Each pixel represents the CARS signal from 500 laser pulses. Only two of the four fingerprints contain a small amount of DNT, and the wafer in the upper left has a 5μm PMMA film. Note there are virtually no false positives even with the small quantities considered, and all images were acquired simultaneously.

Standoff chemical images of fingerprints are shown in Figure 3.7. The fingerprints were created by dipping a finger in a polymer solution and repeatedly pressing it on surfaces until a clean print was observed (visible in the photo). Two solutions were used, one with DNT and one without. The images clearly show which fingerprints contain DNT. The third chemical image shows no signal from the fingerprints because they do not contain PMMA, however, there is signal from the 3 μm thick PMMA film on the wafer located upper left. The images show very high chemical specificity from small quantities of chemicals.

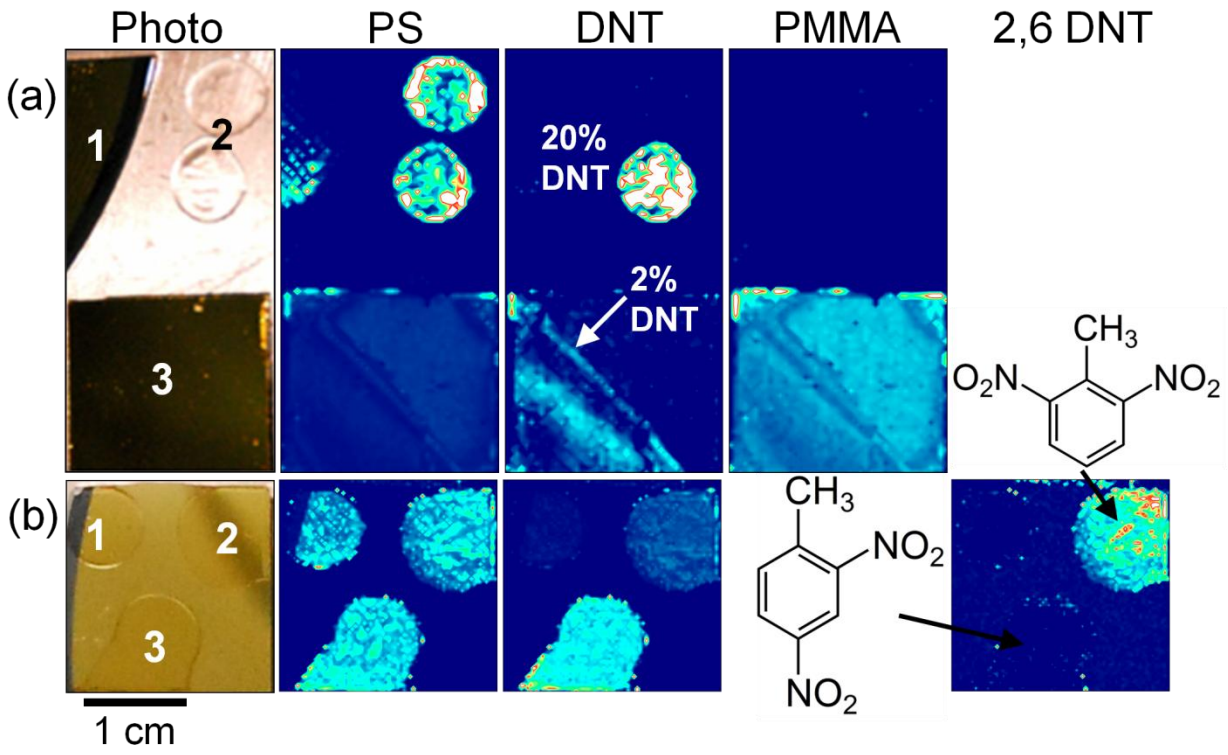

Figure 3.8. Two samples are shown. (a) 1: a PS fingerprint, 2: two ~100 µm thick drops of PS, 3: 3 µm film of PMMA. Sections 1 and 3 of this sample have gold-coated wafer substrates. Section 2 is an aluminum substrate. Only half of the thin film and one of the drops contain DNT. Image is 50x100 pixels. (b) three 3 µm films of PS. Two contain 20% DNT, one of which is the 2,6 isomer. Image is 50x50 pixels. Title of each chemical image refers to the resonance monitored: PS: 1200 cm^{-1}, DNT: 1350 cm^{-1}, PMMA: 1750 cm^{-1}, and 2,6-DNT: 1090 cm^{-1}.

Figure 3.8 displays more quantitative examples of standoff chemical images. In 3.8a, DNT is only present in the lower left half of the film and one of the drops. The concentration of DNT in the film is 5 µg/cm^2, demonstrating similar sensitivity to the spectroscopy in an imaging mode. There is an absence of false positives in all panels except PS where we see signal from the PMMA film. This is because the solvent used in spin coating, toluene, also has a resonance at 1200 cm^{-1}. In 3.8b, discrimination between isomers of DNT is used to demonstrate the versatility and selectivity of the method. The 1350cm^{-1} resonance, which is the NO_2 symmetric

stretch, is shared by both compounds. The 1090 cm^{-1} resonance is only present in the 2,6 isomer.

3.5 Conclusions

We have demonstrated the sensitivity and selectivity of a CARS standoff detection method. The method can provide $\mu g/cm^2$ detection sensitivity within a complex chemical background within one second. This is accomplished with a laser producing less than 8mW of average laser power in the near IR. This concentration is in line with that which is expected from a latent fingerprint after handling explosives.[7]

The chemical images presented provide good examples of the benefits of this technique. High sensitivity and excellent chemical specificity are clearly demonstrated in the standoff chemical images. In addition, the high resolution and sensitivity to low concentrations within sub-millimeter areas identifies samples which would be very challenging for alternative standoff methods. This is in contrast to the sensitivity demonstrated by most linear methods, wherein a large laser spot is used to acquire signal from a comparatively large mass of analyte with low average surface concentration.

Many reports on standoff detection focus on total mass detection. For comparison, we explicitly calculate 2 $\mu g/cm^2$ is equivalent to ~$2x10^{-10}$ g within the focal spot area of our laser. We

contrast that to the mass of a $1mm^3$ crystal of DNT which would have a 10^7 greater mass. These results show great promise for non-destructive imaging and sensing of hazardous materials in a standoff configuration.

4. Coherent Control of Raman Processes

This section describes selective excitation of particular Raman modes with a broadband laser. Using a pulse shaper, the spectral phase of the laser can be manipulated such that only one or a few Raman modes will be excited despite the broad bandwidth. This is interesting to many people working in the field of quantum chemistry as it can be described as coherent control of molecular vibrations and may be useful in the broad goal of coherent control of chemical reactions. For practical applications, like standoff detection, it seems less appealing since a spectrum is generally more useful than knowledge of a single resonance. However, there are a few very important attributes outlined in the last section of this chapter. The ideas are developed in terms of CARS experiments, which aligns with history, but the concept is integral to the SRS detection method described in the final chapter. The final section gives a detailed description of a CARS imaging method, designed by the author, that will clarify many of the features of selective Raman excitation.

4.1 Background

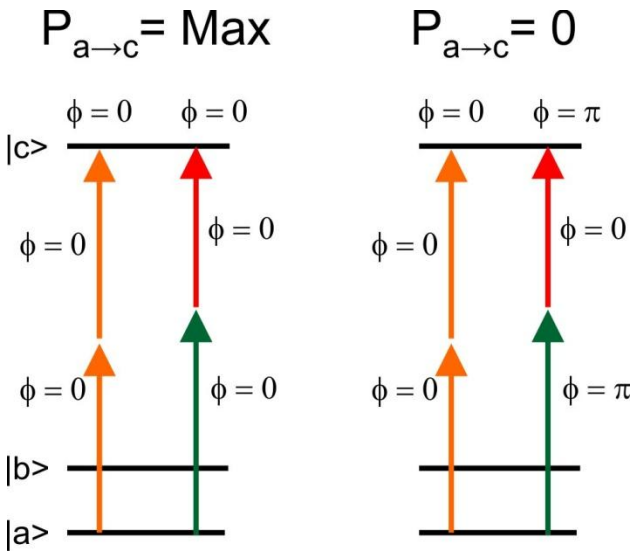

Figure 4.1. An energy level diagram of two-photon absorption in the presence of three lasers. This is a two-photon process, but interference between multiple two-photon paths can eliminate the excitation. This example uses only three discrete photon energies, but the same interference is observed with broadband pulses.

When using a broadband laser for multiphoton processes, there are many possible pathways of excitation available. For example, two photon excitation of a 3.1 eV transition can be accomplished with two 1.55 eV photons or a 1.5 eV and 1.6 eV photon. All of these are available in a 20 fs pulse centered at 800 nm. These two pathways can interfere through the accumulated phase in each path, in analogy with double slit interference in wave mechanics. This is shown schematically in Figure 4.1. This phase can be controlled through the spectral phase applied with a pulse shaper, controlling the probability of a particular transition. With the proper phase, one transition can be virtually eliminated while retaining maximum probability of an adjacent transition. This was demonstrated experimentally in 1999 by Yaron Silberberg's group.[51] In general, there will be maximum excitation at the point of antisymetry in the spectral phase since the phase of the photons equidistant from this point will sum to zero.

This same interference can occur in Raman processes. This was observed experimentally nearly a decade earlier by Weiner *et al.*, and explained classically.[52] Using a periodic spectral phase, they transformed a 75 fs pulse into a train of short pulses several picoseconds long. When the period of the pulse train matched a vibration in the material (either 80 cm^{-1} or 104 cm^{-1} in the α-peryline crystal) the corresponding modes were observed in a time domain CARS measurement.

Using the classical model developed in chapter two, the first pulse in the train will impulsively excite all vibrational modes with period less than the pulse duration. A future pulse, that arrives an integer number of vibrational periods later, will further drive this particular vibration. If the period of the pulse train does not match a particular mode, these pulses may damp this vibration. In this way, Raman active modes can be selectively excited. The excitation becomes increasingly selective as the length of the pulse train is increased. The excitation efficiency will be the square of the Fourier transform of the time domain intensity profile, as shown below.

4.2 Selective Excitation of Raman Modes Described by Perturbation Theory

A semi-classical description of impulsive Raman excitation shows how the interference from multiple excitation paths can lead to selective excitation. This analysis follows one presented by Meshulach and Silberberg based on time dependent perturbation theory.[51]

Consider a two level system in the ground state with a weak excitation from an ultra-short laser pulse. First order perturbation theory predicts for the amplitude of the excited state,

$$a_b(t) \propto \mu_{ba} \int_{-\infty}^{t} E(t_1) \exp(i\omega_{ab} t_1) dt_1 .$$

Assuming the excitation pulse is short compared to the lifetime of the state, the amplitude of the excited state after the excitation pulse can be determined by allowing the integration limits to go to infinity. The probability of excitation is the modulus squared of the transition amplitude, and in this case, is proportional to the square of the Fourier component of the field at $\omega = \omega_{ab}$.

$$P_{a \to b} \propto | \tilde{E}(\omega_{ab}) |^2 .$$

In our experiments, the excitation field is assumed to be off resonant and only second order processes will contribute. Consider the three level system shown schematically in figure 4.2, where |a> is the ground state, |c> is an excited electronic state, and |b> is an excited vibrational state.

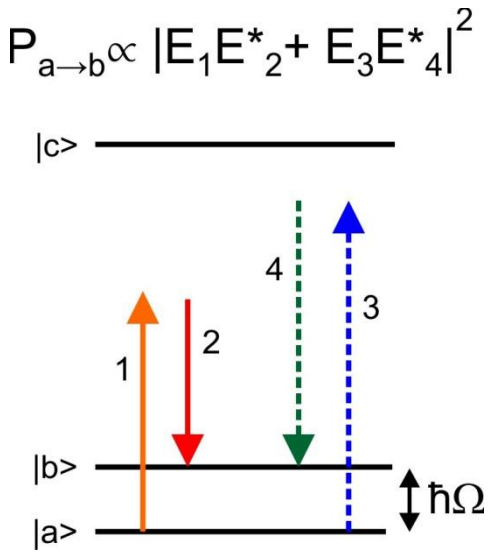

Figure 4.2. Energy level diagram of Raman excitation of a vibrational level involving two possible pathways. The transition amplitude is the sum of the two paths. The transition probability is the square of this amplitude and contains interference terms.

To second order, the transition amplitude of the Raman active transition is

$$a_{ab}(t) \propto \sum_n \mu_{bn}\mu_{na} \int_{-\infty}^{t} E(t_1) exp(i\omega_{bn} t_1) \int_{-\infty}^{t1} E(t_2) exp(i\omega_{na} t_2) dt_2 dt_1,$$

where *n* is the intermediate virtual state. Making the assumption that the virtual states have very short lifetimes (comparable to the inverse of the optical frequency, ω), and the strength of the contributions of different pathways are similar, the following approximation is obtained.[51]

$$a_{ab}(t) \propto \int_{-\infty}^{t} E(t_1) exp(i\omega_{bn} t_1) E(t_1) exp(i\omega_{na} t_1) dt_1,$$

or simply

$$a_{ab}(t) \propto \int_{-\infty}^{t} E^2(t) exp(i\omega_{ba} t) dt. \qquad (4.1)$$

Again, evaluating at infinity, the transition amplitude is proportional to the Fourier component of the *intensity* at the vibrational frequency. This is expected from the classical model. Transforming to the frequency domain, the interference between multiple pathways can be observed. Using Parseval's identity, equation (4.1) can be written,

$$a_{ab} \propto \int_{-\infty}^{\infty} \tilde{E}^{*}(\omega)\tilde{E}(\omega-\omega_{ba})d\omega \,.$$

The probability of transition is proportional to the modulus squared of this transition amplitude, and contains interference terms between the different pathways.

$$P_{a\to b} \propto \left| \int |\tilde{E}^{*}(\omega)|\,|\tilde{E}(\omega-\omega_{ba})|\,exp[i(\phi(\omega-\omega_{ba})-\phi(\omega))]d\omega \right|^{2} \quad (4.2)$$

This probability is maximized when the accumulated phase ($\phi(\omega_p) - \phi(\omega_S)$) of every two photon pathway for this transition ($\omega_p - \omega_S = \omega_{ba}$) is identical. The probability approaches zero if this phase varies rapidly and uniformly. Any phase function with periodicity Ω will produce maximum excitation of ω_{ab} = Ω. Any function without this periodicity will reduce the excitation probability. Experimental examples are explored in the next section.

Double-slit type of interference, as shown in Figure 4.2, is observed by replacing the integral in equation (4.2) with the sum, $E_1 E_2^* + E_3 E_4^*$.

4.3 Experimental Examples of Selective Excitation

This is a short section devoted to experimental realization of selective excitation. Key publications are identified, but for the sake of brevity, much of the work is ignored. The goal is to give a sense of the field and the history behind the author's implementation.

The first experimental demonstration of phase based selective excitation of Raman modes was already described in the background section.[52] There, a silica substrate was etched through microlithography techniques to produce a surface with periodic thickness variations and placed at the Fourier plane of a pulse shaper. The periodic function was binary in nature, only producing phase changes of zero or pi. The intra-period sequence is a pseudo-random "M functions", a pre-selected random structure with small spatial correlation.[53] This spectral phase was used to selectively excite low-frequency vibrational modes of an α-pyradine crystal with a single femtosecond laser. The beam was split into a multi-beam configuration similar to Figure 2.2 using a degenerate probe, and the Fourier transform of the time domain CARS profile confirmed selective excitation.

Silberberg's group used a computer controlled SLM at the Fourier plane to perform single beam CARS spectroscopy and microscopy about a decade later.[32] The total CARS intensity, measured by placing a short pass filter in the laser path after the sample, was recorded as a function of the period of a sinusoidal phase mask. By Fourier transforming, spectra were

acquired. Crude chemical images were acquired with a fixed phase applied to the SLM. The demonstrated resolution was about 50 cm^{-1} with a Raman excitation bandwidth of less than 1000 cm^{-1}.

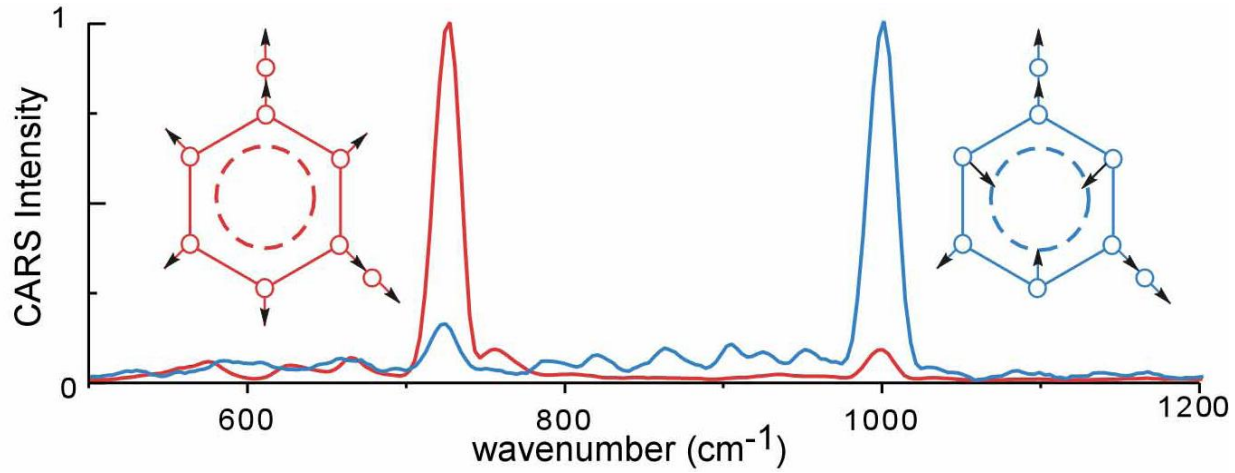

Figure 4.3. Normalized CARS spectra showing selective excitation of two vibrational modes of xylene. Psuedo-random binary phases were applied to the excitation pulse to select the mode.

The first paper on standoff detection with single beam CARS also demonstrated selective excitation.[42] There, psuedo-random binary phases, similar to those used by Weiner *et al.*, were applied with a computer controlled SLM. A narrowband probe was used, providing redundant resolution but allowing clear demonstration of the concept. This implementation was used to create Figure 4.3 in a standoff configuration. With the broad bandwidth available from our laser, we have demonstrated selective excitation up to the C-H stretches of poly-ethylene. Note that this ability is enabled in part by the ability to compensate for dispersion using the MIIPS technology.[48]

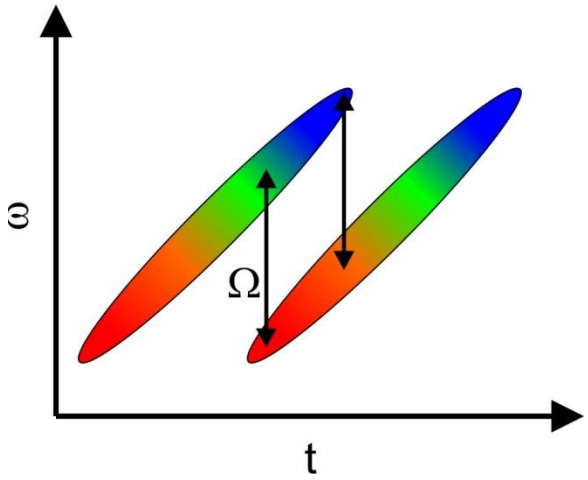

Figure 4.4. Schematic spectrogram of the spectral focusing method of selective excitation. The two frequencies are separated by the same amount at all times. The intensity beating produces a train of pulses at this difference frequency. The excitation frequency can be easily changed by adjusting the relative delay.

An alternative selective excitation scheme, which uses a large amount of chirp and delay stages instead of a pulse shaper, was also developed[54,55] and applied to standoff detection.[56] In short, two pulses are chirped and the relative delay is adjusted. This delay determines which frequencies overlap at any given time, as is shown schematically in Figure 4.4. Adjusting the relative delay will change which frequencies overlap, changing the excitation frequency for CARS experiments. Until recently, this technique was applied exclusively in multi-beam setups where the most important function was to allow rapid tuning of the excitation spectrum without changing the laser wavelength. A similar approach can be accomplished with a pulse shaper by creating a repeated quadratic feature (linear chirp) in the applied phase. This is, perhaps, the simplest selective excitation phase function.

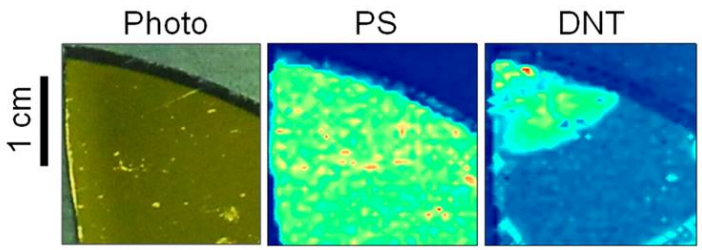

Figure 4.5. Standoff chemical images created at 1 meter using selective excitation. The two intensity maps were created with 2 separate scans with 0.5s of accumulation per pixel. The title refers to the selectively excited resonance: PS = 1200 cm^{-1}, DNT = 1350 cm^{-1}. Only the corner of the 5 µm film contains DNT (40% concentration). Figure reproduced with permission from reference 37.

This two chirp approach of selective single-beam CARS was used to chemically image DNT in polymer films in a standoff configuration in 2011,[37] and this data is reproduced in Figure 4.5. Although a spectrometer was used, the signal was integrated over a broad spectral range to create the image, and a spectrometer is not required. There is very good contrast within the complex chemical environment. Another group has performed single-beam CARS microscopy on the C-H stretches using a similar approach.[57]

4.4 Potential for Practical Application

In the experiments described in the previous section, there appears little practical motivation to use selective excitation. There is no increase in excitation when compared to using a transform limited pulse, and certainly a spectrum is better than knowledge of a single resonance. The only obvious advantage is that the spectrometer can be eliminated from the experimental setup.

There are, however, some subtle but significant advantages to the selective approach to single-beam CARS standoff detection. First, the reduced peak intensity of the shaped pulse can increase the damage threshold of the sample, allowing the pulse energy to be increased and producing a stronger signal. This is only a minor advantage since pulse energy is the most important factor in ultrafast ablation processes. Second, a high resolution probe beam is no longer necessary. This means a broader spectral range can be used, increasing the power in the probe. This will linearly increase the signal. In fact, the probe can be done away with entirely, and the broad band pump/Stokes will automatically serve as the probe, as was done in the single beam microscopy of Silberberg.[32] Unfortunately, elimination of the narrowband probe ensures total overlap of pump/Stokes and probe and maximum non-resonant contribution.

The possibility remains for improved signal. The next section explores one method developed by the author. This exploration will also clarify the subtleties of selective excitation. The SRS approach in the final chapter is perhaps the best way to realize the benefits of selective excitation.

4.5 Multi-Chirp CARS

The method described here increases the CARS signal by increasing the bandwidth of the probe, but maintains resolution through selective excitation. In this case, the excitation pulse is a long train of pulses in the time domain, while the broad bandwidth probe is short. By time delaying the probe beyond the duration of the excitation pulse, the non-resonant background can be

eliminated. These results will also clarify many aspects of selective excitation. The signal is collected with a single large area photodiode, which relaxes the strict alignment requirements for spectrometers, and allows easy implementation of fast laser scanning, as opposed to sample translation, to create images. This, in combination with the strong signal, enables single-shot per pixel imaging which is presented at the end of this section. These results are unpublished.

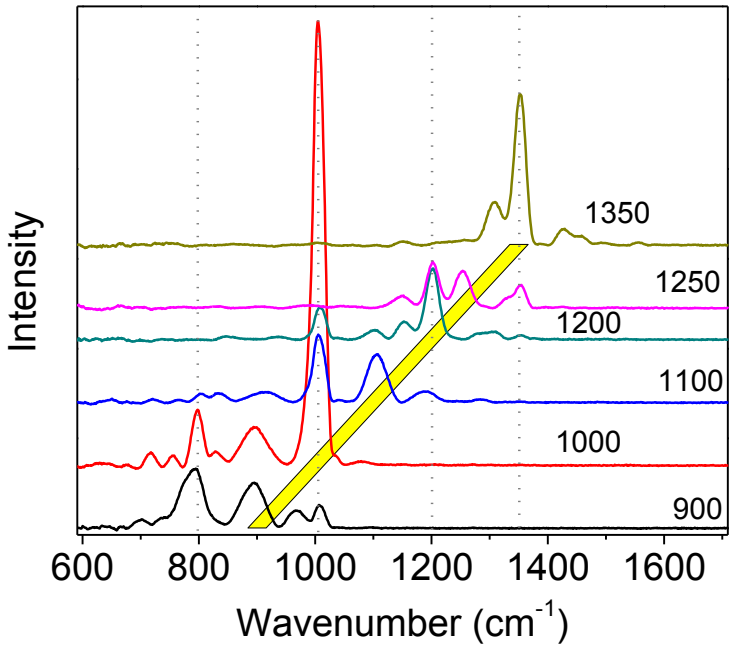

Figure 4.6. Standoff CARS spectra of thin films on mirror substrates observed during selective excitation. The spectra are offset to improve visibility and each spectrum corresponds to a different phase. The diagonal yellow line marks the target frequency of the selective excitation phase. The vertical dotted lines show the positions of the four material resonances.

Figure 4.6 was produced with the selective excitation and narrowband probe configuration used in Figure 4.5, and illustrates the inherent difficulties of selective excitation. In the DNT/PS film there are four resonances within the spectral range explored, identified with dotted lines. Notice that a peak always appears at the selective excitation frequency, regardless of the presence of a

molecular resonance. This is the non-resonant background. There is an increase in the magnitude of this peak on resonance, but clearly this method can only provide contrast and not detection. The problem is exacerbated by collecting the integrated signal as one would prefer with selective excitation. Doing away with the probe and using the excitation pulse as a probe, as was done in single-beam CARS microscopy, increases the non-resonant problem due to the total overlap of all fields.

The non-resonant problem can be solved, and the signal increased, by changing the nature of the probe. The probe can be made a short, intense pulse while the excitation pulse is long and provides chemical specificity. Delaying the probe beyond the duration of the excitation pulse will reduce or eliminate the non-resonant background. This approach was used in a multi-beam spectral focusing scheme to detect sodium dipicolinate (NaDPA), which is similar to a marker for bacterial spores.[56] Described here is a single-beam approach using a pulse shaper to perform selective excitation and delay the probe.

4.5.1 Principle

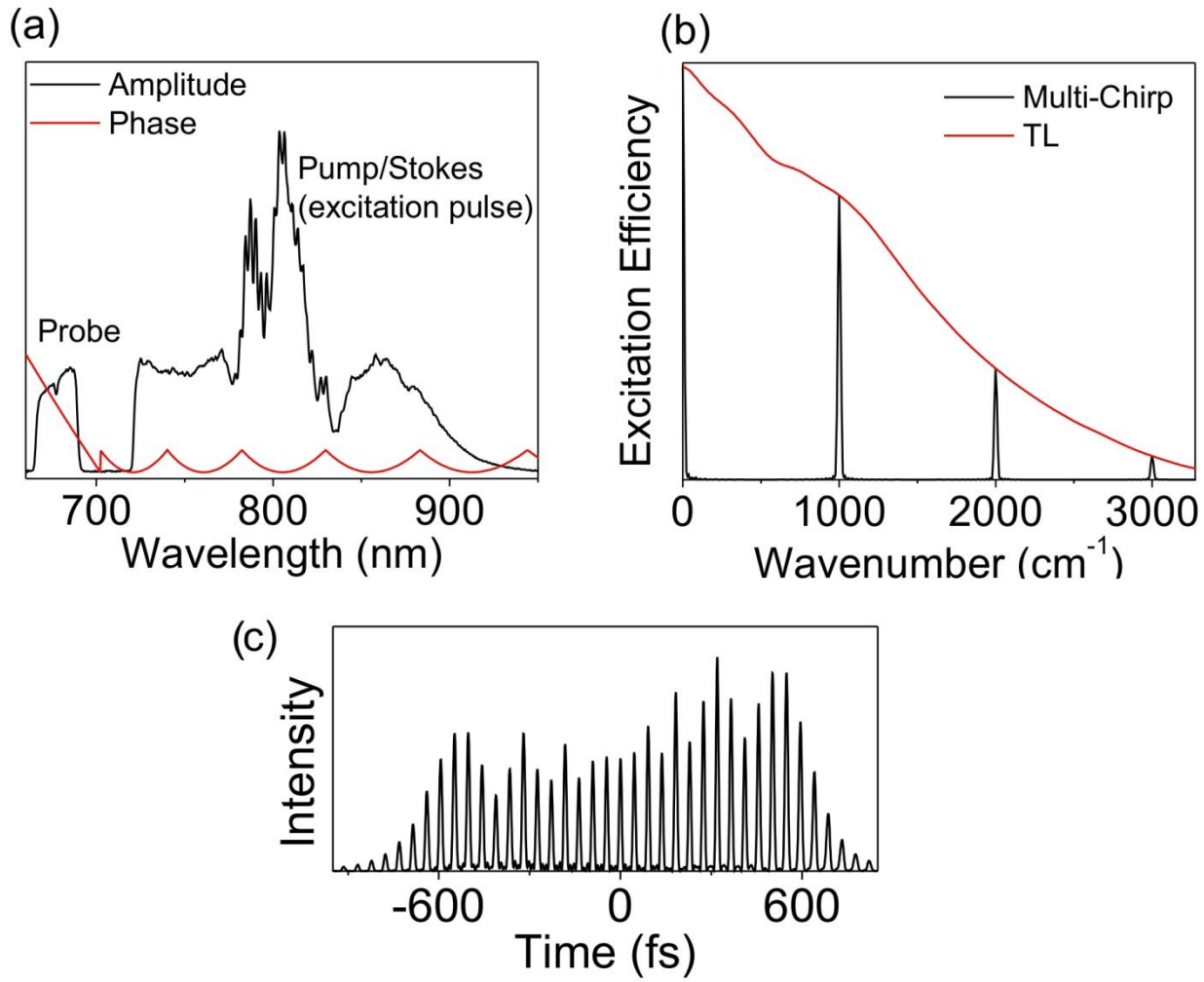

Figure 4.7. Multi-chirp selective excitation method. (a) Phase and amplitude of the spectrum, designed to excite at 1000 cm^{-1}. (b) Simulated excitation efficiency. (c) Time domain intensity profile. The phase is a periodic chirp function, except a small unchirped portion which is delayed in time and serves as a probe. A gap in the spectrum between the excitation and probe portions of the spectrum was created with amplitude shaping to prevent non-resonant contributions from the excitation pulse alone from overlapping with signal from the probe.

The laser spectrum and applied phase are shown in Figure 4.7a. Approximately 30 nm of the short wavelength side of the supercontinuum spectrum is reserved for the probe, supporting a ~35 fs transform limited pulse. A linear phase is applied to this section, the slope of which changes the time delay, but not the pulse duration (see Appendix C). The rest of the spectrum

receives the selective excitation phase. This phase consists of a series of parabolas, with respect to the optical frequency, separated by the Raman frequency of interest. The time domain profile of the excitation pulse consists of a long train of short pulses, simulated in Figure 4.7c. The excitation efficiency was calculated as the normalized square of the Fourier transform of the Intensity vs time profile and plotted in Figure 4.7b. Notice the excitation efficiency of the shaped pulse matches that of a TL pulse at the particular resonance 1000 cm^{-1}. The harmonics of this frequency are also excited with maximum efficiency.

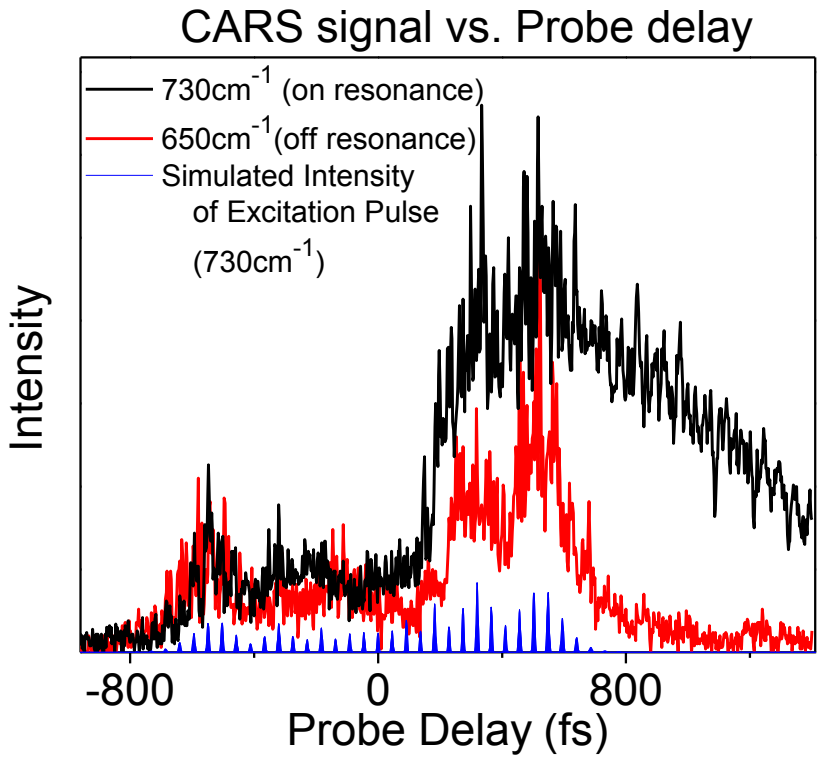

Figure 4.8. CARS signal from PTFE as a function of probe delay plotted for on- and off-resonance selective excitation. The square of the simulated intensity of the excitation pulse is also included.

Figure 4.8 shows the CARS signal as a function of probe time delay from a poly-tetrafluoroethylene (PTFE) or "Teflon" sample. The signal was collected from the diffusely reflecting surface in a standoff configuration with a lens, short pass filter, and photodiode. The time domain profile of the excitation pulse is also plotted. With the excitation pulse tuned off resonance, the CARS signal for a given probe delay essentially follows the square of the intensity of the excitation pulse. This is the non-resonant CARS signal. Tuning the excitation on resonance, 730 cm^{-1} for PTFE, the CARS signal outlasts the excitation pulse and is purely resonant. The probe is too broad in time to resolve the fine features of the excitation. This is done intentionally to prevent the probe from exciting the resonance.

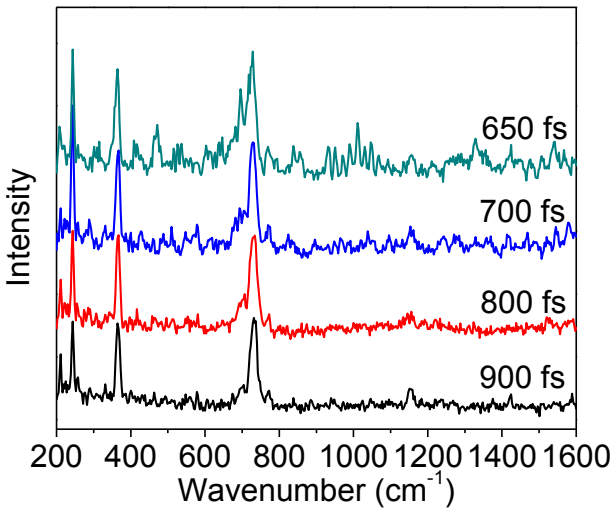

Figure 4.9. Spectra aquired by scanning the excitation mask for a fixed probe delays. Artifacts are observed in the spectrum at short delays due to non-resonant signal. The small peak at 1150 cm^{-1} is the sub-harmonic of N_2 in the air.

A spectrum can be created by scanning the selective excitation phase and recording the total CARS signal. The CARS spectrum of PTFE, acquired at various probe time delays, is displayed

in Figure 4.9. The cleanest spectrum is obtained at large probe delays. There is only one noteworthy resonance in PTFE (730 cm^{-1}) and the lower wavenumber peaks are sub-harmonics due to harmonic excitation from the shaped pulse (see figure 4.7b). The probe bandwidth, and spectral bandwidth chosen for detection can be designed to provide one clean octave of detection, from 600 to 1200 cm^{-1} for example. The frequency resolution is ~25 cm^{-1}.

It is useful to point out the advantages of this setup compared to the closest counterpart in the literature, the spectral focusing with delayed probe setup of Pestov et al.[56] Our method is single beam, with no moving parts or beam combining. The computer controlled pulse shaper creates the train of excitation pulses and time delayed probe. Maximum excitation efficiency is achieved by creating multiple phase parabolas as opposed to only two with the spectral focusing scheme. Further, spectral focusing schemes rely on linear dispersion introduced by materials to produce the quadratic phase. Real materials have higher order dispersion which will create a mismatch in the chirp produced at wavelengths separated by high frequencies, reducing the excitation efficiency. Pulse shaping methods can precisely control the relative phase of all wavelengths.

4.5.2 Experiment and Results

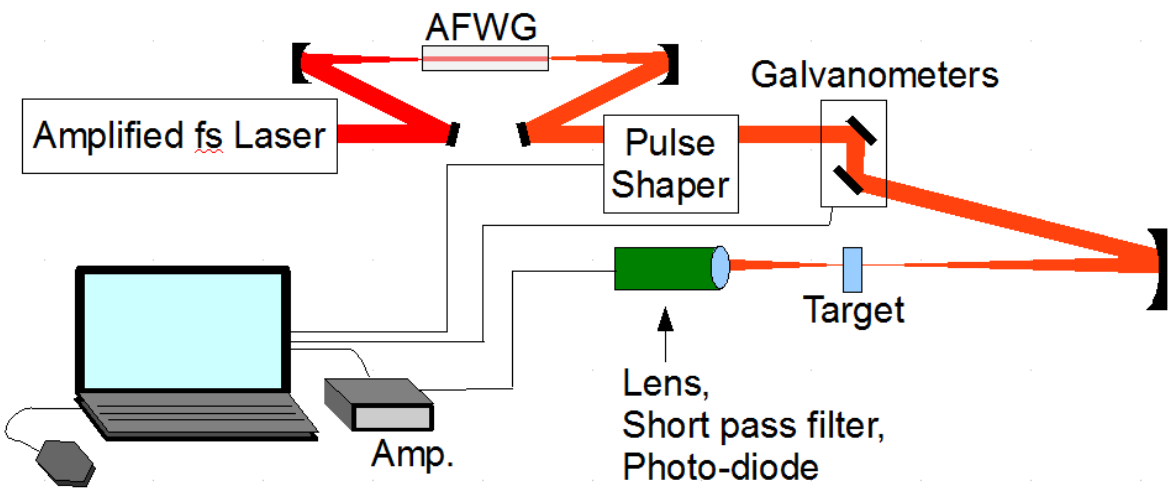

Figure 4.10. Experimental Setup. An amplified fs laser is spectrally broadened in an argon filled wave guide. This continuum is sent to a pulse shaper which compensates for any dispersion and implements the selective excitation phase and any amplitude shaping. The laser is focused at the target and the signal is collected. The imaged area is scanned at maximum rate using the galvanometer mounted mirrors. For scattering samples (PTFE) the detector is placed near the focusing mirror (retro-reflected signal).

This idea was used to perform fast, chemical imaging of macroscopic systems. A schematic of the setup is displayed in Figure 4.10. In contrast to the previous chemical images presented for standoff detection, which were produced by sample translation, the beam is steered by fast scanning galvanometer mounted mirrors. This enables single-shot per pixel imaging, with speed limited by the repetition rate of the laser.

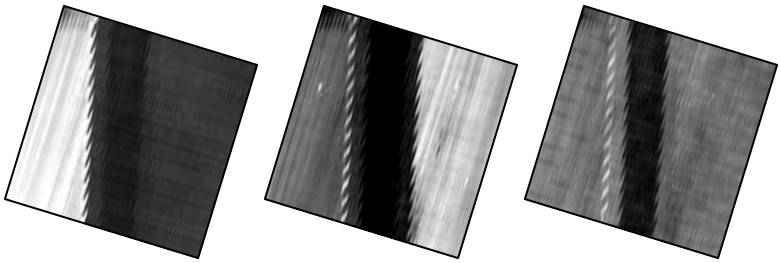

Xylene Toluene Off-Resonance

Figure 4.11. Single-shot-per-pixel images of side by side cuvettes, aquired with different selective excitation phases. The square, raster-scanned area is at an angle to vertical. Left is xylene, right is toluene. Different resonances are selectively excited (735 cm^{-1}, 1005 cm^{-1}, 760 cm^{-1} from left to right). 760 cm^{-1} is off resonance for both samples.

Figure 4.11 shows single shot per pixel chemical images of side by side cuvettes of solvent. Xylene and toluene can be identified in a single shot by applying the appropriate spectral phase. With off resonant excitation (760 cm^{-1}), the contrast disappears. The 100x100 pixel image required 10 s on the 1 kHz laser system.

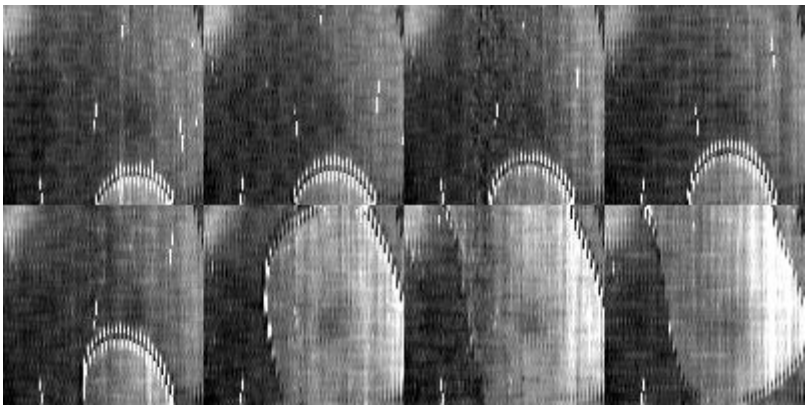

Figure 4.12. Selective CARS images of a drop of xylene rising in glycol. The phase of the excitation pulse is tuned to the 730 cm^{-1} mode of xylene. The images were acquired at the maximum rate: 1 pulse/ pixel.

To demonstrate the speed of the system, flowing liquids were imaged. In Figure 4.12, a drop of xylene slowly rises in a cuvette filled with glycol. The fluids are immiscible, and the high viscosity of glycol allows us to image the motion with the low repetition rate laser. While the images are rudimentary, and the motion capture is slow compared to the near video rate of human cognition, the process is scalable with higher repetition-rate lasers.

The next chapter will use the selective excitation ideas developed here to perform high speed standoff imaging with much greater sensitivity and no background.

5. Stimulated Raman Standoff Detection

This chapter describes, arguably, the most powerful Raman based standoff detection method developed thus far. This technique was developed in response to an obvious criticism of the standoff detection results in Chapter 3: the targets were mirror like surfaces. These previous results showed coherent Raman can in principle detect $\mu g/cm^2$ quantities of explosive simulants in a short time. However, considering a diffusely reflecting surface, a two inch optic at 10 meters will only collect about 10^{-6} of the reflected signal, requiring about 10^{12} times the collection time to achieve the same signal to noise as when the entire signal can be collected. Clearly, the signal must be dramatically increased in order to apply the technique to the textured surfaces of the real world, such as fabric and plastic. Here, the coherent property of the signal is exploited through heterodyne detection to amplify the signal by many orders of magnitude.

Stimulated Raman scattering is used for the first time to detect chemicals in a standoff configuration. This coherent Raman signal is intrinsically heterodyne amplified by the incident laser. This strong amplification can raise the signal far above the background noise level. Detection is equivalent to measuring small changes in the laser light diffusely reflected from the target surface.

Measuring the changes in intensity of the laser due to the coherent Raman process is not straight forward. The same difficulties experienced by those applying absorption based spectroscopies will apply here. The challenge is that variations in the substrate texture, color, and reflectivity as well as laser power fluctuations will also modify the reflected laser intensity. Thus far, this

problem has prevented application of SRS in standoff detection research. Fortunately, non-linear processes present interesting options to eliminate the effects of these linear processes from the measurement, and associated methods are developed in this chapter to enable the standoff detection technology.

This chapter will discuss the background of the stimulated Raman process, outline the experimental setup, and present standoff chemical images for evaluation of the efficacy of the technique. The results were just recently published, and the figures are reproduced with permission.[58]

5.1 Background

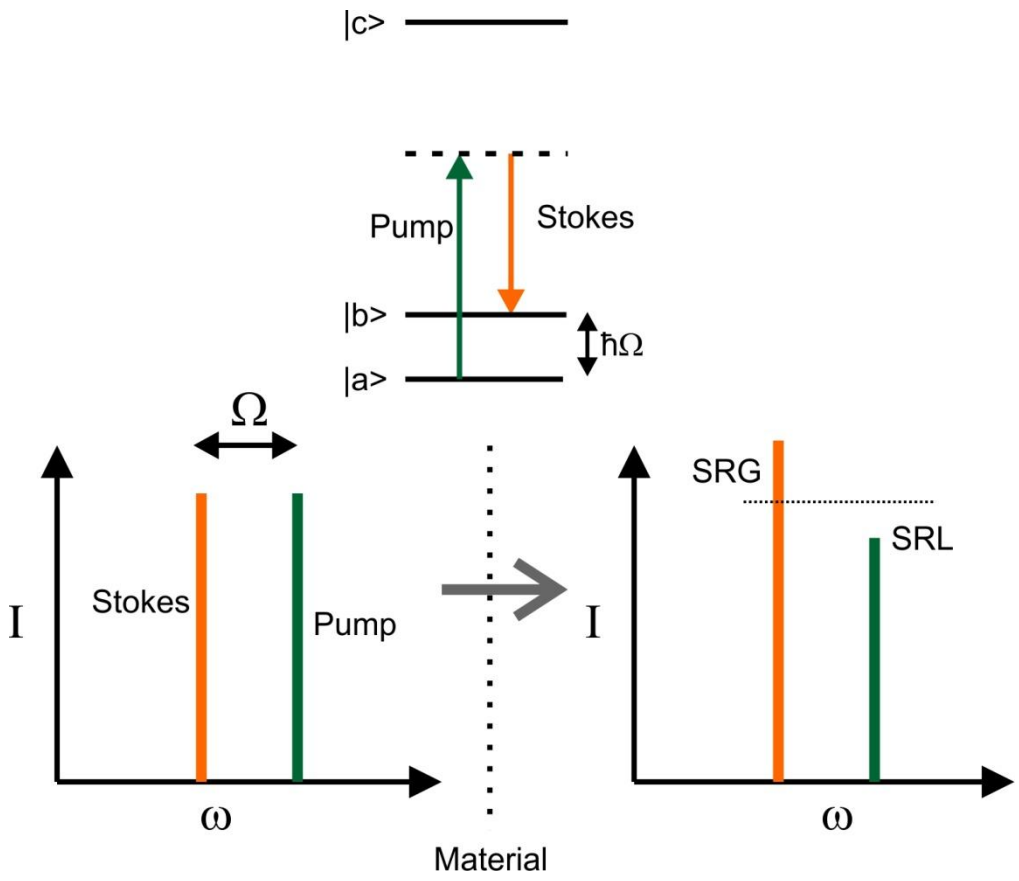

Figure 5.1. Schematic of the two-beam SRS process. If the frequency difference between the two lasers matches a material resonance, there can be a transfer of photons. Note the Stokes emission in the energy diagram is stimulated by the second field. The material is left in a new energy state, and the process cannot occur off-resonance.

When a ground state molecule is in the presence of two strong fields, there is a transfer of photons from the high frequency field to the low frequency field if their frequency difference matches a Raman transition within a molecule. This is called stimulated Raman scattering, in analogy to stimulated emission. Further pushing the analogy, spontaneous Raman scattering is a process stimulated by the ground state electromagnetic modes of the vacuum.[59] The scattered photons will have the same frequency, phase, and propagation as the stimulating field, and will therefore add coherently. The process can be measured by monitoring the changes in the laser

intensity at the two frequencies, termed stimulated Raman loss (SRL) and stimulated Raman gain (SRG) (see Figure 5.1). Conservation of energy is maintained by a change in the population of the excited vibrational state. In the weak response limit, the loss and gain are proportional to the number of molecules and the square of the total laser intensity. Note that the reverse process can occur if the molecule is in the excited vibrational state, but room temperature thermal energy corresponds to ~200 cm^{-1}.

Stimulated Raman scattering was discovered shortly after the invention of the laser, when a coherent beam was observed at an unexpected wavelength in a Q-switched ruby laser.[60] The new wavelength corresponded to a Stokes shift of the ruby laser from the nitrobenzene Q-switch cell. The new wavelength grew from spontaneous processes, and the propagation direction was determined by the properties of the "gain" region. Since then, the non-linear phenomenon has been utilized as a laser source at new wavelengths, for laser cooling,[61] and to measure ultrafast molecular dynamics.[62]

5.1.1 SRS microscopy

A few years ago, the phenomenon was used to for label-free chemical imaging in microscopy.[63] Using the same two beam laser configuration used for CARS, Sunny Xie's group developed an extremely sensitive SRS microscope,[64] eventually achieving video rate chemical imaging in vivo.[65] SRS can be described in the same framework as CARS and shown to have essentially the same sensitivity.[66] CARS creates light at new frequencies, and the sensitivity is limited by

signal photon number. SRS is detected by measuring the change in intensity of one laser frequency, and is limited by shot noise. One clear advantage of SRS is that there is no non-resonant background; the process requires a change in the population of a vibrational state. This benefit has shifted the focus of the microscopy community toward SRS.

The enabling technology in Xie's SRS microscope is high speed modulation and lock-in detection. This was also implemented previously for spectroscopic measurements.[67] The amplitude of one laser is modulated at high frequency. This modulation is imprinted on the other laser through the SRS process and detected through lock-in amplification. The sample is raster scanned to create the image, so the modulation must be done at faster rate than the raster scanning to avoid sample irregularities from contributing to the detected amplitude modulations. In addition, high frequency modulation (>1MHz) is required to eliminate the 1/f laser intensity noise and approach shot noise limited detection.[68]

5.1.2 Theoretical Comparison to CARS

Depending on the theoretical framework used, CARS and SRS can be considered the same phenomenon. This is most directly illustrated with the classical model developed in section 2.2. The model also provides the scaling properties of SRS. The two beam approach will be used in this illustration, and the analysis is based on that of Ozeki *et. al.*[66,69]

As described previously, the beat frequency of the two lasers will drive the oscillations in the polarizability of the material. This creates a phase grating which will imprint side-bands on any

additional beam. The previous analysis used either a separate probe or the pump beam as a probe, producing a blue shifted CARS spectrum. Of course, the Stokes beam will also act as a probe, producing a CARS signal at the same frequency as the pump. Simultaneously, the pump beam will produce a CSRS signal at the same frequency as the Stokes beam. These fields may interfere, producing gain or loss in the incident laser.

On resonance, there is a 90 degree phase lag in the response of the medium and the phase modulation varies as a sine function. Non-resonant contributions will respond in phase and vary approximately as a cosine function. In the frequency domain, the side bands will be real on-resonance and imaginary off-resonance (see section 2.2 for further information).

$$FT[1-c_1(i\ sin(\Omega t))] \propto c_1(\delta(\omega+\Omega)-\delta(\omega-\Omega))+\delta(\omega),$$

and

$$FT[1-c_1(i\ cos(\Omega t))] \propto -ic_1(\delta(\omega-\Omega)+\delta(\omega+\Omega))+\delta(\omega).$$

Where, c_1 is a constant. Again, the resulting spectrum is the convolution of the phase modulation spectrum and the input spectrum. The result is shown schematically in Figure 5.2.

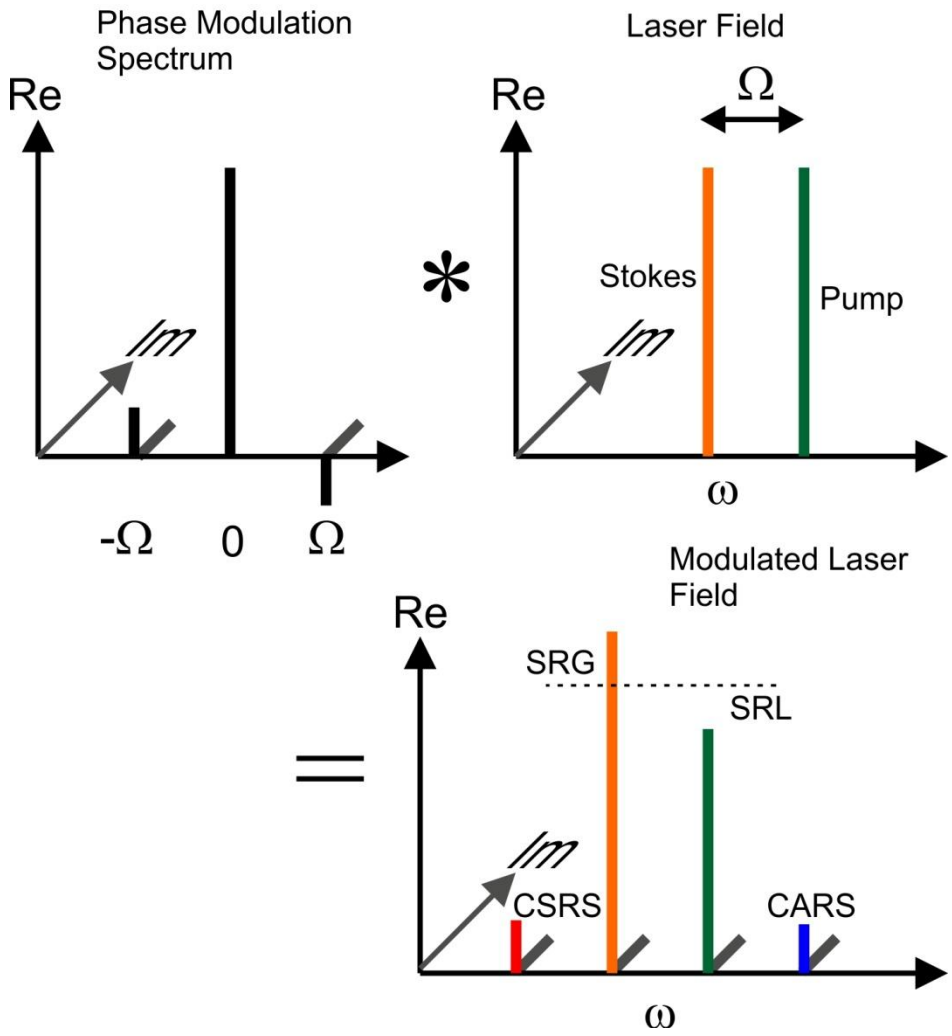

Figure 5.2. Schematic of the phase modulation of the input laser in the frequency domain. The real and imaginary parts are shown.

On-resonance these signals will interfere with the incident laser producing gain at the Stokes wavelength and loss at the pump wavelength. Off resonance, the phase relationship is such that the non-resonant CARS and CSRS will add in quadrature with the excitation field, leaving the pump and Stokes intensities virtually unaffected for small signals.

The scaling properties of the SRS signal can be inferred from the properties of CARS and CSRS signals (see section 2.2). Consider the CSRS field from the pump beam which will occur at the frequency of the Stokes beam, ω_S, and be proportional to the interaction length, *l*.

$$E_{CSRS(\omega_S)} \propto i\omega_S l\chi E_p E_S^* E_p.$$

The appearance of $i\omega$ is due to the produced field being related to the derivative of the polarization.[27] The intensity of the Stokes beam after the sample will include the heterodyne detected CSRS signal.

$$I(\omega_S) \propto |E_S + E_{CSRS}|^2 \propto I_S + I_{CSRS} + 2Re(E_S E_{CSRS}^*).$$

Ignoring the small middle term, the final term is interpreted as the signal and

$$I_{SRS} \propto 2Re\left(-E_S i\omega_S l\chi_R E_p E_S^* E_p\right).$$

The susceptibility is negative imaginary on resonance and I_{SRS} is positive. The SRS signal is quadratic in laser intensity and linear in molecule number. This term vanishes if the susceptibility is real, thus there is no non-resonant contribution.

5.2 SRS Standoff Approach

As with CARS standoff detection, the high repetition rate lasers of today do not produce the pulse energies required to provide sufficient intensity, when focused at a distance (low NA), to induce appreciable SRS. Again, low repetition amplified sources are required. This presents a serious challenge since the high speed modulation, which enables high-sensitivity SRS microscopy, cannot be implemented. Further, in order to interrogate a large area, a single shot approach is desirable. This is very challenging due to the differential nature of the SRS measurement.

The solution is relatively simple. Include a time delayed collinear reference pulse and collect the signal in the time domain with a fast photodiode. This will account for any optical properties (absorptivity, reflectivity) of the target which could otherwise manifest as SRL or SRG. In principle, this will also prevent laser noise from contributing to the signal.

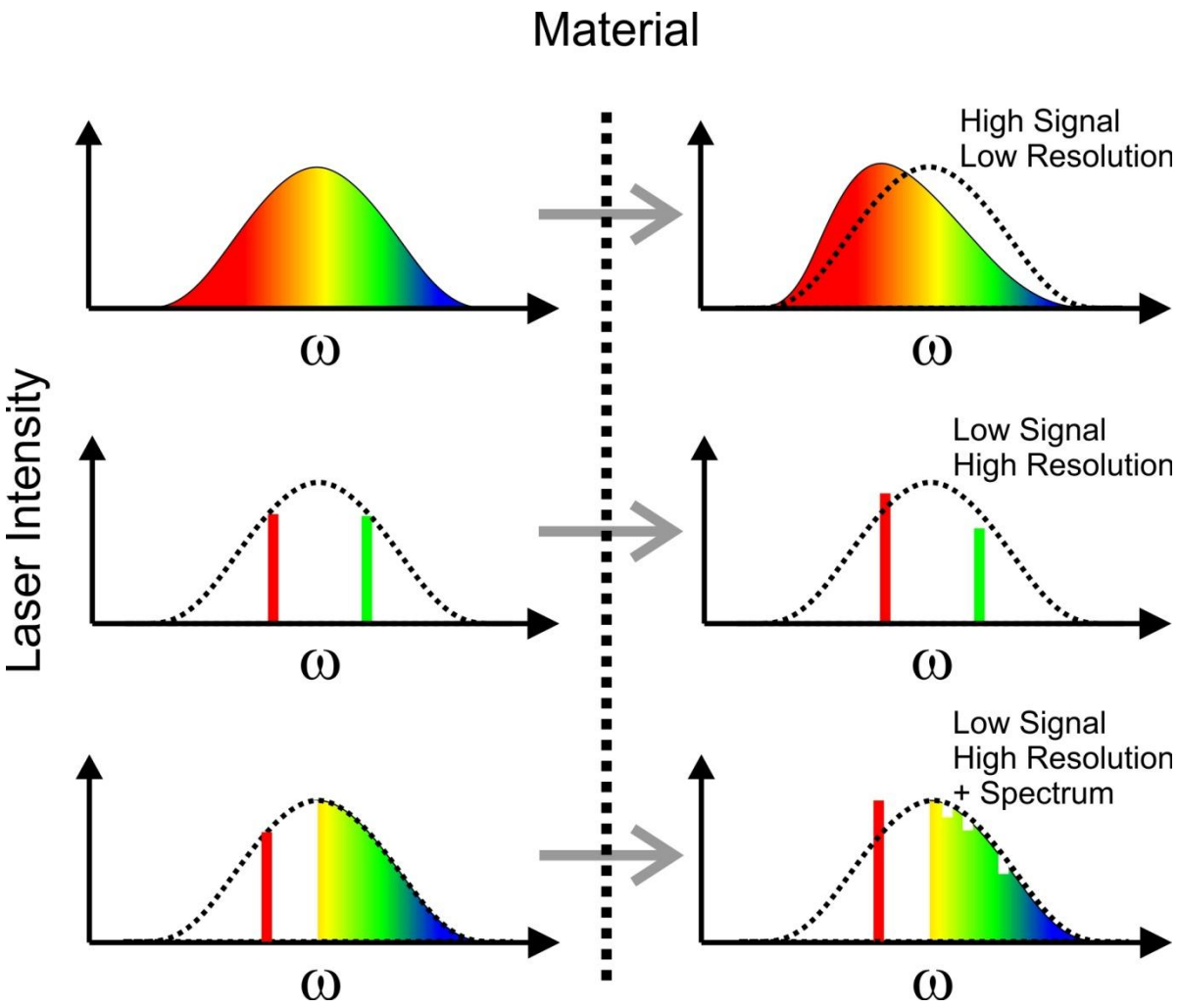

Figure 5.3. Schematic of various approaches to broadband SRS. The narrow-band/broadband approach (bottom) used in single-beam CARS does not produce more energy resolved signal than simply filtering the spectrum into two spectral bands.

The second challenge is to develop a single beam method. This will provide a simple and stable setup with automatic synchronization and spatial overlap of all fields. This precipitates several subtle problems. As with CARS, simply filtering a broadband laser spectrum into two narrowband features reduces the energy, and the SRS signal is proportional to the energy squared. Retaining a broadband portion and a narrow band portion, as was done with single-beam CARS, does not solve this problem (see Figure 5.3); a spectrum will be created, but for

each resonance there are only two narrow spectral regions contributing to the signal intensity. Note that this approach has been very successful in time resolved studies of molecular dynamics.[62,70] The unfiltered broadband spectrum will produce the maximum amount of SRS, but without the ability to energy resolve the process.

The solution is to use coherent control of the non-linear process. The appropriate spectral phase will suppress excitation of most Raman modes, but produce maximum excitation efficiency of the desired resonance (see Chapter 4). With the phase tuned to a specific molecular vibration, SRL and SRG will only be observed in the presence of the corresponding compounds. The following experimental section will provide the details of the implementation.

5.2.1 Experimental Setup

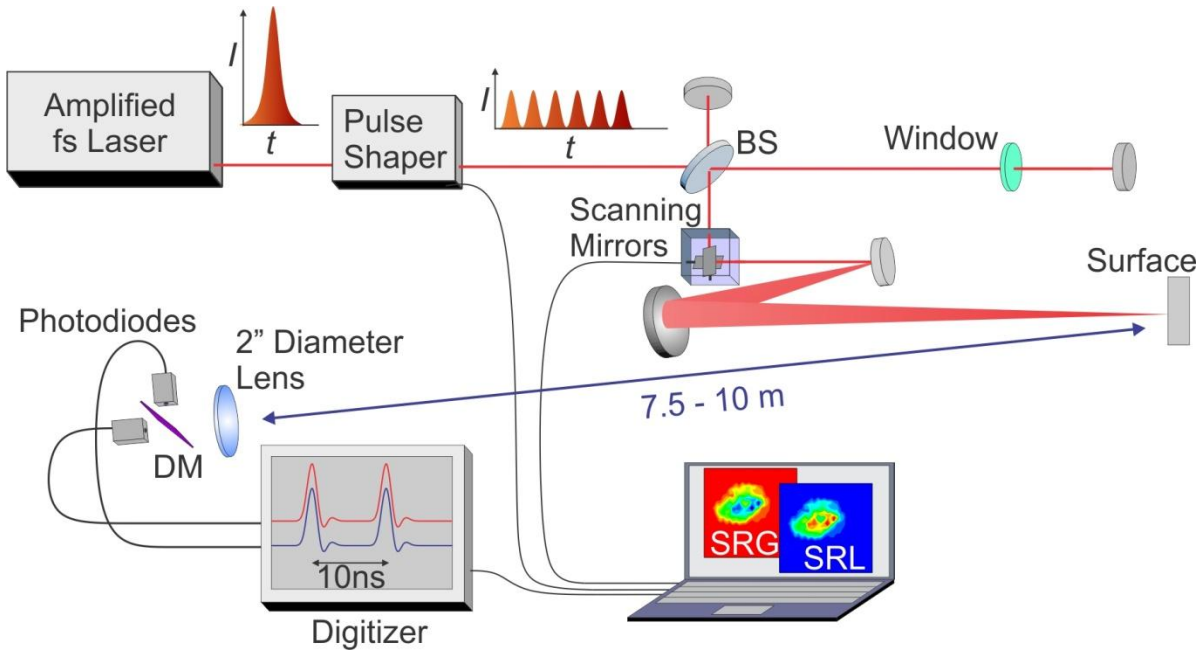

Figure 5.4. Experimental Setup. The spectral phase of a broadband femtosecond laser is modified with a pulse shaper. A Michelson interferometer creates two collinear pulses. The window adds dispersion to the second pulse. The beam is steered by the fast scanning mirrors and expanded and focused at one meter on the sample surface. A lens collects the diffusely reflected light at a distance of 7.5-10 m. The signal is split between two fast photodiodes using a dichroic mirror and digitized with an oscilloscope. Software compares the intensity of the two pulses and the normalized difference is recorded. Scanning the pulse shape produces a spectrum, scanning the mirrors creates an image.

Figure 5.4 shows a schematic of the experiment. The laser system and spectral broadening is identical to that used in the CARS experiments, but the separate probe arm of the pulse shaper is not used. The pulse shaper modifies the pulse shape, through spectral phase shaping, to excite a particular Raman mode. A colinear, time-delayed pulse, identical in energy and spectrum but not spectral phase, is created with a Michelson interferometer and the two pulses are focused on the sample. The second pulse serves as the reference. The glass window in one arm of the interferometer introduces additional dispersion which shifts the resonant frequency of the reference pulse (see section 5.2.2). The two pulses are separated by ~10 ns.

If a particular compound is on the surface, there will be a transfer of photons between the two halves of the spectrum of the first pulse but not necessarily the second due to the different phase of the second pulse. The diffusely reflected laser scatter is collected, and any change in the intensity of either spectral half is inferred by comparing the two pulses. This is done by sending each half of the laser spectrum to a fast photodiode (1GHz, amplified), and recording the intensity of the electronic signal in the time domain using an oscilloscope (Lecroy, Waverunner 610zi). Homebuilt software synchronizes the components and calculates the signal. Fast-scanning, galvanometer-mounted mirrors enable raster scanning of the target to create an image. Scanning the phase applied to the pulse shaper will produce a spectrum. Details of the phase scanning and imaging program are available in Appendix C.2.

5.2.2 Selective Excitation

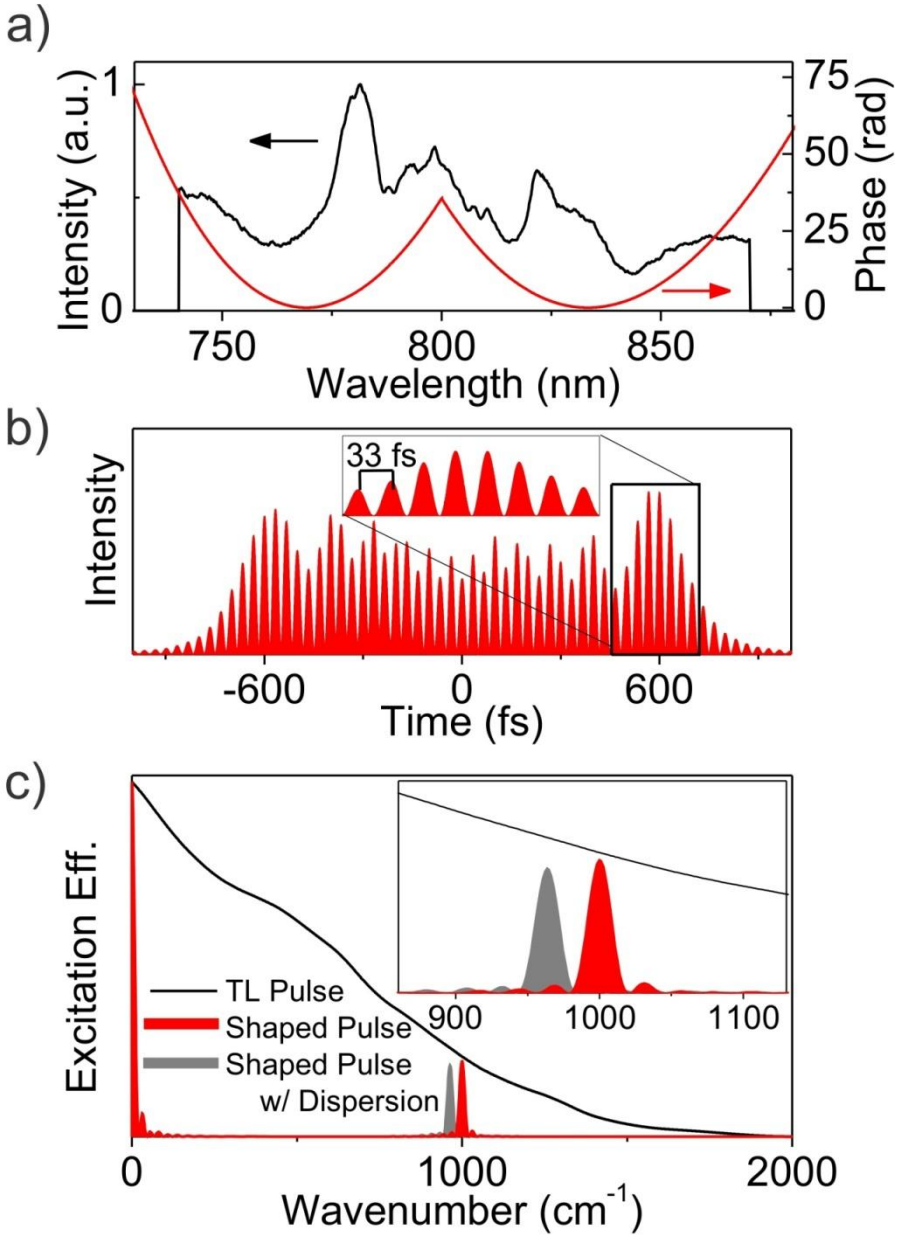

Figure 5.5. Selective Raman excitation. (a) Experimental laser spectrum and phase. (b) Simulated time domain intensity profile. (c) Calculated excitation efficiency. The selective excitation phase is designed for a 1000 cm^{-1} Raman transition and the supercontinuum laser spectrum is cut to cover 2000 cm^{-1} shift, which is optimal in this example.22 The resultant time domain intensity profile consists of a long pulse train with a period of 33.3 fs. The SRS excitation spectrum (c) has a resolution of ~25 cm^{-1}, yet equivalent excitation efficiency as a TL

pulse. The peak of excitation shifts by ~40 cm^{-1} with the application of 300 fs^2 of group delay dispersion.

The selective excitation spectral phase used in these experiments resembles the resultant phase used in spectral focusing experiments, and the previous standoff CARS images. Two parabolic spectral phase functions (linear chirp) separated by the Raman frequency of interest will create a train of pulses arriving with the corresponding period. The greater the magnitude of the quadratic phase, the longer the pulse train and narrower the resulting excitation peak. Figure 5.5 presents spectrum, phase, simulated time domain intensity profile, and simulated excitation efficiency using typical parameters of the experiment. The energy resolution of the selective excitation is approximately 25 cm^{-1}, or about 1% of the bandwidth.

An interesting property of this spectral phase, discovered in this project, is that the application of linear chirp will shift the peak of excitation, as simulated in Figure 5.5c. This can be expected since linear chirp is equivalent to a parabolic phase functions centered with the spectrum (ignoring linear terms which will not affect non-linear processes). Adding this spectral phase to the selective excitation phase will shift the center of the two parabolas toward or away from the center of the spectrum, shifting the excitation up or down in energy. There will also be a small change in the spectral width of the excitation. Linear chirp, or 2nd order dispersion, is the leading contribution of dispersion in most materials, and the function of the window in the reference arm of the experimental setup is to induce this shift. Additional discussion of the effect of dispersion is available in Appendix C.

5.3 Results: Spectra

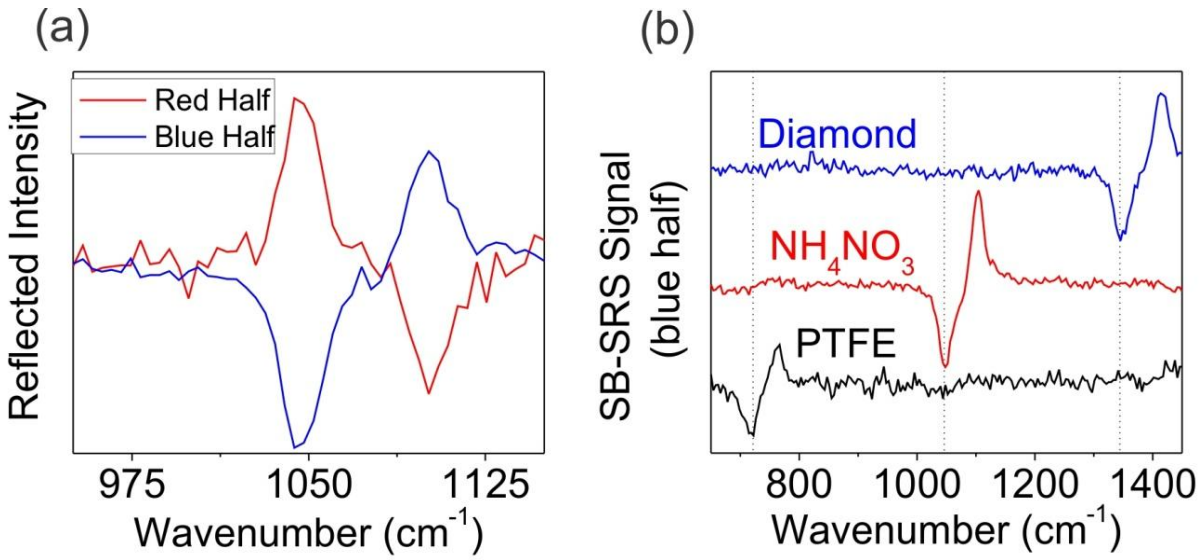

Figure 5.6. Experimental spectra acquired by scanning the phase on the SLM. In (a) we see the transfer of photons between the halves of the spectrum in the presence of NH_4NO_3, while (b) shows only the signal measured from the blue half for various materials. The signal changes sign as the reference pulse becomes resonant with the transition. There are 20 laser shots per phase in the spectra.

Reasonable signal to noise requires only a few laser pulses, and spectra can be acquired in a few seconds by scanning the pulse shape with the computer controlled spatial light modulator. In Figure 5.6a, we present a spectrum acquired from NH_4NO_3 obtained by scanning the applied phase using the computer controlled SLM in the pulse shaper. The x-axis is labeled by the resonance excited by the applied spectral phase. At the nitrate symmetric stretch at 1040 cm^{-1}, there is a transfer of photons from the bluer half of the laser spectrum to the red. The opposite effect appears to occur at higher frequencies, but is in fact indicative of the same process occurring in the reference pulse; its phase is the sum of the selective excitation and that due to the extra dispersion (see Figure 5.5c). The location of this reversal can be tuned by changing the

amount of dispersion in the arm of the interferometer. SRS Spectra from several materials are presented in Figure 5.6b. Each point is the average of 20 laser pulses.

The presence of the dip in the spectrum can complicate spectral analysis. By replacing the window (dispersion element) in the experimental setup with a short pass or long pass filter, this dip is eliminated. However, only SRG or SRL can be measured, and two-photon absorption may contribute to the signal. The SB-SRS technique was designed primarily for imaging and detection of a single resonance, and these results are the focus of the next section.

5.4 Results: Imaging

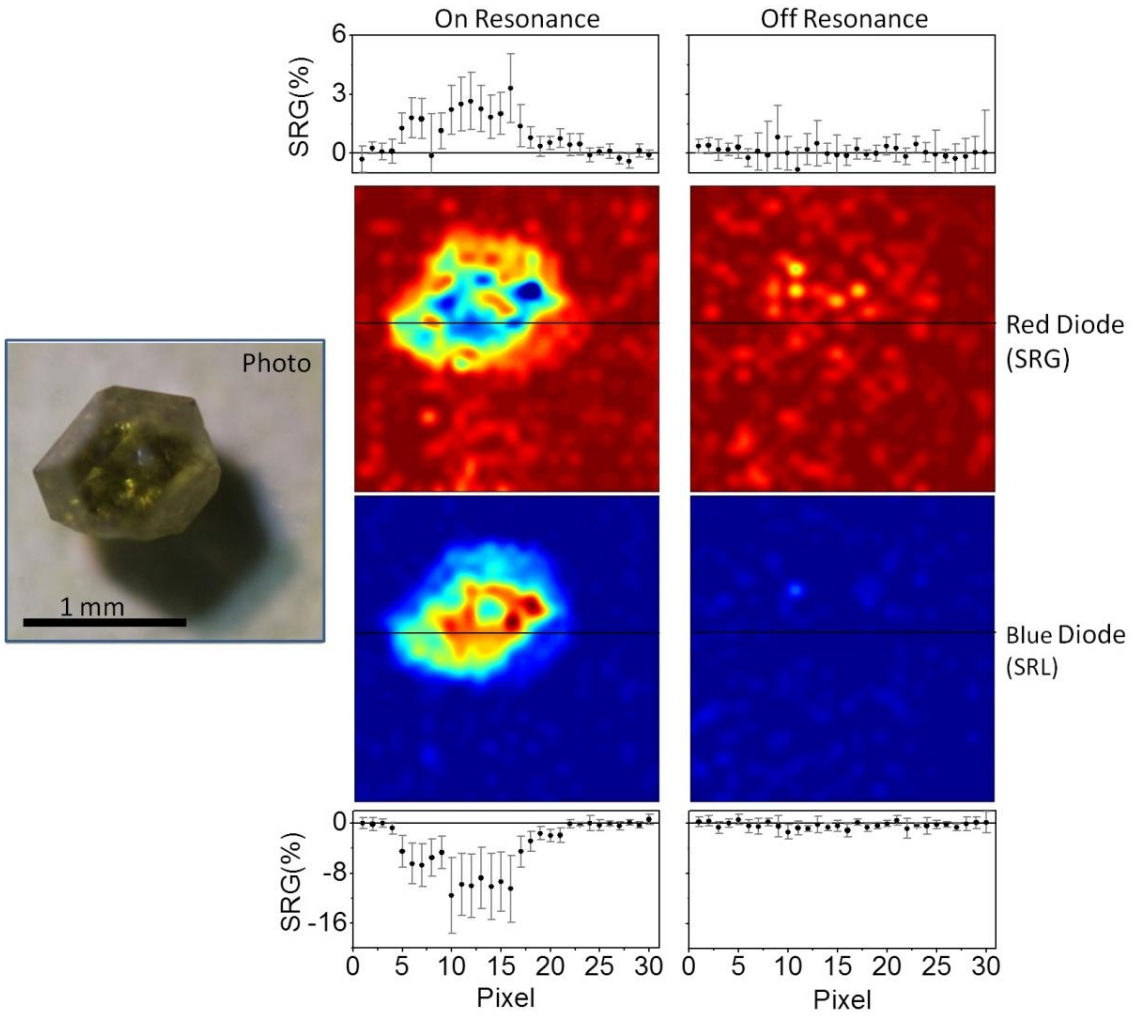

Figure 5.7. Chemical images of a diamond on adhesive paper acquired with 10 laser pulses per pixel. Both SRG (top row images) and SRL (bottom row images) are detected simultaneously. With the pulse shape tuned to 1360 cm^{-1} (on resonance), the diamond is clearly visible. Off resonance (1050 cm^{-1}), only noise is observed. The inserts show the data acquired along the black line in the images. The statistical analysis of the data includes error bars corresponding to 1 standard deviation of the mean, note this is a zero-background method.

The best application of the method is to quickly monitor the intensity of one or a few vibrational resonances for chemical imaging as in SRS microscopy.[64] Figure 5.7 shows such an image,

created by raster scanning a "post-it" note with a small diamond placed on the adhesive portion. With 10 laser shots per pixel, a satisfactory chemical image is created using SRG or SRL. With the phase tuned off resonance, only noise is visible. This shows that the method is only sensitive to chemical information, and bright field features only manifest as a change in noise magnitude. The images also have no background, as shown in the line scans, thus the technique can be used for detection in addition to image contrast.

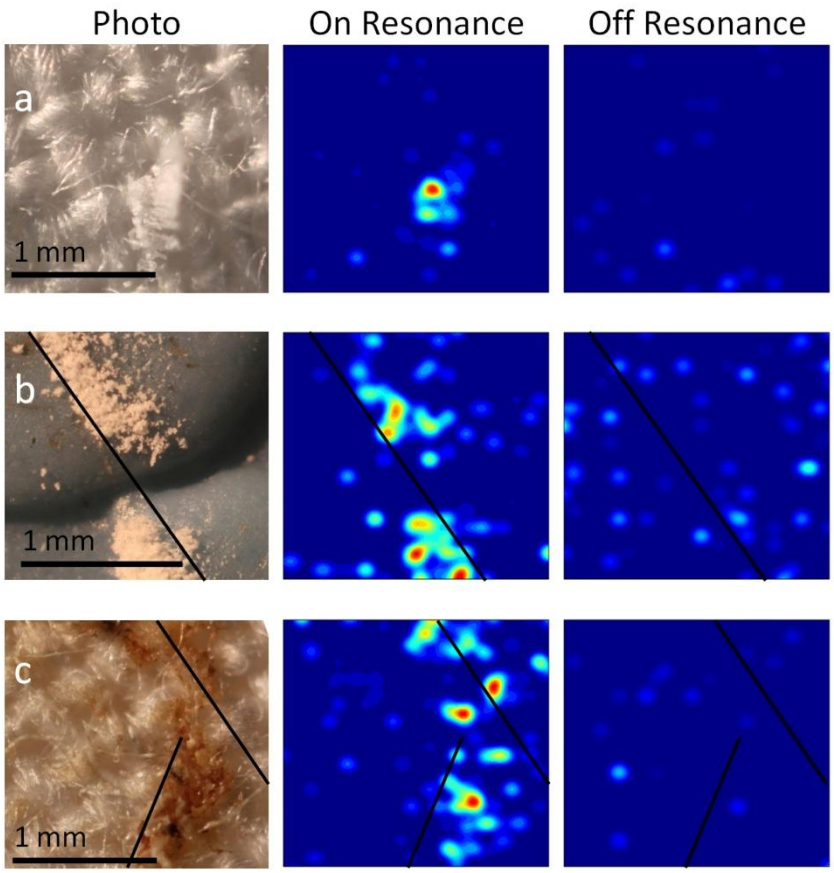

Figure 5.8. Standoff SRS images of NH_3NO_4 on cotton (a) and blue textured plastic (b) and TNT on cotton (c). The sample distribution on each substrate corresponds to ~ 100 µg/cm^2, although the local concentration is higher. With 20 laser shots per pixel in the 30x30 images, the distribution of the analyte is recorded by observing SRL. Statistics were used to eliminate points less than 0.8 standard deviations of the mean above zero. The black lines are guides to the eye. On (off) resonance is 1043 cm^{-1} (950 cm^{-1}) for NH_4NO_3 and 1360 cm^{-1} (1043 cm^{-1}) for TNT. Data for (a) and (c) was collected at 10m, (b) at 7.5m.

Figure 5.8 shows chemical images of plastic and cotton surfaces. In samples (a) and (b), 100 µg of dissolved ammonium nitrate (NH_4NO_3) was sprayed non-uniformly over a 1 cm^2 area. In (c), trinitrotoluene (TNT) was deposited in the same concentration by dry transfer. From the photos,

the samples consist of collections of micro-particles or thin residues. Zero background chemical images are obtained from these surfaces with 20 laser shots per pixel.

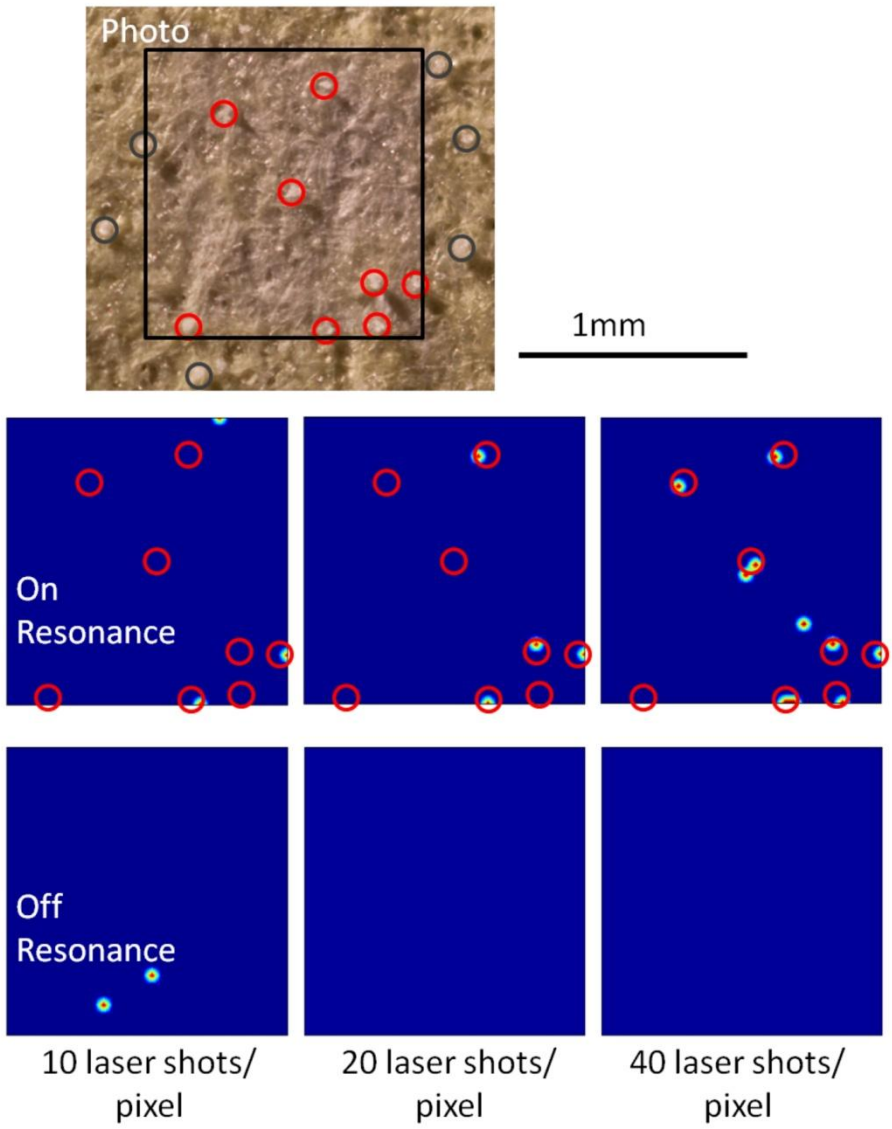

Figure 5.9. Detection of single micro-particles of NH_4NO_3 deposited on an adhesive paper. In the photo, circles identify the micro-particles deemed to be the largest (judged by the shadow cast upon side illumination). In the chemical images, points less than 1.5 standard deviations of the mean above zero are equated to zero, all other points given a value of one. This analysis allows an occasional false positive, but with 20 laser pulses half of the circled particles are identified. A sieve (75µm), was used to ensure small particle size. Image: 30 x 30 (0.9 s per single shot image on the 1kHz system). Signal collected at 10 m.

It is challenging to uniformly deposit smaller quantities than those present in Figure 5.9. However, by careful observation of an adhesive paper substrate before and after deposition, one can identify single micro-particles of NH_4NO_3. Figure 5.9 shows that a majority of the largest particles are identified with just 20 laser shots. The zero level background and statistics obtained from multiple laser shots provide a useful method with which to claim "yes or no" detection. The circled particles' diameters are ~25 - 50 μm with calculated masses between ~15 and 100 ng. Imaging 15 ng particles in a 1.5 mm^2 area is equivalent to ~1 $\mu g/cm^2$.

5.5 Conclusions

In comparison to CARS, SRS offers several advantages. The absence of non-resonant background makes SRS an ideal "yes or no" detection technique. The process scales linearly with concentration, thus the signal from minority constituents is less likely to be overwhelmed by other materials. In terms of speed, the images presented here were acquired at a rate that is two orders of magnitude faster than those obtained in Chapter 3 with standoff CARS imaging and a similar setup.[37] Further, it is substantially less challenging and less expensive to image the rapidly scanned laser spot to a photodiode rather than a spectrometer slit. While SB-SRS can quickly alert someone of the presence of a particular vibrational resonance of interest, one drawback is that spectral information requires phase scanning.

The Silberberg group recently used the non-resonant background to amply the CARS signal and detect milligram quantities of explosives at 50 m from absorbing substrates using a six inch collection optic.[45] Here, 4-5 orders of magnitude less material is detected in 2-3 orders of magnitude less time using a 10th of the laser power and essentially the same solid angle of collection.

An interesting aspect of the technique is that the signal is measured by monitoring the diffusely reflected laser light, which is quite intense and easily collected with small optics at large distances. At less than 10 m, the signal was attenuated to prevent saturation of the photodiodes. This suggests that SB-SRS could be very useful for greater standoff distances, especially since the technique is robust against beam pointing instabilities due to the short delay of the reference. As with SRS microscopy, the fundamental sensitivity limit of the method is related to the photon number shot noise,[66] about 10^{-5} per pulse with a 2 inch lens at 10 meters. The noise level of our implementation is significantly above this level, and the technique is presently limited by the accumulated instrument noise (~0.5% rms). This noise value was determined by measuring the variation in signal level while the laser was stationary and a single phase was applied. During imaging, the full dynamic range of the digitizer cannot be used due to variations in absorption and detector coupling. This will generally increase the noise level.

We have introduced a standoff detection and imaging method which uses the non-linear process of stimulated Raman scattering. Coherent control of Raman transitions provides the chemical specificity for the single beam method, and time multiplexing enables single shot

implementation. With 10 mW of laser power in the near IR, we can detect a single ~15 ng particle of an explosive simulant within 20 ms on a number of "real-world" delicate substrates such as paper, clothing, and plastic. The speed, sensitivity, and robust performance on chemically complex substrates make this technique one of the most promising methods for standoff detection of trace quantities of explosives.

6. Outlook

Multiple techniques were developed in this dissertation to chemically image macroscopic targets using coherent Raman scattering. The research is considered applied physics, and there are very specific, practical goals in mind. However, reaching these goals requires a deep understanding of non-linear optical phenomena and the willingness to take a step back and apply some perspective. The research builds on many recent developments in microscopy and coherent control. Hopefully the ideas developed here will have a broad impact on the goals of fundamental and applied science.

On the goal of standoff detection of trace quantities of explosives, the project was very successful. In comparison to other Raman based standoff detection reports, the stimulated Raman approach is extremely sensitive, achieving $\mu g/cm^2$ detection at 10 meters on chemically complex substrates within 20 seconds. This is accomplished with an average power comparable to a laser pointer. Spontaneous Raman approaches using conventional wavelengths are ~ 2 or more orders of magnitude from this detection limit. In principle, UV enhancement can match this performance, but this assumes that 300 photons in 20 seconds provides adequate signal to noise for detection.[21] Demonstration on realistic substrates present sensitivities that are 2 orders of magnitude larger.[20] Note that the *quantity* of chemical detected in our experiments is many orders of magnitude smaller than spontaneous Raman reports as we can detect 50 ng with just 20 laser pulses. Most reports on linear detection methods will sample a large surface area, and therefore large amounts of material.

Non-linear techniques require a focused laser. In contrast, linear techniques generally employ a large collimated beam. This is often mistakenly perceived as a disadvantage for non-linear techniques, which will take longer to scan a large area. If, for example, there are two methods with the same sensitivity of 1 μg/cm^2, one with a small spot size (0.1 mm^2) and one with large (50 cm^2), a fingerprint with 1 μg/cm^2 concentration of a hazardous material on a door handle is below the detection level of the large area method and the small area method would have to scan to find it. One benefit of a small area method is that background signals will be orders of magnitude smaller. A report on microscopic measurement of explosive contaminated fingerprints found the resolution should match the average size of the particle to be detected (10μm in their case) to provide the best chemical descrimination.[71]

One admitted criticism of coherent Raman standoff detection systems is the immense cost and complexity. The single beam methods developed in the Dantus group eliminate the complexity, assuming large bandwidth laser systems can be made robust. Fortunately, femtosecond laser technology is developing very rapidly. Femtosecond fiber laser systems producing 1 μJ pulses at 1 MHz are being deployed widely for laser surgeries, where PhD physicists and chemists are not available for maintenance. Such a system could increase the speed of detection by up to 1000 times purely due to the repetition rate, with the only remaining requirement being a broad bandwidth. Based on advances in photonics over the past 10 years, it is fair to assume a compact and industrial type of laser with the desired characteristics might be available within 5 years to make this approach practical.

The SRS standoff technique is new, and improvements can be anticipated with further research. In addition, more general goals can be immediately pursued. For example, the SB-SRS can be explored for microscopy or combustion diagnostics. Regarding combustion, SRS is sensitive to populations, and may provide new opportunities for thermometry.

Another interesting feature of SB-SRS which could be explored is that both SRL and SRG can be measured simultaneously. This is unusual in that most microscopy approaches modulate intensity and only one of these processes can be measured at a time. By measuring both simultaneously, other non-linear processes which may change the intensity of a particular wavelength can be avoided.[72] For example, two-photon absorption will manifest as SRL in the usual setup. Avoidance of such interference could be demonstrated with SB-SRS.

APPENDICES

Appendix A - Flame Thermometry/Imaging

This chapter presents some interesting results on gas phase thermometry using the single beam CARS technique. This is a short discussion, as it is unrelated to standoff detection, and most of the motivation and history is neglected. It is essentially self-contained, and the uninterested reader can skip this section with little loss of fluidity. However, the technique explores the CARS signal in the time domain, and the data presented can help clarify the process. The main result is a temperature and chemical map of a flame.

A.1 Background

In gas phase measurements, all the benefits of CARS spectroscopy can be realized. The medium is not easily damaged by the laser, so high powers can be used. The experiment can be designed in a transmission style setup, and the coherent CARS beam is easily collected. The sample volume is large to compensate for the reduced material density. Further, the low dispersion of gasses allows simple phase matching criteria. With these benefits, there is a long history of using CARS to study combustion processes.[24]

For many years, CARS combustion studies were done with high power nanosecond or picosecond lasers. However, femtosecond lasers have some significant advantages, realized in the last decade.[73–77] Measurements performed on the femtosecond time scale occur faster than gas phase collisions, greatly simplifying the extraction of certain quantities, such as

temperature.[73] The broad bandwidth of femtosecond lasers is conducive to measurement of multiple spectral lines. The Dantus group has developed single-beam CARS for combustion measurements, greatly simplifying the experimental setup.[78]

A.2 Hot-band Temperature Measurement

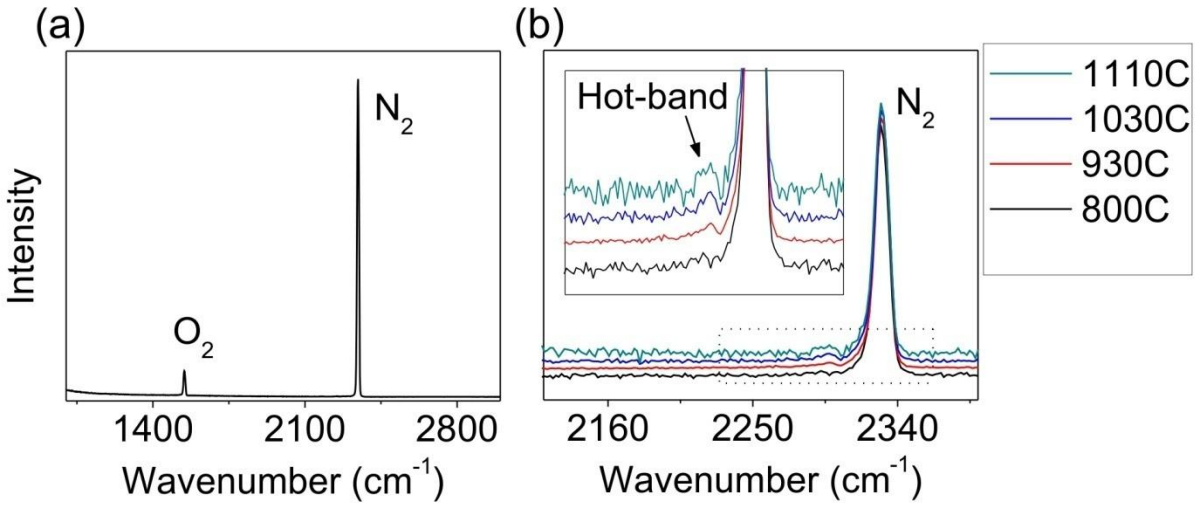

Figure A.1. (a) Room temperature single-beam CARS spectrum of air. (b) Spectrum near nitrogen as a function of temperature, showing the appearance of the hot-band.

Using the standoff detection setup and collecting signal in transmission, CARS spectra are easily acquired from air. An example spectrum is shown in Figure A.1a. The Raman shifts from molecular nitrogen and oxygen are visible. Carbon dioxide, present at about 400ppm, can also be observed with care (see Figure 3.6c). The discussion in this chapter will focus on using N_2 to measure the temperature as it is present in any air fed flame, and not consumed in combustion.

Figure A.1b displays the nitrogen CARS signal at several air temperatures. The air temperature was controlled by a tube furnace. Notice the appearance of an adjacent peak as the temperature is increased. This peak is termed the "hot-band" for obvious reasons. The growth of this peak is due to increasing population of the excited vibrational state of N_2. The nuclear separation potential is not purely harmonic, so the vibrational energy states are not evenly spaced, making transitions between the first and second excited vibrational states distinct from the ground state transitions. The energy shift in this case is ~30cm^{-1} to lower energy. The ratio of the two peaks is independent of density and laser power and provides a convenient method to measure temperature using Boltzman statistics. The fraction of the population in the excited state is approximated at low temperatures as

$$f \approx exp(\frac{-E_{\Omega}}{k_b T}).$$

The ratio of the hot-band intensity to the primary CARS signal is the square of this fraction, since CARS scales quadratically with molecule number.

A.3 Frequency Spread Dephasing Thermometry

Unfortunately, the required signal to noise for temperature determination through hot-band analysis is only available above ~800K. Many situations require measurements at lower

temperatures. This section describes a method which uses the dephasing of the CARS signal to determine temperature. This work appears in an article by Orin Yue *et al.*[79]

4.3.1 CARS Time Profile

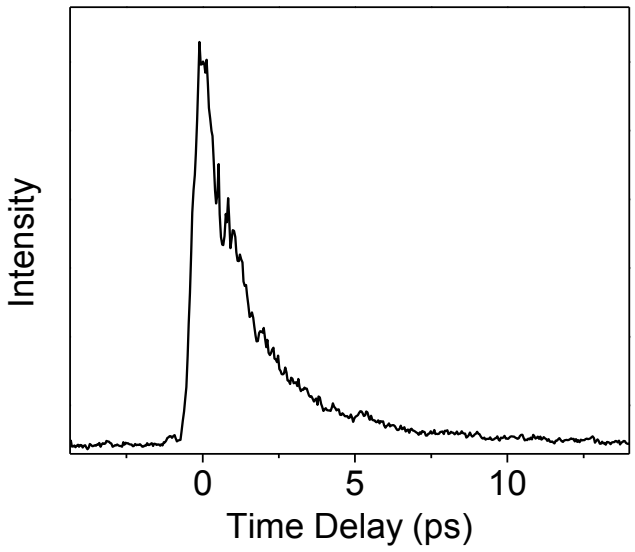

Figure A.2. The intensity of the N_2 CARS signal as a function of probe delay time.

The CARS intensity at the N_2 resonance is plotted as a function of probe time delay in Figure A.2. This is easily accomplished using the delay stage in the probe arm of the pulse shaper. The signal decays primarily due to frequency spread dephasing. Many closely spaced rovibrational transitions are impulsively excited by the broadband portion of the pulse, and the frequency differences cause the coherent excitation to gradually dephase. The frequency spread increases with temperature, as more rovibrational levels are populated, and the dephasing rate can be used for thermometry.[80]

Scanning the probe delay to measure decay rate is a time consuming process and suffers from shot-to-shot fluctuations. Our goal is to make a single-beam/single-shot thermometry method. One approach used previously, is to perform time to frequency mapping with a highly chirped probe.[81,82] The various frequencies within the probe arrive in the sample at different times, and the CARS signal resolved in the frequency domain will directly map to the time domain. These experiments required modeling and fitting of the signal to extract temperature. Here, a simplified empirical approach is used to quickly extract the temperature using three experimental values.

A.3.2 Experimental Setup

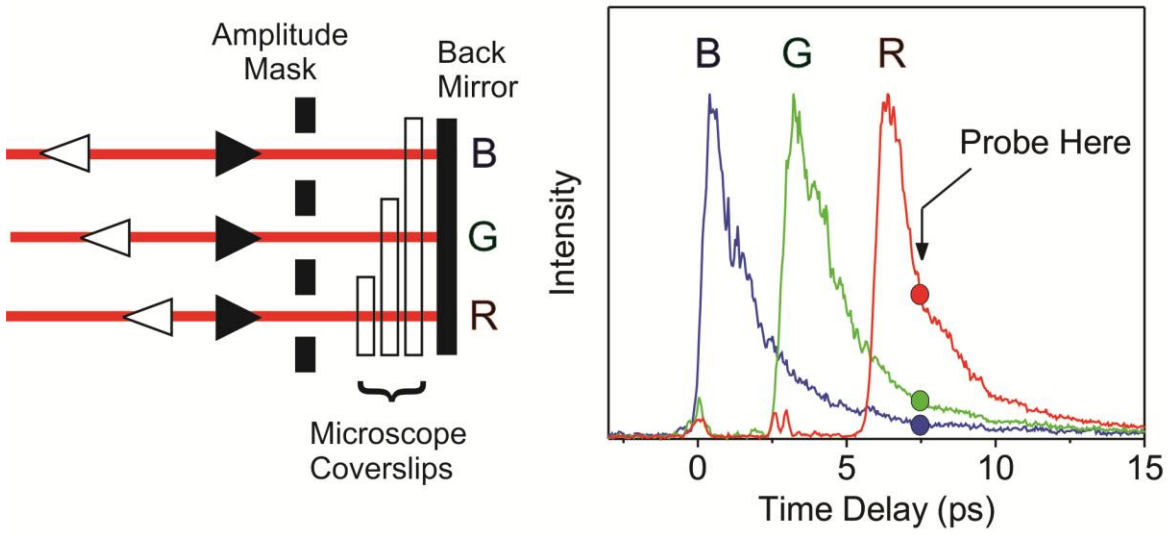

Figure A.3. (left) Schematic of the Fourier plane in the probe arm of the pulse shaper. (right) Resulting CARS signal as a function of probe delay.

The only change to the experimental setup is in the probe arm of the pulse shaper. Three probes are created by placing a mask at the Fourier plane (see Figure A.3). By inserting various

amounts of glass in each probe, the relative arrival time can be controlled. The three resulting CARS signals are plotted as a function of time. Fixing the delay, the CARS signal will sample three different probe delays, and the decay rate can be inferred.

As an aside, Figure A.3 also shows some properties of the non-resonant background. The small bumps in the R curve, which correspond to the onset of the CARS signal due to the other probes, are due to the non-resonant background. Non-resonant background is observed at all anti-Stokes shifts, but is only present when the probe overlaps the excitation pulse in time. As in the standoff detection experiments, the non-resonant spike should be avoided with appropriate time delays. In the gas phase, dephasing times are much longer and the non-resonant background is easier to avoid.

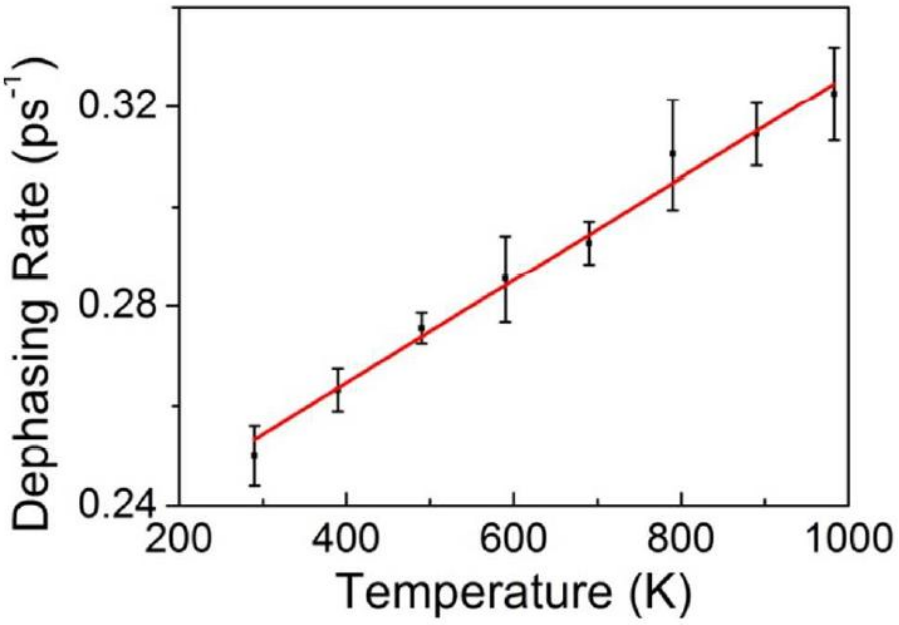

Figure A.4. The calibration curve consists of a line fit to the dephasing rate measured at various temperatures.

Calibration data is created by measuring the temperature inside a specially made oven. At every set temperature, a CARS spectrum is collected. An exponential decay is fit to the three data points measured from the intensity of each N_2 CARS band. A calibration data set of decay rate versus temperature is created and shown in Figure A.4. The data is fit with a line, which is the calibration curve.

A.3.3 Evaluation

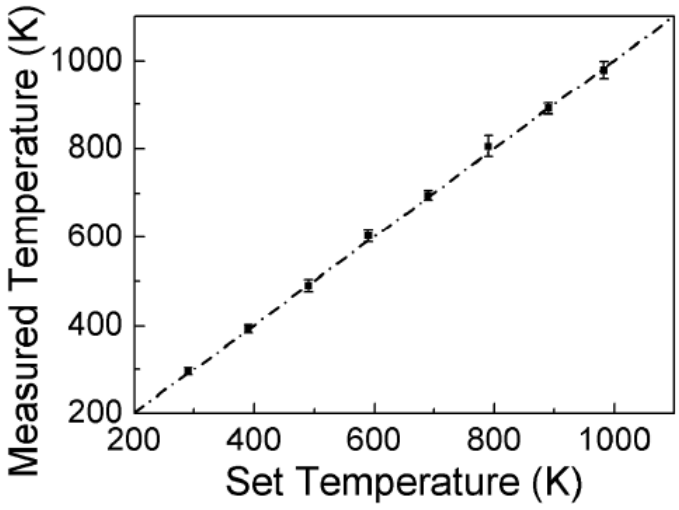

Figure A.5. The CARS thermometer is evaluated.

The method was tested using the same oven by comparing the set and measured temperatures. The results are shown in Figure A.5. The spectra from 200 laser pulses were averaged for each data point and the standard deviation of the mean used as the uncertainty. The technique is accurate to within 15 K in the range tested. At higher temperatures, the signal decays too fast and the hot-band technique must be used.

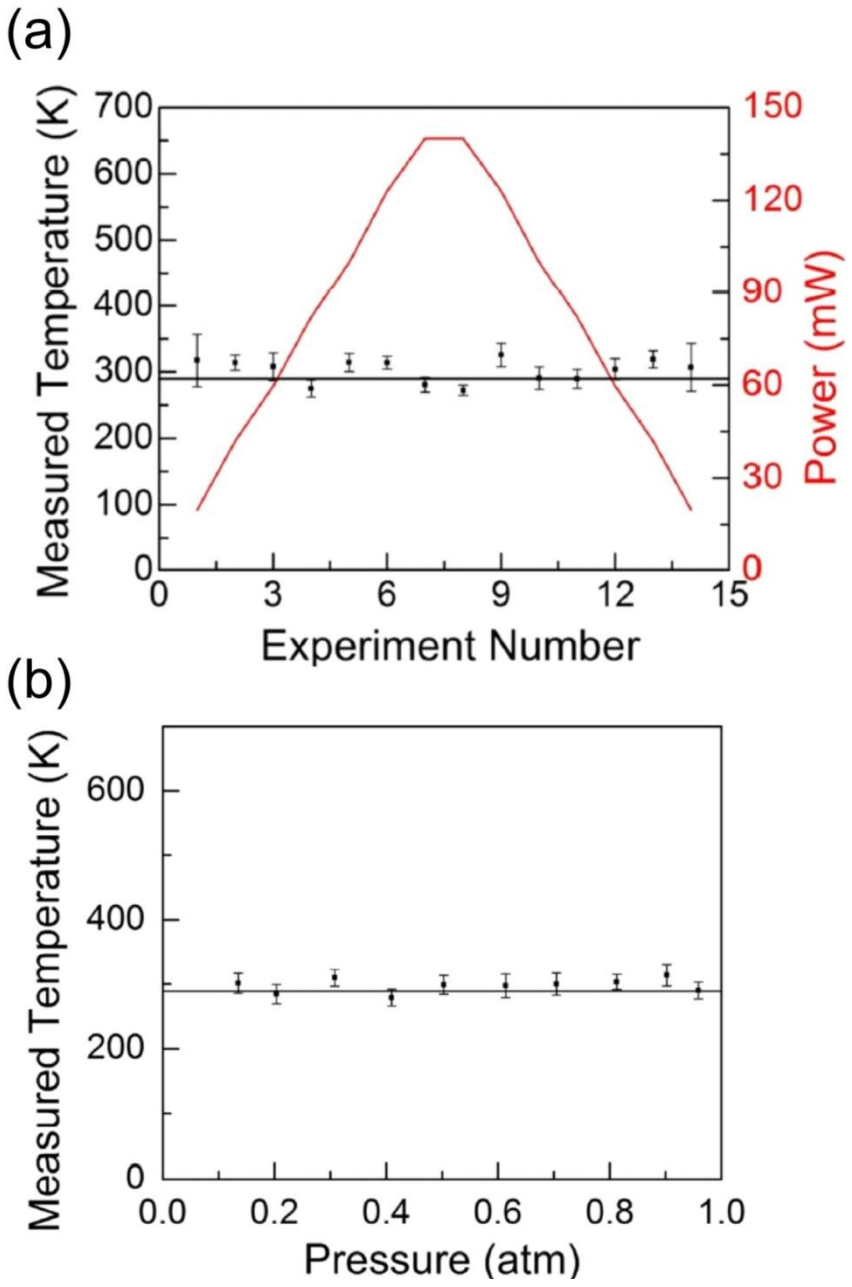

Figure A.6. (a) Measured temperature at several laser powers. (b) Measured temperature as a function of pressure.

Figure A.6 shows that the technique does not depend on pressure or laser power. The above data were based on 200 total laser shots to improve accuracy and calculate statistics. Figure A.7

shows the temperatures obtained on a single shot basis. This is a robust method to quickly measure temperatures in a combustion environment.

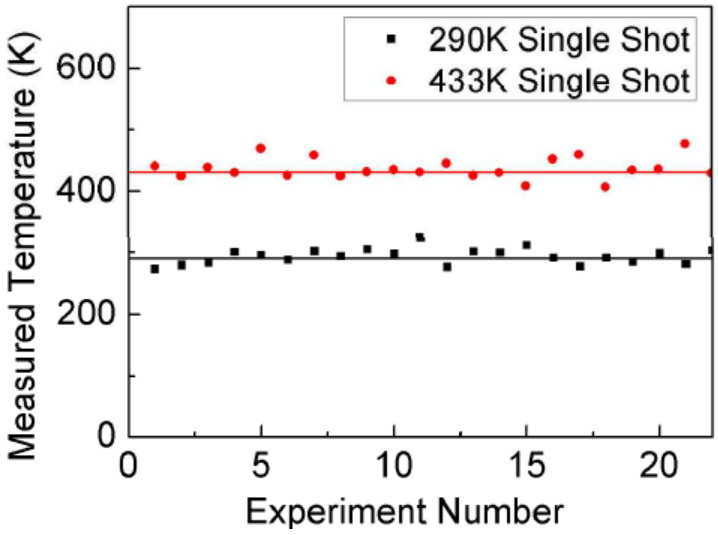

Figure A.7. Single-shot temperature measurements. The oven was set at the temperature denoted by the horizontal lines.

A.4 Combined Method for Flame Imaging

The two methods can be combined to make a wide range CARS thermometer that, in principle, can operate on a single shot basis. The technique also provides chemical information. Since the signal from the third order process comes primarily from the focus, three dimensional thermal maps can be created. In this section we present chemical and temperature cross sections of a Bunsen burner flame. The results are a part of a manuscript yet to be submitted.[83]

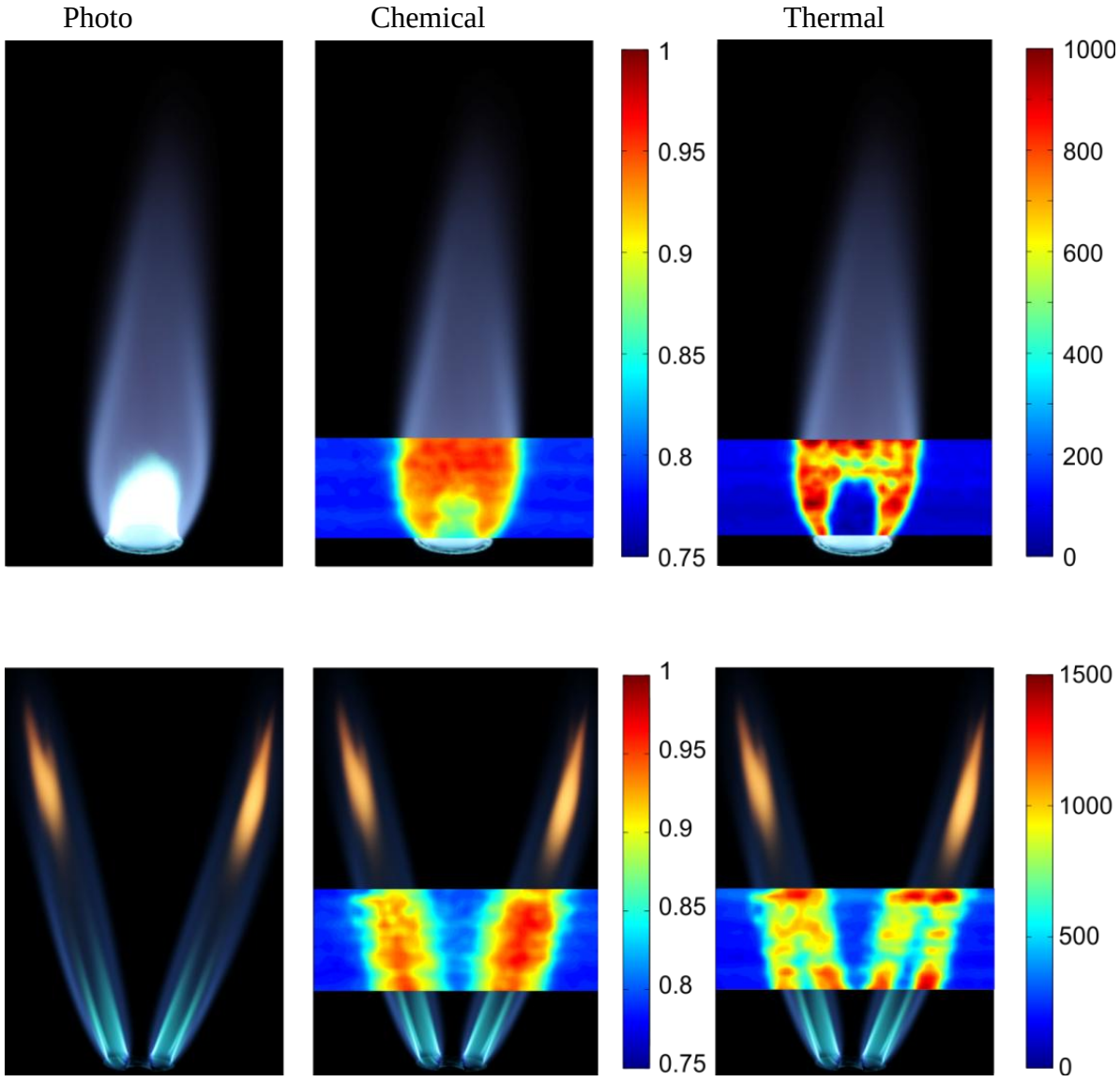

Figure A.8. The chemical and thermal images acquired using CARS are overlaid on the photographs of the flame. The chemical images show the concentration of nitrogen normalized to the total nitrogen and oxygen. The temperature, displayed in degrees Celsius, is measured over the entire range by using the two methods simultaneously to produce the thermal image.

Figure A.8 shows chemical and thermal maps from two propane/air flames. Note that the flame is air fed and the concentration of oxygen is reduced as it is consumed. The temperature is measured form the unconsumed N_2 CARS signal, although oxygen can also be used. The spectra from multiple laser shots were averaged to create the above images, but with

experimental advances, the technique could provide a fast, single-beam, temperature and chemical sensor for combustion diagnostics.

Appendix B - Femtosecond Lasers in the Time and Frequency Domain

The electric field is a real quantity and a femtosecond pulse can be created mathematically by multiplying a cosine function by a normalized Gaussian.

$$E_0(t) = E_0 G(t) cos(\omega_c t) .$$

Through Fourier analysis, the corresponding field in the frequency domain can be calculated,

$$\tilde{E}_0(\omega) = FT[E_0 G(t) cos(\omega_c t)] \propto \tilde{E}_0 \tilde{G}(\omega) * (\delta(\omega - \omega_c) + \delta(\omega + \omega_c))$$

The spectrum consists of two Gaussian profiles in the frequency domain, centered at positive and negative carrier frequency, ω_c. This obeys the relation $\tilde{E}(\omega) = \tilde{E}(\omega)^*$, which is true for any real *E(t)*. The negative frequencies in $\tilde{E}(\omega)$ are often dropped, but this will make *E(t)* complex. It should be understood that the real part of *E(t)* represents the actual field. However, detectors generally measure intensity,

$$I(t) \propto | E(t) |^2,$$

and the complex form of *E* is suitable. Similarly, spectral intensity is proportional to the modulus square of the frequency component of the electric field

$$I(\omega) \propto |\tilde{E}(\omega)|^2 .$$

The spectral phase is contained within the complex valued $\tilde{E}(\omega)$.

Note that a narrow Gaussian in time will become a broad Gaussian in the frequency domain due to the scaling property of Fourier transforms. The Fourier transform of $G(at)$ is proportional to $\tilde{G}(\omega/a)$, demonstrating the broad bandwidth requirement of short pulses.

Appendix C - Pulse Shaping

With broadband pulses, the temporal profile can be controlled in the frequency domain through Fourier synthesis. Ignoring the vectoral nature of the field, changing the amplitude and phase of each frequency provides total control of the pulse in the time domain.

C.1 Amplitude Shaping

Pulsed lasers typically emit trains of pulses. Oscillators will emit pulses with a period equal to the cavity round trip time. Mathematically, this is equivalent to the convolution of the Gaussian pulse with a "comb" function, III(t), where

$$III_T(t) = \sum_n \delta(t - Tn).$$

Using the convolution rule for Fourier transforms, the resulting frequency domain spectrum will consist of a comb function multiplied by a Gaussian. With high resolution spectrometers and stable oscillators, these narrow spectral lines can be observed. These frequency combs can be used for high resolution spectroscopy and atomic clocks. The features are so fine that the spectrum can be assumed smooth for most applications.

This shows one way in which amplitude shaping can dramatically change the pulse shape. Pulse trains can be created by passing the laser through a periodic spectral filter, an etalon for example.

An etalon is just a small cavity, corresponding to a relatively coarse comb. This corresponds to a fine comb in the time domain, and a series of closely spaced pulses. Similarly, a square spectrum will create a sinc-like intensity profile in the time domain. The drawback of amplitude shaping is that the laser power is reduced, significantly reducing the efficiency of non-linear processes. This is why phase shaping is preferred throughout this dissertation. Phase shaping is very powerful in controlling the time profile of the laser pulse.

C.2 Spectral Phase

Applying a linear phase function, $\phi(\omega) = -\tau\omega$, will delay the pulse in time.

$$\tilde{E}_1(\omega) = \tilde{E}_0(\omega)e^{i\phi(\omega)} = \tilde{E}_0(\omega)e^{-i\tau\omega}$$

$$E_1(t) = IFT[\tilde{E}_0(\omega)e^{-i\tau\omega}] = E_0(t-\tau).$$

A linear spectral phase is equivalent to changing the optical path length and will not affect non-linear processes. Quadratic or higher order spectral phases can be introduced by optical components, and will change the temporal profile and the outcome of non-linear processes. Analytical expressions for the time domain effect of these higher order phases are harder to derive. However, the effect is easily visualized by taking the derivative of the spectral phase and

equating the value to the time delay. For example, a quadratic phase will introduce a linear change in frequency versus time as visualized in the spectrogram in Figure A1.

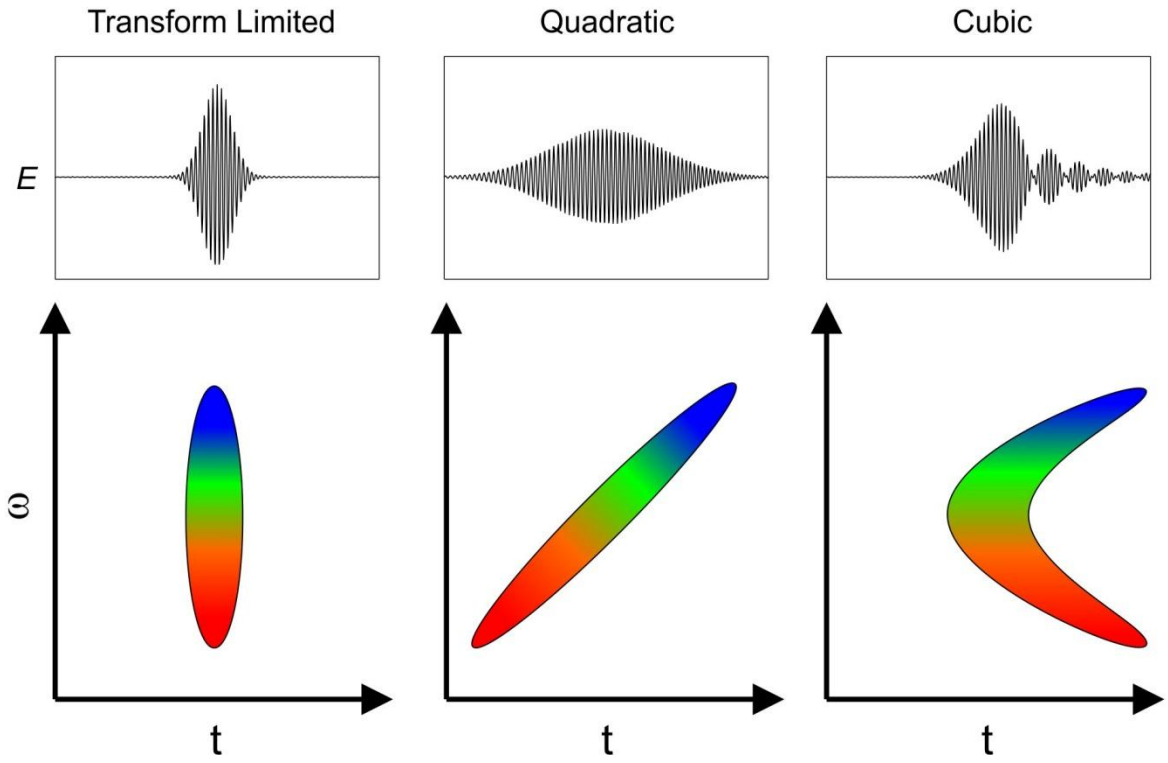

Figure C.1. Effect of basic spectral phases on the shape of the pulse. Note the spectrograms are schematic representations to aid understanding. Beating between the red and blue parts of the spectrum is observed in the cubic phase.

C.3 Dispersion

All materials produce dispersion in the phase velocity for different frequencies. This includes the glass (lenses, windows) in the optical setup and the air in which the beam travels. This can have a significant effect on broadband pulses. All spectral phases of 2nd order or higher will increase the pulse duration from the transform limited (constant spectral phase) case.

The spectral phase due to dispersion is often expanded in a Taylor series around the carrier frequency:

$$\phi(\omega) = \phi_{\omega c}^{(0)} + \phi_{\omega c}^{(1)}(\omega - \omega_c) + \phi_{\omega c}^{(2)} \frac{(\omega - \omega_c)^2}{2} + \phi_{\omega c}^{(3)} \frac{(\omega - \omega_c)^3}{6} .$$

In general, the influence of each term decreases rapidly with order. Prism pair or grating based compressors can compensate for quadratic dispersion, which is adequate for low dispersion or narrow bandwidth lasers. Pulse shapers can compensate for all orders of dispersion and are extremely useful in compressing broad bandwidth lasers to their transform limited pulse durations.

Appendix D - Experimental Details

D.1 Details of the Laser System

A titanium sapphire oscillator (Coherent, Micra) produces 20fs, 3nJ pulses FWHM centered at 800nm with a repetition rate of 80MHz. This output is sent through a pulse shaper (BiophotonicSolutions, Femtofit) and delivered to the chirped pulse regenerative amplifier (Coherent, Legend). The primary purpose of the pulse shaper is to compensate for high order dispersion in the output of the amplifier. The amplifier selects one of every 80,000 pulses for amplification, reducing the repetition rate to 1kHz. These pulses are heavily chirped (lengthened in time) to reduce the peak intensity and prevent destruction of the gain medium and other non-linear effects. Amplification is performed in a cavity with a titanium sapphire gain medium. When the pulses reach adequate intensity, they are released from the cavity, de-chirped with a grating compressor and exit the amplifier system. This output can support a ~35 fs pulse (1mJ), which is larger than the input due to gain narrowing in the amplifier.

D.2 SRS Data Collection Details

Each amplified laser pulse will produce four total signals, two "red" and two "blue", recorded by the oscilloscope at 20 GSa/s. The oscilloscope can store the corresponding signal locally for at least 1600 laser pulses. The home-built software analyses each set separately. Considering only one channel, (e.g. blue), the software sums the highest 20 points (typically) from each of the two

pulses and computes the normalized difference. By choosing this set of highest values, rather than integrating over a set time window, noise contributions from the time jitter between the trigger and signal are avoided. The noise level versus included points is shown in Figure D.1.

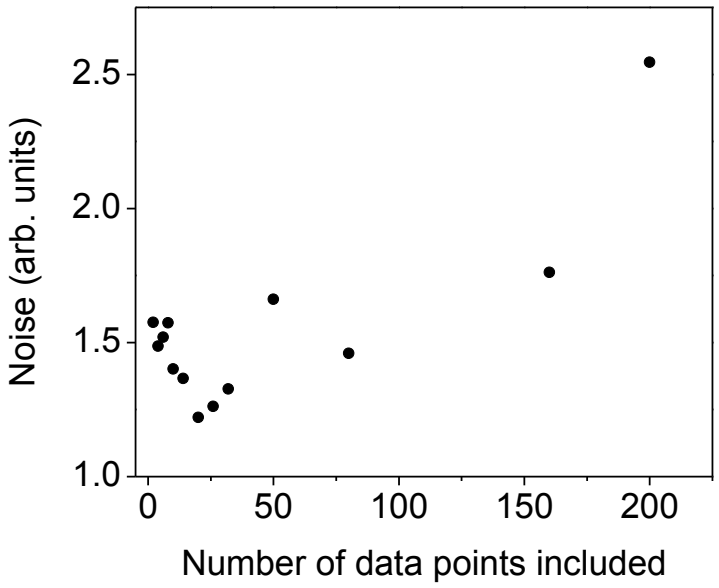

Figure D.1. Noise as a function of the number of included data points in the peak. The noise level is reduced by including more points until around 20 points are included. Including more points increases the noise level as the additional points are closer to the base of the peak.

During spectral acquisition, the signal from several amplified laser pulses is computed and summed to form a single spectral value. The pulse shaper switches to a new spectral phase, and the process is repeated. A wait time of up to 200 ms is required for the liquid crystals in the SLM to reach their equilibrium value, but shorter times still produce reasonable spectra. The spectral phase for each resonance is easily calculated as

$$\phi_{\Omega,R,\omega_0}(\omega) = \begin{cases} R(\omega - (\omega_0 - \Omega/2))^2, & \omega < \omega_0 \\ R(\omega - (\omega_0 + \Omega/2))^2, & \omega > \omega_0 \end{cases},$$

where Ω is the target resonance, $\omega_0$is ideally the center of the spectrum, and *R* is inversely proportional to the resolution of the excitation. The typical *R* value in these experiments was 4000 fs^2 at 1000 cm^{-1}. The *R* value must be altered during the scan to maintain resolution and prevent overlap in the excitation range of the primary and replicated pulses.

$$R = 4000\text{fs}^2 \frac{1000\text{cm}^{-1}}{\Omega}.$$

Images were acquired by scanning the target area using fast-tilting mirrors. This motion was synchronized to the laser repetition rate to ensure single-shot-per-pixel imaging. The corresponding digitized photodiode signals for an entire frame are stored locally on the oscilloscope before processing. As an example, a 30x30 image will require storage of the data from the corresponding 900 laser pulses. After a single frame is acquired, the data is loaded to the computer for processing, and the chemical image is constructed. This process repeats until the desired frame number is achieved. The lag time between frames is typically 1-2 seconds, but depends on image size. Little effort was expended in reducing the between-frame dead time. Generally, the spectral phase was changed every other frame, switching between producing a primary pulse on resonance and a replicated pulse on resonance. This produces alternating positive and negative signals and will cancel out any systematic errors.

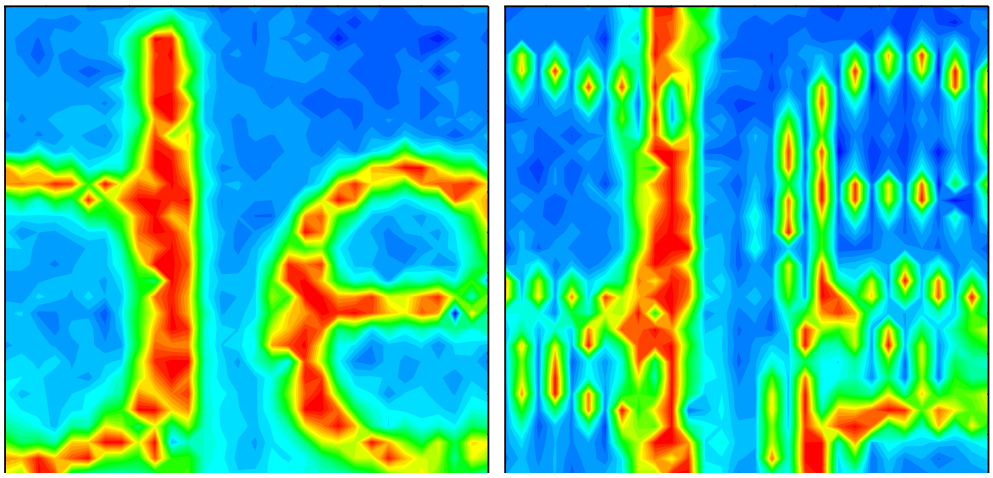

Figure D.2. Illustration of the digitizer synchronization problem with two collections of images. Synchronized images (left) and unsynchronized images (right). The replica pulse was blocked and the lettering of a business card was imaged. The result is a collection of synchronized and unsynchronized images. These can be sorted, as done here, if the image pattern is known and there is high signal to noise, but in general will limit contrast.

Although all components were triggered from the same source, it was found that the oscilloscope was not always well synchronized. Every few image frames, the oscilloscope would miss the first few pulses in the raster scanning series, distorting the image. This is demonstrated in the bright field images of Figure D.2. This problem was solved by including a marker pixel; the laser was deliberately shot off-target for one laser shot, producing a distinguishable value. All frames in which the pixel value was incorrect were thrown out.

D.3. SRS Noise Suppression

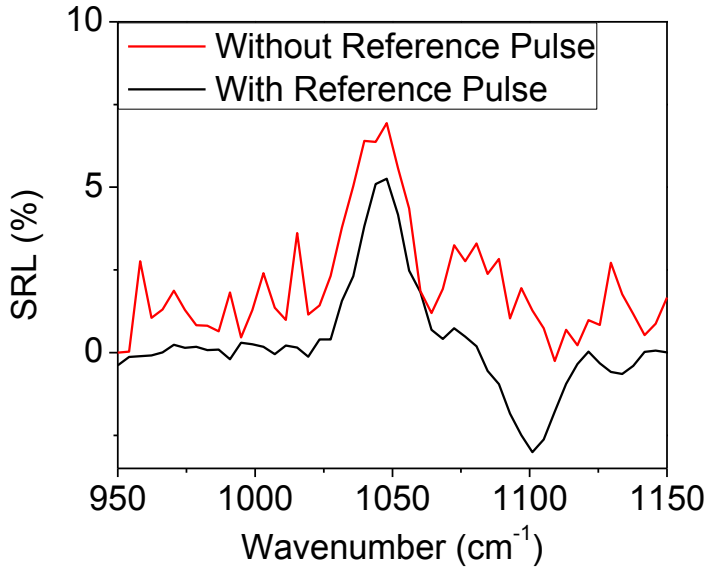

Figure D.3. SRL spectra of bulk NH_4NO_3, acquired with 20 pulses per point. For the red curve (top), the initial intensity is used as a reference to measure SRL. The use of the time multiplexed replica pulse dramatically reduces the noise level (black/bottom curve).

Measuring SRS requires a reference, since the signal is found in small changes in the laser intensity. Generally, SRS microscopy utilizes lock-in detection and modulation at high frequency, up to half the laser repetition rate.[68] This is effective since laser noise is generally low at small time scales. With amplified, low repetition rate lasers the shot-to-shot fluctuations are much more significant, generally on the order of 1% or more, which can overwhelm the SRS signal. To compensate for this without extensive averaging, we create a time-delayed replica of every pulse. A small change in the temporal shape, caused by dispersion, of the replicated pulse shifts the excitation frequency and allows us to detect SRS by comparing the intensity of the otherwise identical pulses. A related self referencing technique was implemented recently for two color SRS microscopy with lock-in detection.[84] There, a delay line effectively doubled the

repetition rate of one of the lasers, dramatically reducing the noise at the detection frequency and allowing SRS microscopy with a noisy fiber laser system. Figure D.3 demonstrates the effectiveness of the referencing technique.

REFERENCES

REFERENCES

1. Ramos, C. & Dagdigian, P. J. Detection of vapors of explosives and explosive-related compounds by ultraviolet cavity ringdown spectroscopy. *Appl. Opt.* **46,** 620–627 (2007).

2. Sylvia, J. M., Janni, J. A., Klein, J. D. & Spencer, K. M. Surface-Enhanced Raman Detection of 2,4-Dinitrotoluene Impurity Vapor as a Marker To Locate Landmines. *Anal. Chem.* **72,** 5834–5840 (2000).

3. Qi, P. *et al.* Toward Large Arrays of Multiplex Functionalized Carbon Nanotube Sensors for Highly Sensitive and Selective Molecular Detection. *Nano Lett.* **3,** 347–351 (2003).

4. Moore, D. S. Instrumentation for trace detection of high explosives. *Rev. Sci. Instrum.* **75,** 2499 (2004).

5. Moore, D. S. Recent Advances in Trace Explosives Detection Instrumentation. *Sens. Imaging Int. J.* **8,** 9–38 (2007).

6. Willer, U. & Schade, W. Photonic sensor devices for explosive detection. *Anal. Bioanal. Chem.* **395,** 275–282 (2009).

7. Wallin, S., Pettersson, A., Östmark, H. & Hobro, A. Laser-based standoff detection of explosives: a critical review. *Anal. Bioanal. Chem.* **395,** 259–274 (2009).

8. Furstenberg, R. *et al.* Stand-off detection of trace explosives via resonant infrared photothermal imaging. *Appl. Phys. Lett.* **93,** 224103 (2008).

9. Blake, T. A., Kelly, J. F., Gallagher, N. B., Gassman, P. L. & Johnson, T. J. Passive standoff detection of RDX residues on metal surfaces via infrared hyperspectral imaging. *Anal. Bioanal. Chem.* **395,** 337–348 (2009).

10. Pacheco-Londoño, L. C., Ortiz-Rivera, W., Primera-Pedrozo, O. M. & Hernández-Rivera, S. P. Vibrational spectroscopy standoff detection of explosives. *Anal. Bioanal. Chem.* **395,** 323–335 (2009).

11. Van Neste, C. W., Senesac, L. R. & Thundat, T. Standoff photoacoustic spectroscopy. *Appl. Phys. Lett.* **92,** 234102 (2008).

12. Ray, M. D., Sedlacek, A. J. & Wu, M. Ultraviolet mini-Raman lidar for stand-off, in situ identification of chemical surface contaminants. *Rev. Sci. Instrum.* **71,** 3485 (2000).

13. Sharma, S. K., Lucey, P. G., Ghosh, M., Hubble, H. W. & Horton, K. A. Stand-off Raman spectroscopic detection of minerals on planetary surfaces. *Spectrochim. Acta. A. Mol. Biomol. Spectrosc.* **59,** 2391–2407 (2003).

14. Carter, J. C. *et al.* Standoff Detection of High Explosive Materials at 50 Meters in Ambient Light Conditions Using a Small Raman Instrument. *Appl. Spectrosc.* **59,** 769–775 (2005).
15. Hobro, A. J. & Lendl, B. Stand-off Raman spectroscopy. *TrAC Trends Anal. Chem.* **28,** 1235–1242 (2009).

16. Pettersson, A. *et al.* Explosives standoff detection using Raman spectroscopy: from bulk towards trace detection. *Proc. SPIE* 76641K–76641K (2010). doi:10.1117/12.852544

17. Dudik, J. M., Johnson, C. R. & Asher, S. A. Wavelength dependence of the preresonance Raman cross sections of CH3CN, SO42−, ClO4−, and NO3−. *J. Chem. Phys.* **82,** 1732–1740 (1985).

18. Gaft, M. & Nagi, L. UV gated Raman spectroscopy for standoff detection of explosives. *Opt. Mater.* **30,** 1739–1746 (2008).

19. Jander, P. & Noll, R. Automated Detection of Fingerprint Traces of High Explosives Using Ultraviolet Raman Spectroscopy. *Appl. Spectrosc.* **63,** 559–563 (2009).

20. Chirico, R. *et al.* Stand-off detection of traces of explosives and precursors on fabrics by UV Raman spectroscopy. 85460W–85460W (2012). doi:10.1117/12.974518

21. Reichardt, T. A., Bisson, S. E. & Kulp, T. J. Standoff Ultraviolet Raman Scattering Detection of Trace Levels of Explosives. *Sandia Rep.* **SAND2011-7955,** (2011).

22. Nagli, L., Gaft, M., Fleger, Y. & Rosenbluh, M. Absolute Raman cross-sections of some explosives: Trend to UV. *Opt. Mater.* **30,** 1747–1754 (2008).

23. Maker, P. D. & Terhune, R. W. Study of Optical Effects Due to an Induced Polarization Third Order in the Electric Field Strength. *Phys. Rev.* **137,** A801 (1965).

24. Tolles, W. M., Nibler, J. W., McDonald, J. R. & Harvey, A. B. A Review of the Theory and Application of Coherent Anti-Stokes Raman Spectroscopy (CARS). *Appl. Spectrosc.* **31,** 253–271 (1977).

25. Evans, C. L. & Xie, X. S. Coherent Anti-Stokes Raman Scattering Microscopy: Chemical Imaging for Biology and Medicine. *Annu. Rev. Anal. Chem.* **1,** 883–909 (2008).

26. Evans, C. L. *et al.* Chemical Imaging of Tissue in Vivo with Video-Rate Coherent Anti-Stokes Raman Scattering Microscopy. *Proc. Natl. Acad. Sci. U. S. A.* **102,** 16807–16812 (2005).

27. Boyd, R. W. *Nonlinear Optics*. (Acad. Press, 2003).

28. Shen, Y. R. The principles of nonlinear optics. *N. Y. Wiley-Intersci. 1984 575 P* **-1,** (1984).

29. Song, J. J., Eesley, G. L. & Levenson, M. D. Background suppression in coherent Raman spectroscopy. *Appl. Phys. Lett.* **29,** 567 (1976).

30. Jurna, M., Korterik, J. P., Otto, C., Herek, J. L. & Offerhaus, H. L. Vibrational Phase Contrast Microscopy by Use of Coherent Anti-Stokes Raman Scattering. *Phys. Rev. Lett.* **103,** 043905 (2009).

31. Liu, Y., Lee, Y. J. & Cicerone, M. T. Fast extraction of resonant vibrational response from CARS spectra with arbitrary nonresonant background. *J. Raman Spectrosc.* **40,** 726–731 (2009).
32. Dudovich, N., Oron, D. & Silberberg, Y. Single-pulse coherently controlled nonlinear Raman spectroscopy and microscopy. *Nature* **418,** 512–514 (2002).

33. Oron, D., Dudovich, N. & Silberberg, Y. Single-pulse phase-contrast nonlinear Raman spectroscopy. *Phys. Rev. Lett.* **89,** (2002).

34. Oron, D., Dudovich, N. & Silberberg, Y. Femtosecond Phase-and-Polarization Control for Background-Free Coherent Anti-Stokes Raman Spectroscopy. *Phys. Rev. Lett.* **90,** 213902 (2003).

35. Von Vacano, B., Buckup, T. & Motzkus, M. Highly sensitive single-beam heterodyne coherent anti-Stokes Raman scattering. *Opt. Lett.* **31,** 2495–2497 (2006).

36. Von Vacano, B. & Motzkus, M. Time-resolved two color single-beam CARS employing supercontinuum and femtosecond pulse shaping. *Opt. Commun.* **264,** 488–493 (2006).

37. Bremer, M. T., Wrzesinski, P. J., Butcher, N., Lozovoy, V. V. & Dantus, M. Highly selective standoff detection and imaging of trace chemicals in a complex background using single-beam coherent anti-Stokes Raman scattering. *Appl. Phys. Lett.* **99,** 101109–101109–3 (2011).

38. Bremer, M. T., Lozovoy, V. V. & Dantus, M. Nondestructive detection and imaging of trace chemicals with high-chemical specificity using single-beam coherent anti-stokes Raman scattering in a standoff configuration. 835818–835818 (2012). doi:10.1117/12.919404

39. Ooi, C. H. R. *et al.* Theory of femtosecond coherent anti-Stokes Raman backscattering enhanced by quantum coherence for standoff detection of bacterial spores. *Phys. Rev. A* **72,** 023807 (2005).

40. Petrov, G. I. *et al.* Comparison of coherent and spontaneous Raman microspectroscopies for noninvasive detection of single bacterial endospores. *Proc. Natl. Acad. Sci.* **104,** 7776–7779 (2007).

41. Dogariu, A., Michael, J. B., Scully, M. O. & Miles, R. B. High-Gain Backward Lasing in Air. *Science* **331,** 442–445 (2011).

42. Li, H. *et al.* Coherent mode-selective Raman excitation towards standoff detection. *Opt. EXPRESS* **16,** 5499–5504 (2008).

43. Li, H. *et al.* Standoff and arms-length detection of chemicals with single-beam coherent anti-Stokes Raman scattering. *Appl. Opt.* **48,** B17–B22 (2009).

44. Katz, O., Natan, A., Silberberg, Y. & Rosenwaks, S. Standoff detection of trace amounts of solids by nonlinear Raman spectroscopy using shaped femtosecond pulses. *Appl. Phys. Lett.* **92,** 171116 (2008).

45. Natan, A., Levitt, J. M., Graham, L., Katz, O. & Silberberg, Y. Standoff detection via single-beam spectral notch filtered pulses. *Appl. Phys. Lett.* **100,** 051111–051111–3 (2012).

46. Portnov, A., Bar, I. & Rosenwaks, S. Highly sensitive standoff detection of explosives via backward coherent anti-Stokes Raman scattering. *Appl. Phys. B-LASERS Opt.* **98,** 529–535 (2010).

47. Nisoli, M., De Silvestri, S. & Svelto, O. Generation of high energy 10 fs pulses by a new pulse compression technique. *Appl. Phys. Lett.* **68,** 2793–2795 (1996).

48. Coello, Y. *et al.* Interference without an interferometer: a different approach to measuring, compressing, and shaping ultrashort laser pulses. *J. Opt. Soc. Am. B* **25,** A140–A150 (2008).

49. Plewicki, M., Weise, F., Weber, S. M. & Lindinger, A. Phase, amplitude, and polarization shaping with a pulse shaper in a Mach-Zehnder interferometer. *Appl. Opt.* **45,** 8354–8359 (2006).

50. Masihzadeh, O., Schlup, P. & Bartels, R. A. Complete polarization state control ofultrafast laser pulses with a single linearspatial light modulator. *Opt. Express* **15,** 18025–18032 (2007).

51. Meshulach, D. & Silberberg, Y. Coherent quantum control of multiphoton transitions by shaped ultrashort optical pulses. *Phys. Rev. A* **60,** 1287–1292 (1999).

52. Weiner, A. M., Leaird, D. E., Wiederrecht, G. P. & Nelson, K. A. Femtosecond Pulse Sequences Used for Optical Manipulation of Molecular Motion. *Science* **247,** 1317–1319 (1990).

53. Weiner, A. M. & Leaird, D. E. Generation of terahertz-rate trains of femtosecond pulses by phase-only filtering. *Opt. Lett.* **15,** 51–53 (1990).

54. Gershgoren, E. *et al.* Simplified setup for high-resolution spectroscopy that uses ultrashort pulses. *Opt. Lett.* **28,** 361–363 (2003).

55. Hellerer, T., Enejder, A. M. K. & Zumbusch, A. Spectral focusing: High spectral resolution spectroscopy with broad-bandwidth laser pulses. *Appl. Phys. Lett.* **85,** 25–27 (2004).

56. Pestov, D. *et al.* Pulse shaping for mode-selective ultrafast coherent Raman spectroscopy of highly scattering solids. *J. Opt. Soc. Am. B* **25,** 768–772 (2008).

57. Isobe, K. *et al.* Single-pulse coherent anti-Stokes Raman scattering microscopy employing an octave spanning pulse. *Opt. Express* **17,** 11259–11266 (2009).

58. Bremer, M. T. & Dantus, M. Standoff detection and imaging with selective stimulated Raman scattering. *Appl. Phys. Lett.*

59. Bloembergen, N. The Stimulated Raman Effect. *Am. J. Phys.* **35,** 989 (1967).

60. Woodbury, E. L. & Ng, W. K. Correspondence. *Proc. IRE* **50,** 2365–2383 (1962).

61. Kasevich, M. & Chu, S. Laser cooling below a photon recoil with three-level atoms. *Phys. Rev. Lett.* **69,** 1741–1744 (1992).

62. Fang, C., Frontiera, R. R., Tran, R. & Mathies, R. A. Mapping GFP structure evolution during proton transfer with femtosecond Raman spectroscopy. *Nature* **462,** 200–204 (2009).

63. Ploetz, E., Laimgruber, S., Berner, S., Zinth, W. & Gilch, P. Femtosecond stimulated Raman microscopy. *Appl. Phys. B* **87,** 389–393 (2007).
64. Freudiger, C. W. *et al.* Label-Free Biomedical Imaging with High Sensitivity by Stimulated Raman Scattering Microscopy. *Science* **322,** 1857–1861 (2008).

65. Saar, B. G. *et al.* Video-Rate Molecular Imaging in Vivo with Stimulated Raman Scattering. *Science* **330,** 1368–1370 (2010).

66. Ozeki, Y., Dake, F., Kajiyama, S., Fukui, K. & Itoh, K. Analysis and experimental assessment of the sensitivity of stimulated Raman scattering microscopy. *Opt. Express* **17,** 3651–3658 (2009).

67. Levine, B., Shank, C. V. & Heritage, J. P. Surface vibrational spectroscopy using stimulated Raman scattering. *IEEE J. Quantum Electron.* **15,** 1418–1432 (1979).

68. Ozeki, Y. *et al.* Stimulated Raman scattering microscope with shot noise limited sensitivity using subharmonically synchronized laser pulses. *Opt. Express* **18,** 13708–13719 (2010).

69. Ozeki, Y. High-sensitivity stimulated Raman scattering microscopy. at <https://sites.google.com/site/ysozeki/research-1>

70. Kukura, P., McCamant, D. W., Yoon, S., Wandschneider, D. B. & Mathies, R. A. Structural Observation of the Primary Isomerization in Vision with Femtosecond-Stimulated Raman. *Science* **310,** 1006–1009 (2005).

71. Tripathi, A. *et al.* Semi-Automated Detection of Trace Explosives in Fingerprints on Strongly Interfering Surfaces with Raman Chemical Imaging. *Appl. Spectrosc.* **65,** 611–619 (2011).

72. Rahav, S. & Mukamel, S. Stimulated coherent anti-Stokes Raman spectroscopy (CARS) resonances originate from double-slit interference of two-photon Stokes pathways. *Proc. Natl. Acad. Sci.* **107,** 4825–4829 (2010).

73. Lang, T., Kompa, K.-L. & Motzkus, M. Femtosecond CARS on H2. *Chem. Phys. Lett.* **310,** 65–72 (1999).

74. Beaud, P., Frey, H.-M., Lang, T. & Motzkus, M. Flame thermometry by femtosecond CARS. *Chem. Phys. Lett.* **344,** 407–412 (2001).

75. Prince, B. D., Chakraborty, A., Prince, B. M. & Stauffer, H. U. Development of simultaneous frequency- and time-resolved coherent anti-Stokes Raman scattering for ultrafast detection of molecular Raman spectra. *J. Chem. Phys.* **125,** 044502 (2006).

76. Miller, J. D., Roy, S., Slipchenko, M. N., Gord, J. R. & Meyer, T. R. Single-shot gas-phase thermometry using pure-rotational hybrid femtosecond/picosecond coherent anti-Stokes Raman scattering. *Opt. Express* **19,** 15627–15640 (2011).

77. Miller, J. D., Slipchenko, M. N. & Meyer, T. R. Probe-pulse optimization for nonresonant suppression in hybrid fs/ps coherent anti-Stokes Raman scattering at high temperature. *Opt. Express* **19,** 13326–13333 (2011).

78. Roy, S. *et al.* Single-beam coherent anti-Stokes Raman scattering spectroscopy of N[sub 2] using a shaped 7 fs laser pulse. *Appl. Phys. Lett.* **95,** 074102 (2009).

79. Yue, O. *et al.* Single-Shot Gas-Phase Thermometry by Time-to-Frequency Mapping of Coherence Dephasing. *J. Phys. Chem. A* **116,** 8138–8141 (2012).

80. Lucht, R. P., Roy, S., Meyer, T. R. & Gord, J. R. Femtosecond coherent anti-Stokes Raman scattering measurement of gas temperatures from frequency-spread dephasing of the Raman coherence. *Appl. Phys. Lett.* **89,** 251112 (2006).

81. Lang, T. & Motzkus, M. Single-shot femtosecond coherent anti-Stokes Raman-scattering thermometry. *J. Opt. Soc. Am. B* **19,** 340 (2002).

82. Roy, S., Kulatilaka, W. D., Richardson, D. R., Lucht, R. P. & Gord, J. R. Gas-phase single-shot thermometry at 1 kHz using fs-CARS spectroscopy. *Opt. Lett.* **34,** 3857–3859 (2009).

83. Yue, O. *et al.* Imaging the temperature and chemical makeup of flames in 3D with single beam CARS. *Prep.*

84. Nose, K. *et al.* Sensitivity enhancement of fiber-laser-based stimulated Raman scattering microscopy by collinear balanced detection technique. *Opt. Express* **20,** 13958–13965 (2012).